

POWER GENERATION FROM LOW TEMPERATURE LIQUID DOMINATED
GEOTHERMAL SYSTEMS UTILIZING A BINARY POWER PLANT

A THESIS SUBMITTED TO
THE BOARD OF GRADUATE PROGRAMS
OF
MIDDLE EAST TECHNICAL UNIVERSITY, NORTHERN CYPRUS CAMPUS

BY

OUBAIDA TAJI

IN PARTIAL FULFILLMENT OF THE REQUIREMENTS
FOR
THE DEGREE OF MASTER OF SCIENCE
IN SUSTAINABLE ENVIRONMENT AND ENERGY SYSTEMS PROGRAM

AUGUST 2022

Approval of the Board of Graduate Programs

Prof. Dr. Cumali Sabah
Chairperson

I certify that this thesis satisfies all the requirements as a thesis for the degree of Master of Science

Asst. Prof. Dr. Ceren İnce Derogar
Program Coordinator

This is to certify that we have read this thesis and that in our opinion it is fully adequate, in scope and quality, as a thesis for the degree of Master of Science.

Prof. Dr. Mahmut Parlaktuna
Co-Supervisor

Asst. Prof. Dr. Doruk Alp
Supervisor

Examining Committee Members

Prof. Dr. Salih Saner NEU/ PNGE _____

Asst. Prof. Dr. Doruk Alp METU-NCC/ PNGE _____

Asst. Prof. Dr. Gamze İpek METU-NCC/ PNGE _____

I hereby declare that all information in this document has been obtained and presented in accordance with academic rules and ethical conduct. I also declare that, as required by these rules and conduct, I have fully cited and referenced all material and results that are not original to this work.

Name, Last name : Oubaida, Taji

Signature :

ABSTRACT

POWER GENERATION FROM LOW TEMPERATURE LIQUID DOMINATED GEOTHERMAL SYSTEMS UTILIZING A BINARY POWER PLANT

Taji, Oubaida

Master of Science, Sustainable Environment and Energy Systems Program

Supervisor: Asst. Prof. Dr. Doruk Alp

Co-Supervisor: Prof. Dr. Mahmut Parlaktuna

August 2022, 176 pages

Sustainable and renewable energy became of great importance in a world threatened by its climate change and its ever-increasing population. Among the sustainable, renewable, and environmentally friendly energy sources, namely solar, wind, wave and tide, geothermal energy distinguishes itself as it provides supply and storage security. In this study, an explicit, analytical spreadsheet model has been developed, estimating the power generated from a binary power plant utilizing low temperature liquid-dominated geothermal system. Production from a hypothetical reservoir is simulated using a single-tank Lumped-Parameter Model (LPM), which is verified against industry standard TOUGH2 code for a 30-day test period. For the development of the explicit LPM, two new explicit pressure and temperature equations are derived. The developed LPM; can simulate variable production/injection rates at variable injection temperatures, takes into account the conductive and convective heat transfer mechanisms, is coupled with a steady state reservoir flow and thermal wellbore flow models. Four production/injection scenarios have been considered. The case 4, with constant production rate of 1000 kg/s, constant re-injection of 100 kg/s at binary power plant outlet temperature,

achieved the highest power output of $11.5\text{E}+06$ MWh with 81% capacity factor, saving $1.15\text{E}+10$ kg CO₂ equivalent of emissions if same amount of power were to be generated from coal fired plant.

Keywords: Geothermal energy, Low temperature liquid-dominated reservoir, Lumped-Parameter model, Non-isothermal, Single-liquid phase

ÖZ

SIVI BARINDAN DÜŞÜK SICAKLIKLI JEOTERMAL SİSTEMLERDEN İKİLİ SANTRAL İLE GÜÇ ÜRETİMİ

Taji, Oubaida

Yüksek Lisans, Sürdürülebilir Çevre ve Enerji Sistemleri

Tez Yöneticisi: Asst. Prof. Dr. Doruk Alp

Ortak Tez Yöneticisi: Prof. Dr. Mahmut Parlaktuna

Ağustos 2022, 176 sayfa

İklim değişikliği ve herdaim artan nüfusun tehdidi altındaki günümüz dünyasında, sürdürülebilir ve yenilenebilir enerji çok büyük önem arz etmektedir. Jeotermal enerji, sürdürülebilir, yenilenebilir, ve çevre dostu enerji kaynakları olan güneş, rüzgar, dalga ve gelgit arasında arz ve depolama güvenliği sunmasıyla öne çıkmaktadır. Bu çalışmada, düşük sıcaklıkta, sadece sıvı-içeren jeotermal sistemden, ikili-elektrik santrali kullanarak güç üretimini tayin etmek üzere, geçerli denklemlerin açık halinin çözümsel olarak işlendiği, hesap çizelgesi yazılımı temelli bir model geliştirilmiştir.

Ortalama parametreler ile tanımlanan soyut bir rezervuardan üretim, tek-hacim İndirgenmiş (Yuvarlanmış) Parametre Modeli (IPM) ile kurgulanmıştır. Geliştirilen IPM verdiği sonuçlar, jeotermal endüstrisinde dünya standardı olan TOUGH2 araştırma yazılımı ile 30-günlük bir süreç için teyit edilmiştir.

Geliştirilen IPM, rezervuar içinde iletimli ve taşınımli ısı aktarım mekanizmaları ile, rezervuar ve kuyu içinde kararlı-hal eşsıl olmayan akış modelleri içermektedir.

Böylece, değişken sıcaklıklarda, değişken üretim/basım (enjeksiyon) debileri kullanabilmektedir.

Tez sürecinde 4 farklı üretim/basım planı çalışılmıştır. Bunlardan, 1000 kg/saniye sabit üretim ile, ikili-santral çıkış sıcaklığında 100 kg/saniye sabit geri-basım debisi öngören 4. plan, 11.5E+06 MW-saat ve %81 kapasite faktörü ile azami güç üretimi sağlayan plan olmuştur. Eşdeğer elektrik üretimi için, kömür bazlı termik santrale kıyasla 1.15E+10 kg CO₂-dengi salınımı önleyecektir.

Anahtar Kelimeler: Jeotermal Enerji, Düşük Sıcaklık, Sıvı-İçeren/Baskın Rezervuar, İndirgenmiş (Yuvarlanmış) Parametre Modeli, Eşsıl Olmayan, Tek-Faz Sıvı.

*To my brother Omran Dakramanji
and my beloved family*

ACKNOWLEDGMENTS

I would like to express my gratitude to Assoc. Prof. Dr. Emre Artun for his motivating and helpful words, and to the main characters of my story: Alaa Shammaa, Sinan Bellek, Adnan Alhomssi, Sameh Algharabli, Ashihan Mecbure Tok, and Mohamad Hamad, for their amazingness.

I thank my advisor Asst. Prof. Dr. Doruk Alp and my Co-supervisor Prof. Dr. Mahmut Parlaktuna, for their critical feedback and guidance. This work would not be possible without their efforts.

I would like to thank the five jury members for their invaluable comments, Prof. Dr. Salih Saner, Asst. Prof. Dr. Doruk Alp, Prof. Dr. Mahmut Parlaktuna, Assoc. Prof. Dr. Murat Sönmez, and Asst. Prof. Dr. Gamze İpek. Due to some bureaucratic reasons, Assoc. Prof. Dr. Murat Sönmez was not accepted as a jury member later. However, this thesis has been defended against five jury members.

Finally, an honorable quote to end with. **“Nationalism is an infantile disease. It is the measles of mankind”** Albert Einstein.

.

TABLE OF CONTENTS

ABSTRACT.....	v
ÖZ	vii
ACKNOWLEDGMENTS	x
TABLE OF CONTENTS.....	xi
LIST OF TABLES	xiv
LIST OF FIGURES	xv
LIST OF ABBREVIATIONS	xxii
LIST OF SYMBOLS	xxiv
CHAPTERS	
1. INTRODUCTION	1
1.1 The Energy Dilemma	1
1.2 Geothermal Energy	3
1.2.1 Geothermal Energy and Other Renewable Resources	5
1.3 Thesis Objective.....	9
1.4 Organization of the Thesis	10
2. BACKGROUND INFORMATION	11
2.1 Geology of Geothermal Regions	11
2.1.1 The Origin of Earth's Heat.....	12
2.1.2 Tectonic Plates and Their Boundaries.....	13
2.1.3 Heat Transfer Mechanisms within the Earth.....	18
2.2 Geothermal Resources	19
2.2.1 Hydrothermal Resources	20

2.2.2	Non-conventional Geothermal Resources	29
2.3	Utilization of Geothermal Systems	32
2.3.1	Power Generation	33
2.3.2	Direct Use	40
3.	GEOTHERMAL RESERVOIR MODELS	43
3.1	Decline Curve Analysis	44
3.2	Reservoir Simulators or Distributed-Parameter Model	45
3.3	Lumped-Parameter Models	47
3.3.1	Motivation for Lumped-Parameter Models	48
3.3.2	Single-Tank Lumped-Parameter Models	49
3.3.3	Literature Review	51
4.	METHODOLOGY	63
4.1	Input Parameters and Preliminary Calculations	66
4.1.1	Input Parameters	67
4.1.2	Preliminary Calculations.....	69
4.2	Reservoir Model	71
4.2.1	Modified Lumped-Parameter Model	71
4.3	Production Well Model	85
4.3.1	Preliminary Calculations.....	86
4.3.2	Steady State Reservoir-Production Well Model	86
4.3.3	Liquid Steady State Model for the Flow in the Production Well	88
4.4	Binary Power Plant.....	92
4.5	Injection Well Model.....	93
4.5.1	Preliminary Calculations.....	94

4.5.2	Liquid Steady State Model for the Flow in the Injection Well	94
4.6	Postliminary Calculations	96
5.	RESULTS AND DISCUSSION	99
5.1	Inputs.....	99
5.1.1	Preliminary Outputs	101
5.2	Investigated Cases.....	102
5.2.1	Case 1	105
5.2.2	Case 2	124
5.2.3	Other Cases	132
5.3	Summary	142
6.	CONCLUSION.....	145
6.1	Results.....	146
6.2	Future Work and Recommendations.....	147
	REFERENCES	149
	APPENDICES	
A.	Derivation of Schilthuis Method, Eq. 4.12	161
B.	Derivation of Reservoir Pressure Behavior, Eq. 4.14.....	162
C.	Derivation of Reservoir Temperature Behavior, Eq. 4.17.....	164
D.	Steady State Flow in Radial Reservoir Under Production, Eq. 4.33.	167
E.	Steady State Flow in Radial Reservoir Under Injection, Eq. 4.61.....	168
F.	Geothermal Fluid Temperature Behavior in Well.	169
G.	Liquid Flow in Wells.	173
H.	Derivation of Cumulative Recharge	175

LIST OF TABLES

TABLES

Table 1.1. Utilized land area by different energy resources for 30 years (Bronicki & Lax, 2004).....	8
Table 2.1. Geothermal resources classifications based on reservoir temperature criterion (Zarrouk & McLean, 2019).....	24
Table 2.2. Sanyal (2005)'s Classification of hydrothermal resources according to reservoir temperature (Sanyal, 2005).	25
Table 2.3. Applicable power conversion system (power plant) for each hydrothermal resource class of Sanyal (2005).	33
Table 3.1. Summary of the important features of all the LPM models discussed in the literature review, including this study.	61
Table 4.1. Conversion factors (cf) used in this thesis.....	66
Table 4.2. Essential parameters that must be supplied into the developed model. .	68
Table 4.3. Data set used for the verification of Eq. 31 (Satman, 2010).	77
Table 4.4. TOUGH2 model input parameters (Onur et al., 2008).....	82
Table 5.1. Model input parameters.....	100
Table 5.2. Preliminary outputs obtained from the input.....	101
Table 5.3. Summary of the considered production/injection cases in this study, in terms of electricity produced, installed capacity, and capacity factor.....	143
Table 5.4. Levelized cost and land use of all the four cases.	143
Table 6.1. Capacity factor, lifecycle GHG emissions, land use, and levelized cost of Case 4 (geothermal energy – binary) and Coal (IGCC).	146

LIST OF FIGURES

FIGURES

Figure 1.1. World's energy consumption by source in terawatt-hours (TWh) through 1950 to 2019 (Ritchie et al., 2020).	1
Figure 1.2. World's population from 1820 until 2019 (Roser et al., 2013).	2
Figure 1.3. World's power generation installed capacity from geothermal energy from 1975 to 2020. Data is taken from WEC (2013) and Lund et al. (2022) for time periods from 1975 to 1990 and from 1995 to 2020, respectively.	4
Figure 1.4. World's direct use installed capacity from geothermal energy from 1975 to 2020. Data is taken from WEC (2013) and Lund et al. (2022) for time periods from 1975 to 1990 and from 1995 to 2020, respectively.	5
Figure 1.5. Capacity factors of different renewable energy resources (Glassley, 2010).	6
Figure 1.6. Lifecycle greenhouse gas emissions of various renewable and non-renewable energy resources (Edenhofer et al., 2011).	7
Figure 1.7. Levelized cost of different energy resources (Glassley, 2010).	8
Figure 2.1. Planet Earth's layers and their thicknesses (Barbier, 2002).	11
Figure 2.2. The lithospheric plates, their movement direction indicated by the arrows, operating geothermal fields indicated by the triangles (1 in the legend), unexploited geothermal fields indicated by the circles (2 in the legend), mid-oceanic ridges crossed by transform faults (3 in the legend), and subduction zones (4 in the legend) (Barbier, 2002).	14
Figure 2.3. Schematic description of the various types of possible interactions that could result from tensional and compressional stresses (DiPippo, 2008).	16
Figure 2.4. Schematic illustration of a divergent and convergent plate boundaries with their resultant geologic events (Barbier, 1997).	16
Figure 2.5. Simple Schematic illustration of a transform (conservative) plate boundary (Math/Science Nucleus, n.d.)	18

Figure 2.6. Schematic of a pan filled with water in direct contact with the stove (Libretexts, 2020).	19
Figure 2.7. Schematic representation of a hydrothermal geothermal system (Dickson & Fanelli, 2003).	21
Figure 2.8. Schematic illustration of geothermal hydrothermal system (Dickson & Fanelli, 2003).	23
Figure 2.9. Classification scheme on pressure-enthalpy-temperature diagram of pure water (Sanyal, 2005).	26
Figure 2.10. Temperature profile through the Alpine fault, New Zealand (Zarrouk & McLean, 2019).	27
Figure 2.11. Temperature profile of well 6-2 in East Mesa hydrothermal system, U.S. (Zarrouk & McLean, 2019).	28
Figure 2.12. Schematic illustration of an EGS/HDR system (DiPippo, 2008).	29
Figure 2.13. Schematic illustration for a cross-section of a geopressed system (DiPippo, 2008).	30
Figure 2.14. Schematic illustration for extracting the thermal energy contained in magma (Aydemir, 2021).	31
Figure 2.15. Lindal diagram relates the suitable application based on geothermal fluid temperature. Original diagram is on the left (Lindal, 1973), and a modified one by Haklidir & Haklidir (2020) is on the right.	32
Figure 2.16. Simplified Schematic diagram of a steam power plant (DiPippo, 1998).	34
Figure 2.17. Simplified Schematic diagram of a single-flash power plant (DiPippo, 1998).	35
Figure 2.18. Simplified Schematic diagram of a double-flash power plant (DiPippo, 1998).	36
Figure 2.19. kgCO ₂ /kWh for various energy resources (Bronicki & Lax, 2004).	37
Figure 2.20. Simplified Schematic diagram of a binary power plant (DiPippo, 1998).	38

Figure 2.21. Geothermal district heating systems are of two types, open loop type (top), and closed loop type (bottom) (Edenhofer et al., 2011).....	41
Figure 3.1. Production rate vs time fitted by the exponential, hyperbolic, and harmonic decline equations (Ripperda & Bodvarsson, 1987).	45
Figure 3.2. Example of a conceptual model built using a number of cells or tanks (Alcott et al., 2012).	47
Figure 3.3. Three various lumped-parameter models where; case (a) is a single-tank LPM, Case (b) is a two-tank LPM, Case (c) is a three-tank LPM (Sarak et al., 2005).	48
Figure 3.4. One tank, cell, or control volume lumped-parameter model for hot water hydrothermal systems.	49
Figure 3.5. Reservoir pressure history of Wairakei geothermal reservoir from 1956 to 1961 matched by the model of Whiting & Ramey Jr. (1969). The model was used to predict and forecast the future performance of the reservoir Whiting & Ramey Jr. (1969).	52
Figure 3.6. Reservoir representation of Castanier et al. (1980) analytical model divided into three distinctive radial zones; central, intermediate, and outer zone. .	53
Figure 4.1. Illustration; of the LPM developed in this study for low temperature geothermal system, and the developed model. The numbers correspond to the geothermal fluid state (pressure, temperature) at different points.	65
Figure 4.2. Top view of a radial aquifer surrounding radial reservoir.....	72
Figure 4.3. Net production rate scenario used for verification of Eq. 4.14 results.	76
Figure 4.4. Verification of the results obtained using the derived Eq. 4.14 in this study against the results of Eq. 3.13 of Sarak et al. (2005)'s.....	76
Figure 4.5. Results of reservoir Pressure obtained using Satman's Model and this study's LPM for the first 80 years production period.....	78
Figure 4.6. Results of reservoir temperature obtained using Satman's Model and this study's LPM for the first 80 years production period.....	78
Figure 4.7. Results of reservoir Pressure obtained using Satman's Model and this study's LPM for 80 years of production and another 80 years of shut-in.	80

Figure 4.8. Results of reservoir temperature obtained using Satman's Model and this study's LPM for 80 years of production and another 80 years of shut-in.	80
Figure 4.9. Reservoir model created on PETRASIM to verify the modified LPM used in this study against TOUGH2.	81
Figure 4.10. Production/injection scenario used for the third stage verification (Onur et al., 2008).	83
Figure 4.11. Results of reservoir pressure obtained from TOUGH2, and this study. In addition to error percentage between the results of TOUGH2 and this study. ...	84
Figure 4.12. Results of reservoir temperature obtained from TOUGH2, and this study. In addition to error percentage between the results of TOUGH2 and this study.	85
Figure 4.13. Schematic of radial reservoir, where the fluid flows from the undisturbed far-field reservoir into the well (DiPippo, 2008).....	87
Figure 4.14. Schematic illustration of the top view of the well.	88
Figure 4.15. Side view schematic of a portion of the well (Guo et al, 2013).	89
Figure 5.1. Temperature profile from the surface to the center of the underlying layer at the natural state.	102
Figure 5.2. Illustration; of the LPM developed in this study for low temperature geothermal system, and the developed model for cases from 1 to 4. The numbers correspond to the geothermal fluid state (pressure, temperature) at different points.	104
Figure 5.3. Production/injection scenario, net production rate, recharge rate, and injection temperature of Case 1.	105
Figure 5.4. Reservoir pressure behavior with time in response to Case 1 shown for the first 5 years, and throughout the 30 years.	106
Figure 5.5. Reservoir temperature behavior with time in response to Case 1.	106
Figure 5.6. Cumulative pore volume produced, injected, recharged, and net produced through exploitation for Case 1.	107
Figure 5.7. Cumulative heat produced, heat injected, heat recharged, and net conductive heat as a fraction of the initial reservoir heat content.	108

Figure 5.8. Conductive heat flow; from the underlying layer, to the overlying layer, and net conduction through time.....	109
Figure 5.9. Cumulative conductive heat; gained from the underlaying layer, lost to the overlying layer, and net conduction during the 30 years.	109
Figure 5.10. Number of injection wells and production wells, Production rate of a single production well, and injection rate of a single injection well throughout exploitation time.	110
Figure 5.11. Bottom-hole production pressure throughout exploitation.....	111
Figure 5.12. Fluid density change, computed at reservoir conditions through exploitation time.	111
Figure 5.13. Change of geothermal fluid pressure while it flows through the porous media from the reservoir to the bottomhole of the production well at different instances.	112
Figure 5.14. Downhole production pump and flash horizon depth behaviors with time.	113
Figure 5.15. Change of geothermal fluid saturation pressure, computed at reservoir temperature, through exploitation.	113
Figure 5.16. Wellhead production pressure behavior with time.	114
Figure 5.17. Production well schematic showing flash depth, pressure at the wellhead and pressure at the bottomhole, at the beginning, mid, and end of exploitation. .	115
Figure 5.18. Geothermal fluid temperature change throughout the production well at beginning, middle and end of exploitation.	116
Figure 5.19. Geothermal fluid temperature at the wellhead production and at the reservoir throughout the exploitation.	116
Figure 5.20. Geothermal fluid temperature before and after its heat is utilized by the binary power plant throughout exploitation.	117
Figure 5.21. Wellhead injection pressure, and pressure supplied by the injection pump through exploitation time.	118
Figure 5.22. Change of geothermal fluid density, computed at the power plant outlet, through time.	118

Figure 5.23. Behavior of wellhead injection pressure through exploitation.	119
Figure 5.24. Behavior of bottomhole injection pressure through exploitation.....	119
Figure 5.25. Reservoir pressure and injected fluid pressure after it has reached the reservoir (flow through porous media).....	120
Figure 5.26. Geothermal fluid pressure behavior as it flows through the porous media from the bottomhole of the injection well to the reservoir at various instances....	121
Figure 5.27. <i>T_{out}</i> and bottom hole injection temperature behavior with time.	122
Figure 5.28. Geothermal fluid temperature change throughout the injection well at beginning, middle and end of exploitation.	122
Figure 5.29. Power generated, work of pumps, running capacity and its net behaviors with time.	123
Figure 5.30. Phase diagram of water, and geothermal fluid at multiple conditions throughout its power generation cycle.	124
Figure 5.31. Production/injection scenario, production induced recharge, and injection temperature of Case 2.	125
Figure 5.32. Case 2 utilized production and injection well count, and their single well production and injection rate.	126
Figure 5.33. Response of reservoir pressure to Case 2 production/injection scenario	127
Figure 5.34. Case 2's cumulative; produced PV, injected PV, net produced PV, and recharged PV	127
Figure 5.35. Change of reservoir temperature in response to Case 2 production/injection scenario	128
Figure 5.36. Cumulative; produced heat, gained heat, recharged heat, injected heat, and net conductive heat, of Case 2.	129
Figure 5.37. Change of flash depth, and pressure supplied by the downhole pump, of Case 2 through time.....	130
Figure 5.38. Change of pressure supplied by the injection pump through time....	131
Figure 5.39. Change of; DHP and IP requirements, power, running capacity and its net, in Case 2.	132

Figure 5.40. Change of reservoir pressure with time, in response to Case 3 production/injection scenario.....	133
Figure 5.41. Change of reservoir temperature in Case 3, through exploitation....	134
Figure 5.42. Case 3; requirements of DHP and IP, cumulative power generated, running capacity and its net, through time.....	134
Figure 5.43. Production/injection scenario, injection temperature, and production-induced recharge rate of Case 4.	135
Figure 5.44. Reservoir pressure behavior in response to Case 4 production/injection scenario, through exploitation.....	136
Figure 5.45. Reservoir temperature behavior in response to Case 4 production/injection scenario, through exploitation.	136
Figure 5.46. Case 4's cumulative, produced PV, injected PV, net produced PV, and recharged PV, through time.	137
Figure 5.47. Case 4's cumulative conductive heat; gained from the underlying layer, lost to the overlying layer, and net conduction during the 30 years.	137
Figure 5.48. Case 4's; requirements of DHP and IP, cumulative power generated, running capacity and its net, through time.....	138
Figure 5.49. Reservoir temperature behavior in response to Case 4 and Case 4b through exploitation.	139
Figure 5.50. Reservoir pressure behavior in response to case 4 and 4b through exploitation.	139
Figure 5.51. production-induced recharge rate and injection temperature of Cases 4 and 4b through time.	140
Figure 5.52. Case 4's and 4b's cumulative net conductive heat gained during the 30 years.	141
Figure 5.53. Case 4b's; requirements of DHP and IP, cumulative power generated, running capacity and its net, through time.....	142

LIST OF ABBREVIATIONS

ABBREVIATIONS

Abbreviation	Description
BCV	Ball Check Valve
BPD	Boiling Point Depth
CP	Condensate Pump
CS	Cyclone Separator
CSV	Control and Stop Valve
CWP	Cold Water Pump
DCA	Decline Curve Analysis
DHP	Down Hole Pump
DPM	Distributed Parameter Model
EESI	Environmental and Energy Study Institute
EGS	Engineered Geothermal Resources
FF	Final Filter
GHG	Greenhouse Gas
HDR	Hot Dry Rock
IAPWS	International Association for the Properties of Water and Steam
IGCC	Integrated coal Gasification Combined Cycle
IP	Injection Pump
IW	Injection Well
LHS	Left Hand Side
LPM	Lumped Parameter Model
MR	Moisture Remover
NCG	Non-Condensable Gas
ODE	Ordinary Differential Equation
PDE	Partial Differential Equation

PH	Pre-Heater
PR	Particulate Remover
PSS	Pseudo-Steady State
PV	Pore Volume
PW	Production Well
RHS	Right Hand Side
SE	Steam Ejector
SP	Steam Pipe
SR	Sand Remover
SS	Steady State
TV	Throttle Valve
WEC	World Energy Council
WP	Water or brine Pipe
WV	Wellhead Valve

LIST OF SYMBOLS

SYMBOLS

Symbol	Description	Unit
A_R	Reservoir area	m^2
A_{top}	Cross-sectional area between the overlying layer and the reservoir	m^2
A_{bottom}	Cross-sectional area between the underlying layer and the reservoir	m^2
A_f	Cross-sectional flow area in the well	m^2
b	Decline exponent for DCA	
C_{pw}	Water isobaric heat capacity at reservoir conditions	J/(kg °C)
C_{pwre}	Recharge isobaric heat capacity	J/(kg °C)
C_{pwri}	Injection isobaric heat capacity	J/(kg °C)
C_{pm}	Matrix or rock isobaric heat capacity	J/(kg °C)
C_D	Drawdown coefficient	bar.s/kg
c_f	Fluid compressibility	1/bar
c_r	Matric or rock compressibility	1/bar
c_t	Total compressibility	1/bar
cf	Conversion factor	
D_r	Decline rate for DCA	
D_W	Well diameter	m
d_{top}	Distance between the centers of the overlying layer and the reservoir	m
d_{bottom}	Distance between the centers of the underlying layer and the reservoir	m
E	Electricity produced	MWh
$Error$ (%)	Error percentage	%
\vec{F}	Flow across the domain n boundary	
f	Friction factor	-
G	Geothermal gradient	°C/m

g	Gravitational acceleration constant	m/s^2
HC_i	Initial heat content	J
H_p	Cumulative produced heat	fraction
H_{ri}	Cumulative injected heat	fraction
H_{re}	Cumulative recharged heat	fraction
H_{Qn}	Cumulative net conductive heat	fraction
h_{comp}	Completion thickness	m
h_{in}	Geothermal fluid enthalpy at the power plant inlet	kJ/kg
II	Injectivity index	$\text{kg}/(\text{bar.s})$
J	Productivity index	$\text{kg}/(\text{bar.s})$
K	Component (e.g., heat, mass, water)	
k_A	Aquifer permeability	mD
k_R	Reservoir permeability	mD
M	Accumulation term	
M_p	Produced mass	kg
M_{ri}	Injected mass	kg
M_{re}	Recharged mass	kg
M_{pn}	Net produced mass	kg
\dot{m}_p	Production mass rate from the reservoir	kg/s
$\dot{m}_{p(PW)}$	Production rate from a single production well	kg/s
\dot{m}_{ri}	Injection mass rate	kg/s
$\dot{m}_{ri(IW)}$	Injection rate from a single injection well	kg/s
\dot{m}_{re}	Recharge mass rate	kg/s
\dot{m}_{pn}	Net production mass rate	kg/s
L_A	Aquifer thickness	m
L_R	Reservoir thickness	m
L_W	Well length	m
L_f	Flash horizon	m
L_x	Length of a rectangular reservoir along the x-axis	m
n_p	Number of production wells	-
n_{ri}	Number of injection wells	-

P_{re}	Constant pressure of the recharge source	bar
P_{ri}	Initial reservoir pressure	bar
P_r	Reservoir pressure	bar
$P_{W(PW)}$	Bottomhole production pressure	bar
$P_{W(IW)}$	Bottomhole Injection pressure	bar
$P_{Wh(PW)}$	Wellhead production pressure	bar
$P_{Wh(IW)}$	Wellhead injection pressure	bar
$P_{r(IW)}$	Reservoir pressure from injection	bar
P_{in}	Geothermal fluid pressure at the inlet of the power plant	bar
PV_i	Initial pore volume	fraction
PV_p	Cumulative produced pore volume	fraction
PV_{ri}	Cumulative injected pore volume	fraction
PV_{re}	Cumulative recharged pore volume	fraction
PV_{pn}	Cumulative net produced pore volume	fraction
Q_{top}	Conductive heat loss from the reservoir to the overlying layer	J/s
Q_{bottom}	Conductive heat gain from the underlying layer to the reservoir	J/s
Q_n	Net conductive heat flow	J/s
q_v	Sink or source rate	
q	Production rate for DCA	
q_i	Initial production rate for DCA	
q_{in}	Heat energy entering well element, for LPM	
q_{out}	Heat energy exiting well element	
q_{acc}	Accumulated heat energy in the well element	
q_R	Heat energy transferred through the insulation layer due to conduction	
Re	Reynolds number	-
r_A	Aquifer radius	m
r_R	Reservoir radius	m
r_W	Well radius	m
r_n	Insulation layer inner radius	m
s	Insulation layer thickness	m

T_r	Reservoir temperature	°C
T_{ri}	Initial reservoir temperature	°C
T_{ri}	Injection temperature	°C
T_{re}	Recharge temperature	°C
T_{rp}	Reservoir temperature at the end of the production period	°C
$T_{W(PW)}$	Bottomhole production temperature	°C
$T_{W(IW)}$	Bottomhole injection temperature	°C
$T_{Wh(PW)}$	Wellhead production temperature	°C
$T_{Wh(IW)}$	Wellhead injection temperature	°C
$T_{f,0}$	Medium temperature outside the insulation layer	°C
T_{in}	Geothermal fluid temperature at the inlet of the power plant	°C
T_{out}	Geothermal fluid temperature at the outlet of the power plant, after its thermal energy has been converted to electrical energy	°C
T_{top}	Temperature at the center of the overlying layer	°C
T_{bottom}	Temperature at the center of the underlying layer	°C
T_s	Surface temperature	°C
t	Time	sec
t_p	Production period time	sec
V_n	Volume of domain n	
V_R	Reservoir volume	m ³
v_{PW}	Geothermal fluid flow velocity in the production well	m/s
v_{IW}	Geothermal fluid flow velocity in the injection well	m/s
W	Binary power plant running capacity	MW
W_{DHP}	Downhole pump requirement	MW
W_{IP}	Injection pump requirement	MW
W_{pumps}	Total requirements of all pumps	MW
W_n	Net (actual) running capacity	MW
w	Width of a rectangular reservoir	m
α	Recharge index or recharge constant	kg/(bar. s)

γ_{top}	Conduction index between the overlying layer and the reservoir	(W/°C)
γ_{bottom}	Conduction index between the underlying layer and the reservoir	(W/°C)
ΔP_r	Reservoir pressure drawdown	bar
ΔP_{DHP}	Pressure supplied by the downhole pump to the geothermal fluid	bar
ΔP_{IP}	Pressure supplied by the injection pump to the geothermal fluid	bar
Δt	Time step	sec
ε	Absolute roughness	mm
η_{act}	Conversion efficiency of binary power plant	%
η_{DHP}	Efficiency of downhole pump	fraction
η_{IP}	Efficiency of injection pump	fraction
κ	Storage capacity	kg/bar
λ_R	Reservoir thermal conductivity	W/(m C°)
λ_{top}	Thermal conductivity of the overlying layer	W/(m C°)
λ_{bottom}	Thermal conductivity of the underlying layer	W/(m C°)
$\lambda_{A_{top}}$	Average thermal conductivity of the overlying layer and the reservoir	W/(m C°)
$\lambda_{A_{bottom}}$	Average thermal conductivity of the underlying layer and the reservoir	W/(m C°)
λ_n	Thermal conductivity of the insulation layer	W/(m C°)
μ_w	Water viscosity	bar.s
ρ_m	Matrix or rock density	kg/m ³
ρ_w	Water density	kg/m ³
$\rho_{av} C_{av}$	Reservoir volumetric heat capacity	J/(m ³ °C)
τ_n	Boundary area of domain n	
ϕ_r	Rock porosity	fraction
ϕ_i	Initial rock porosity	fraction

CHAPTER 1

INTRODUCTION

1.1 The Energy Dilemma

The world is going through an energy dilemma that threatens the future on Earth. Coal, crude oil, and natural gas (known as fossil fuels), have been the main resources of energy for more than 150 years, supplying 80% of the world's energy as shown in Figure 1.1 (EESI, n.d.). These resources, however, are harmful to the environment on one hand. On the other hand, more energy must be supplied in order to satisfy the demand of the ever-growing population as shown in Figure 1.2, where the world's population started to increase significantly since 1950. This significant increase can also be noted in Figure 1.1 in terms of energy consumption.

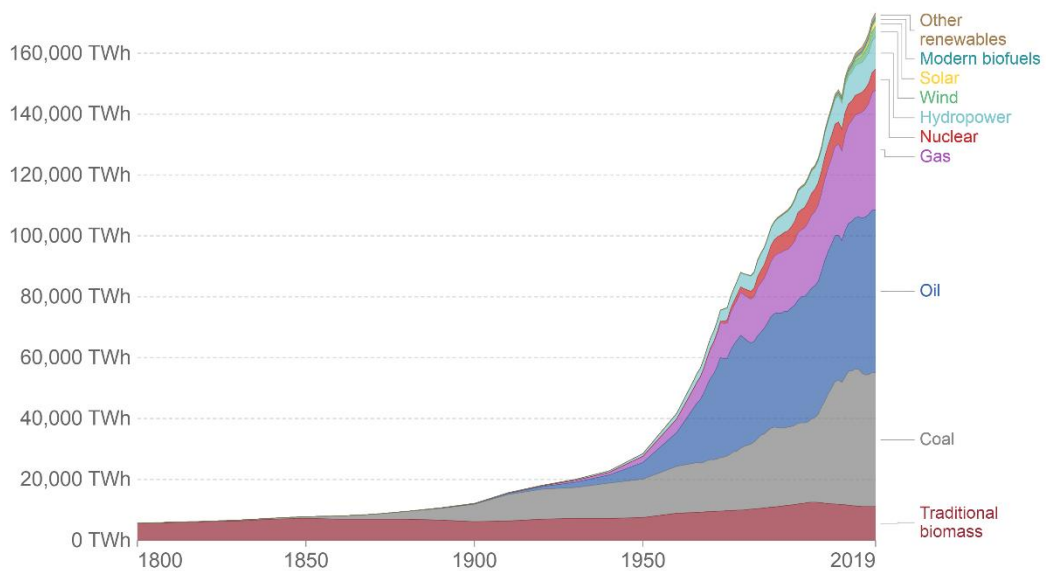


Figure 1.1. World's energy consumption by source in terawatt-hours (TWh) through 1950 to 2019 (Ritchie et al., 2020).

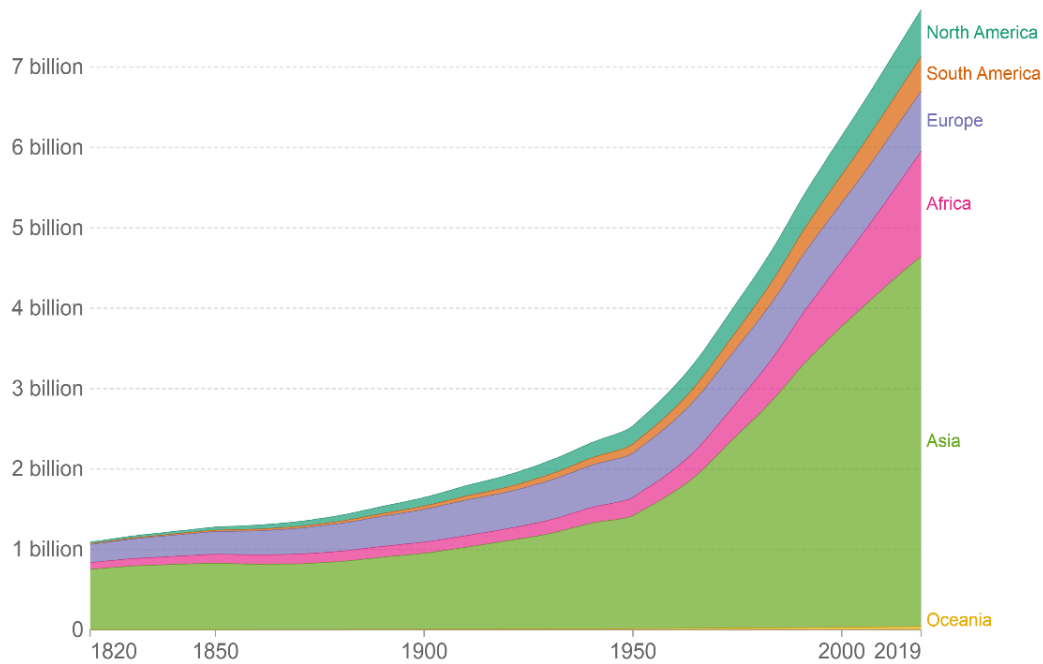


Figure 1.2. World's population from 1820 until 2019 (Roser et al., 2013).

The problem in generating electricity from fossil fuels lies in the release of large amounts of Carbon dioxide (CO₂) gas into the atmosphere during the combustion process. This gas is one of the Green House Gases (GHG), which trap heat in the atmosphere. CO₂ is the primary GHG emitted by human activities and the dominant reason for global warming as 89% of global CO₂ emissions are from fossil fuels and industry (Client Earth, 2020). Concentration level of CO₂ in the atmosphere has reached 414.72 ppm (Lindsey, 2022), accompanied by a 1 Celsius degree increase in global average temperature, a phenomenon known today as the global warming (Client Earth, 2020).

The increase in global temperature (global warming) is causing an alteration in climate (climate change). The following are some of the consequences of climate change:

- The melting of ice sheets and glaciers, and the expansion of water, due to higher temperatures is causing sea level to increase. This leads to the flooding of low-lying coastal areas (Nunez & National Geographic Staff, 2019), and the pollution of fresh groundwater reservoirs (BradFord, n.d.).
- Enhanced evaporation rates and precipitation rates leading to more extreme droughts (center for climate and energy solutions, n.d.) and floods (Matawal & Maton, 2013).
- More intense tropical cyclones would result from the increased temperature of ocean surface (Chung et al., 2021).
- Increased diseases and infections (Matawal & Maton, 2013).

As a result, the international community has moved towards limiting the increase of global average temperature to less than 2 degrees Celsius (to 1.5 degrees Celsius preferably) by binding to the Paris agreement in 2015 (United Nations, n.d.). To accomplish this goal, governments are shifting their energy resources from fossil fuels into more sustainable and renewable energy sources such as solar, wind, hydro, and geothermal energies.

1.2 Geothermal Energy

Geothermal energy – Earth heat – utilizes the thermal energy contained in planet Earth. Heat moves from the center of the Earth towards the surface, with an average geothermal gradient of 30 °C/km (Barbier, 2002). However, in certain areas of the Earth’s crust, geothermal gradients higher than 100 °C/km can be found (Zarrouk & McLean, 2019).

Historically, Geothermal energy was used by many civilizations. The Greeks, Chinese, Romans, Indians, Indigenous civilizations of Mexico, and Japanese, have all used the hot waters of springs as it was believed that it has healing properties. Arabs and Turks used these waters for the thermal baths developing what is known today as “The Turkish Bath”. Thermal springs were also used by the Romans for

recreational purposes. In 14th century, the earliest residential heating utilizing geothermal water directly in the world, took place in France. The use of geothermal resources was not an uncommon practice for humanity. However, generating electricity from geothermal resources is relatively recent dating back to 1904 in Italy, when five light bulbs were lighted up by natural steam using a steam engine connected to a dynamo. Following that, the first commercial geothermal power plant was built with an installed capacity of 250 kW_e in Larderello, Italy, 1913 (Barbier, 2002). After that, the evolution of power generation from geothermal resources started as shown in Figure 1.3. The world's direct use installed capacity in MW_t (Mega-Watt thermal) is shown in Figure 1.4.

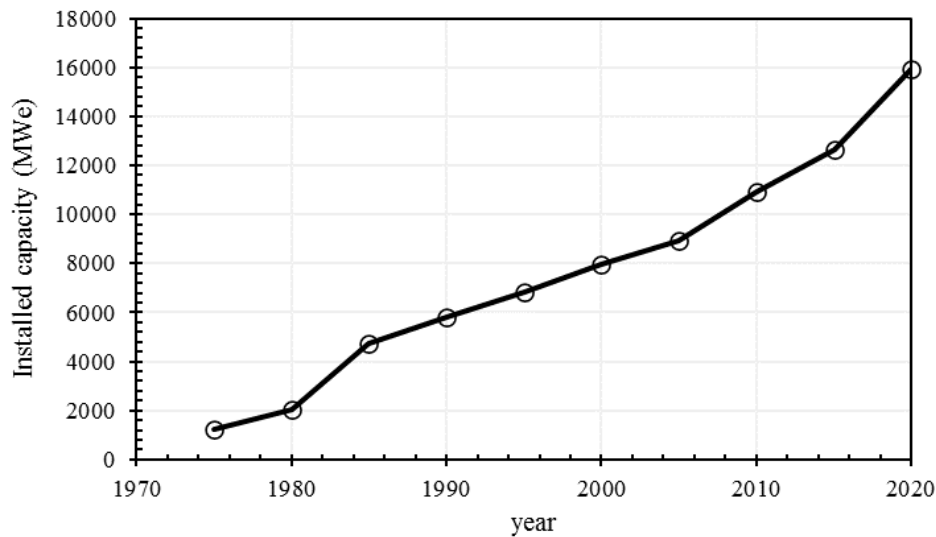


Figure 1.3. World's power generation installed capacity from geothermal energy from 1975 to 2020. Data is taken from WEC (2013) and Lund et al. (2022) for time periods from 1975 to 1990 and from 1995 to 2020, respectively.

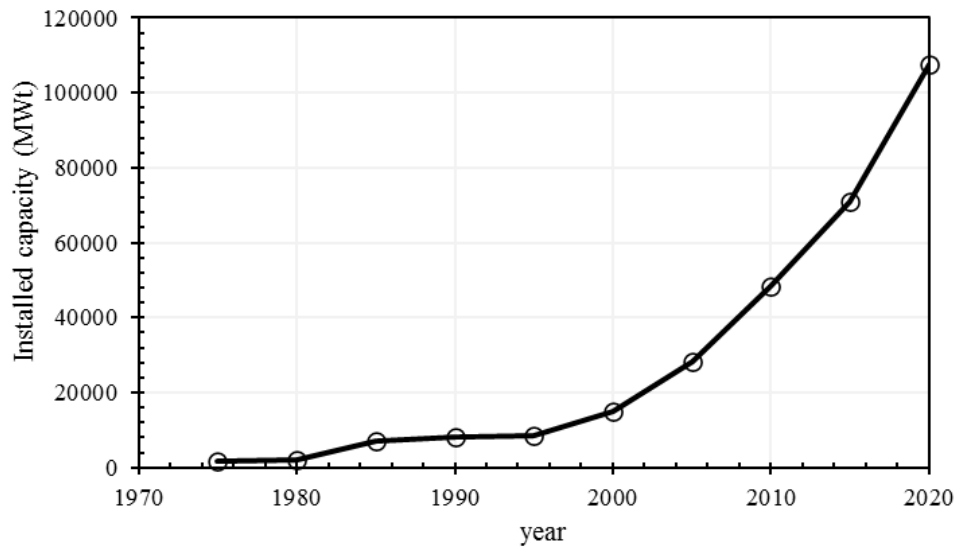


Figure 1.4. World's direct use installed capacity from geothermal energy from 1975 to 2020. Data is taken from WEC (2013) and Lund et al. (2022) for time periods from 1975 to 1990 and from 1995 to 2020, respectively.

1.2.1 Geothermal Energy and Other Renewable Resources

Geothermal energy has many advantages over other renewable energy resources such as solar and wind energies. Solar and wind energies are intermittent energy resources (Glassley, 2010). In simpler words, they are not always available. Solar and wind power plants produce power from the solar radiation and the kinetic energy of wind, respectively. Thus, wind and solar power plants cannot provide the baseload capability, which is the minimum amount of power the supplier must provide to its customers. Their intermittency also negatively affects their capacity factors (Rybach, 2010). On the other hand, geothermal energy is not intermittent since it is always available, enabling it to contribute to the baseload supply system (Glassley, 2010), and to have a high capacity factor.

Capacity factor is the amount of power produced for a period of time over the amount of power that would have been produced given that the power plant was operating at

its installed capacity (ideal conditions) for the same duration. As shown in Figure 1.5, capacity factor of geothermal power plants is the highest (around 90%) regardless of its type, relative to the other energy resources (Glassley, 2010).

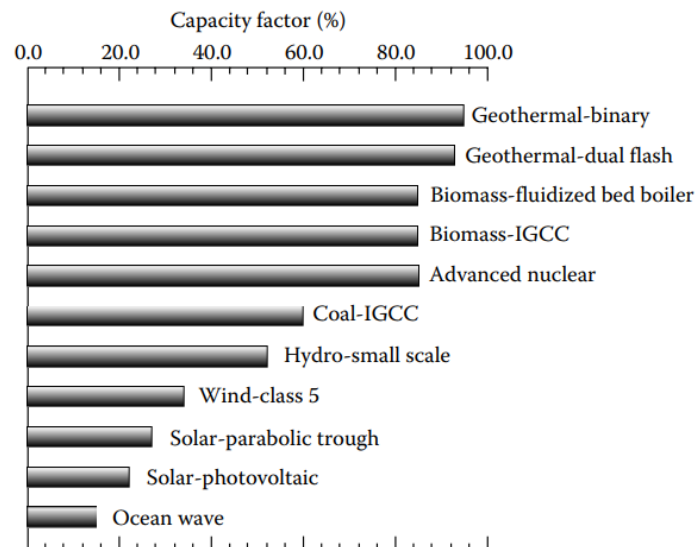


Figure 1.5. Capacity factors of different renewable energy resources (Glassley, 2010).

Geothermal energy is more environment friendly compared to other renewable energy resources. Figure 1.6 shows the lifecycle greenhouse gas emissions for different energy resources in CO₂ equivalent per kWh. Geothermal energy is the third after ocean energy and hydropower in terms of the least carbon footprint per kWh produced. Moreover, compared to other energy resources, the utilized land area by geothermal for a 30-year period is the least as shown in Table 1.1.

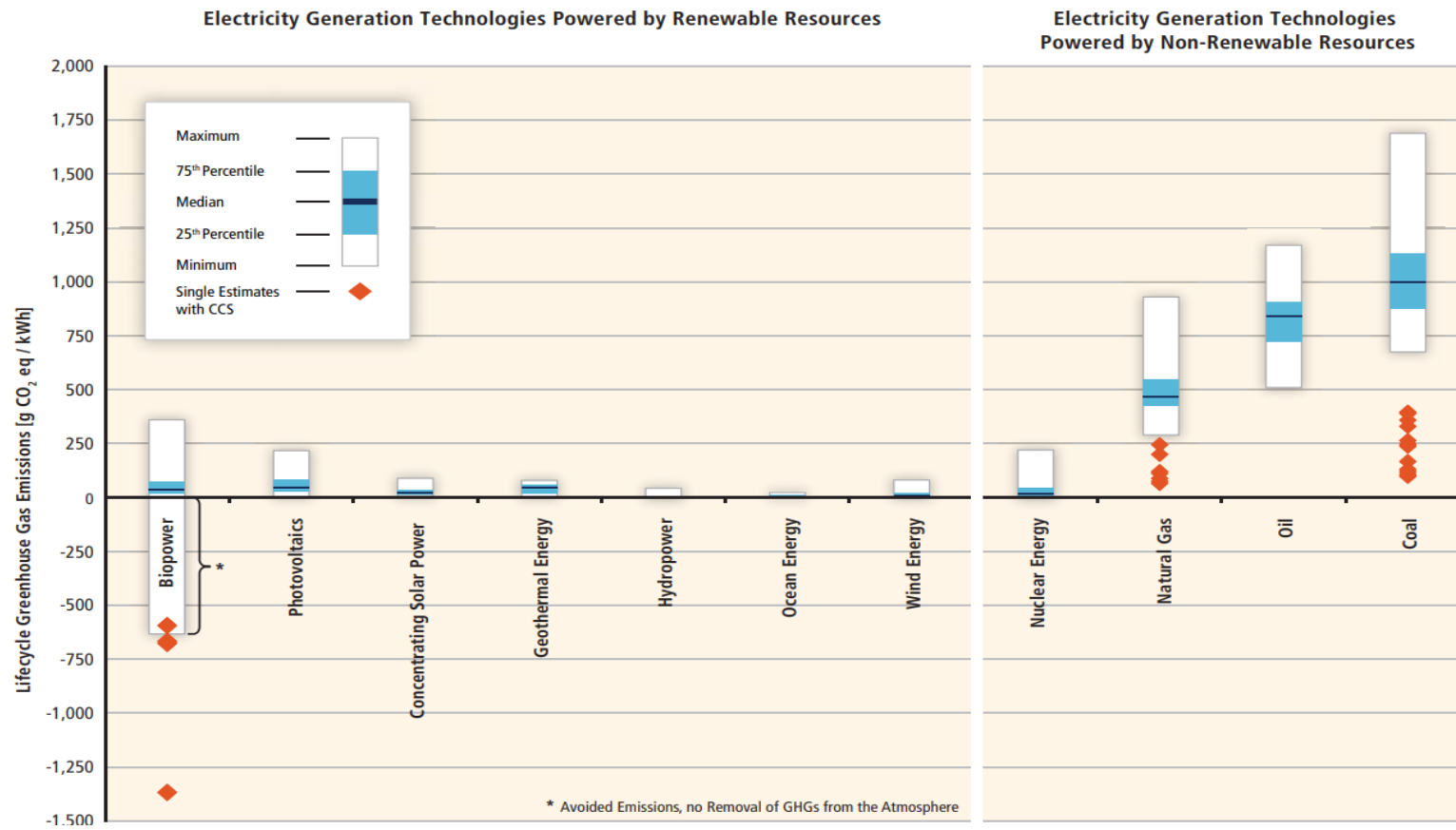


Figure 1.6. Lifecycle greenhouse gas emissions of various renewable and non-renewable energy resources (Edenhofer et al., 2011).

Table 1.1. Utilized land area by different energy resources for 30 years (Bronicki & Lax, 2004).

Technology	Land occupied in m ² /GWh/yr for 30 years
Coal (including mining)	3 642
Solar thermal	3 561
Photovoltaics	3 237
Wind (turbines and roads)	1 335
Geothermal	404

From an economic perspective, geothermal power plants have the least levelized cost compared to the other power plants. Levelized cost is the minimum cost put for selling the generated power so the power plant breaks even (its revenues equals its costs) (Glassley, 2010). Geothermal power plants regardless of its type, and wind power plants, have a levelized cost equal to 6.5 cents/kWh as shown in Figure 1.7.

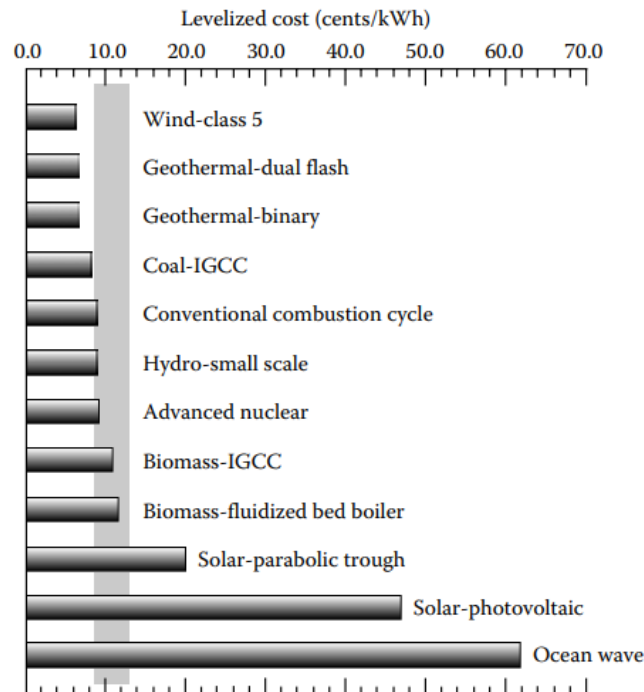


Figure 1.7. Levelized cost of different energy resources (Glassley, 2010).

According to United Nations Development Programme (2000), geothermal energy has the highest potential of 5000 EJ¹/year followed by solar (1575 EJ/year) and wind (640 EJ/year), respectively.

1.3 Thesis Objective

Many parameters affect the production capacity of a hydrothermal geothermal reservoir. Reservoir pressure and temperature are a function of many parameters such as: production rate, injection rate, production induced recharge, conduction, convection, reservoir volume, aquifer permeability, etc. (Axelsson, 2016). The primary goal of this study is to develop a tool that simulates the behavior of a low temperature hydrothermal reservoir under exploitation utilizing a binary power plant. The tool should predict geothermal fluid condition (pressure and temperature) from the reservoir to the binary power plant through production wells, and back to the reservoir through injection wells. The secondary goal is to find the production/injection scenario in which the power generation is optimized for a period of 30 years. The secondary goal would answer the following questions:

- What is the production rate scenario?
- Should injection occur? If yes, what is the injection rate and the injection temperature scenario?
- Should we ever shut-in the reservoir (no production/injection) within the 30 years?

¹ 1 Exajoule (EJ) = 1E+9 Gigajoule (GJ)

1.4 Organization of the Thesis

This thesis is organized in the following manner:

- Chapter 2: discusses background information regarding the geology of geothermal energy, type of geothermal resources, and their applications
- Chapter 3: presents geothermal reservoir modelling methods, detailing Lumped Parameter Model in explanation and literature review.
- Chapter 4: discusses the methodology followed in this study
- Chapter 5: results and discussion.
- Chapter 6: conclusion and recommendations.

CHAPTER 2

BACKGROUND INFORMATION

This chapter presents background information regarding geology of geothermal resources, their types, and industrial applications for these resources.

2.1 Geology of Geothermal Regions

Planet Earth is composed of multiple various layers grouped into four main sections: crust, mantle, outer core, and inner core as shown in Figure 2.1. The pressure at the Earth's center is around 3.6 million bar, and the temperature in the core is approximately 4000 °C (Barbier, 2002). The formation process of planet Earth explains the significantly high temperature in Earth's core.

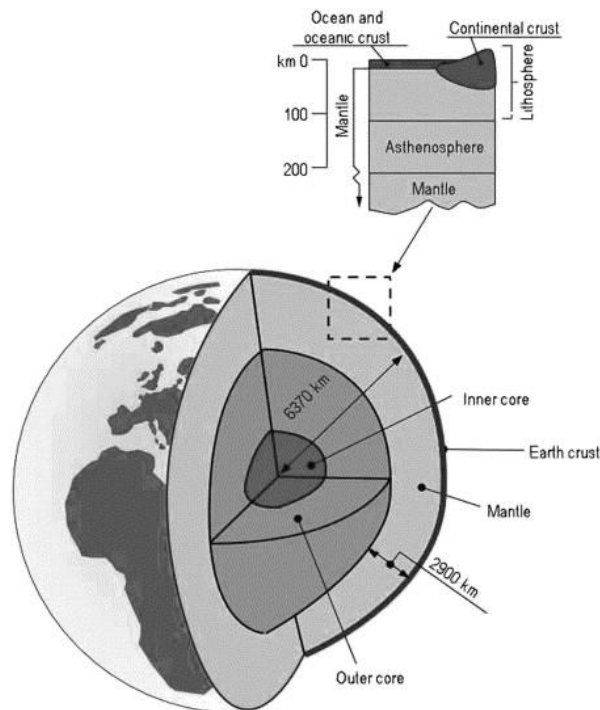


Figure 2.1. Planet Earth's layers and their thicknesses (Barbier, 2002).

2.1.1 The Origin of Earth's Heat

Planet Earth, came into existence 4.56 billion years ago (Göpel et al., 1994; Allegre et al., 1995), has formed from the solar nebula by the condensation of sand-sized particles, dust, and other objects (Chambers, 2001; Yin et al., 2002). These materials were composed of minerals (mainly silicates), metals (mainly iron), and frozen volatiles (e.g., water and simple hydrocarbons). During the accumulation of material, the internal heat of the planet was increasing due to, the conversion of the kinetic energy of the incoming particles into heat after the collision with the planet surface, and the increasing internal pressure as material was being accreted.

Furthermore, the early solar nebula had significant amount of radioactive elements of short half-lives². Once a radioactive element decays, it releases heat. These short-lived radioactive minerals also contributed substantially in increasing the planet's internal heat.

Due to all these preceding processes, the internal temperature of the planet exceeded the melting temperature of iron, resulting to the movement of liquid iron to the inner core of the planet due to its mobility and high density relative to the silicates with which it was in contact. The migration of iron into the planet's inner core caused the release of its gravitational potential energy, which also contributed in increasing the internal temperature of the earth. The liquid iron core has cooled and solidified with time creating the inner solid core of the earth. The inner core has been slowly cooling and extending in radius, while the liquid outer core is diminishing in size (Glassley, 2010).

Approximately 40% of the heat used in geothermal applications derives from the remnant heat from Earth's formation (Stein, 1995). The rest 60% derives from the decay of four long-lived highly radioactive elements: potassium (K), thorium (Th),

² half-life is the amount of time needed for half of a radioactive element to decay.

uranium (U), and rubidium (Rb). These elements are located in the crust (mainly, in the continental crust) (Glassley, 2010).

2.1.2 Tectonic Plates and Their Boundaries

Planet Earth's crust is divided into two parts: continental crust and oceanic crust (Figure 2.1). The mantle, located underneath the crust, makes up 80% of the Earth's volume and its chemical composition is the same throughout the 2900 km thickness it occupies (Thompson & Turk, 1998). It is composed of relatively high density, and low-in-silica minerals. In other words, it does not accommodate the long-lived highly radioactive elements (K, Th, U, and Rb) due to the high pressures in Earth's interior (Glassley, 2010). The low-density radioactive elements (such as K, Th, U, Rb) are accumulated in the continental crust, making it the largest reservoir of radioactive elements (Shih, 1971).

As pressure and temperature increase with depth, they do affect the strength of the mantle. The upper part of the mantle is composed of two layers: the lithosphere (Greek for "rock layer"), which includes the crust, and the asthenosphere. The mantle in the lithosphere is relatively hard and cool while the mantle in the asthenosphere is hotter, weaker, and plastic. 1 to 2% of the mantle in the asthenosphere is liquid. Due to its plasticity, the asthenosphere flows in a rate of few centimeters per year (Thompson & Turk, 1998).

The thickness of the lithosphere layer differs from 100-125 km under continents and about 70 km under oceans. The lithosphere is divided into multiple plates (several small ones and 7 large ones) termed as the lithospheric plates or tectonic plates (Figure 2.2). These plates move freely at very slow rates and thus could crash or move away from each other depending on the plates relative motion. The arrows in Figure 2.2 show the movement direction of each plate (Thompson & Turk, 1998).

It can be noted from Figure 2.2 that most of the exploited and unexploited geothermal fields are located near the plate boundaries (Gupta & Roy, 2006; Bronicki & Lax, 2004).

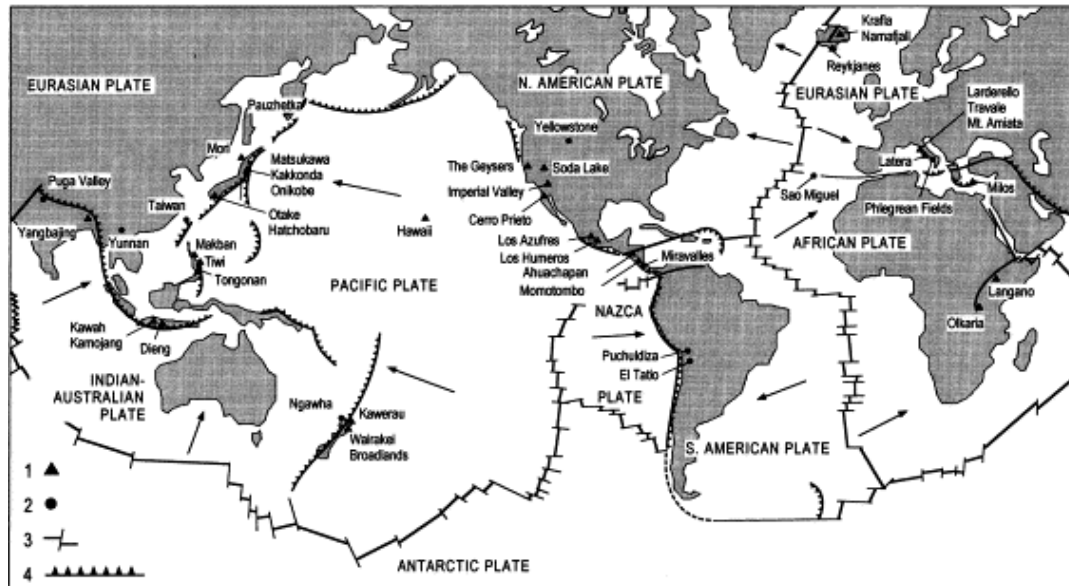


Figure 2.2. The lithospheric plates, their movement direction indicated by the arrows, operating geothermal fields indicated by the triangles (1 in the legend), unexploited geothermal fields indicated by the circles (2 in the legend), mid-oceanic ridges crossed by transform faults (3 in the legend), and subduction zones (4 in the legend) (Barbier, 2002).

Due to the movement of the lithospheric plates, three different types of plate boundaries, where tectonic plates meet, could occur (Thompson & Turk, 1998):

- divergent plate boundary: two lithospheric plates move away from each other developing tension,
- convergent plate boundary: two lithospheric plates converge into each other developing compression, and
- transform plate boundary: two lithospheric plates slide past each other horizontally while they move in opposite directions developing shear stress.

Transform plate boundary is also called conservative plate boundary as there is no lithosphere destruction or creation at this plate boundary (Barbier, 2002). While lithosphere is created and destroyed at divergent and convergent plate boundaries, respectively. The rate of lithosphere creation and destruction is equal, maintaining global balance (Thompson & Turk, 1998).

All of these three types of plate boundaries generate great forces causing volcanic eruptions, earthquakes, building of mountain ranges, and other geologic events (Thompson & Turk, 1998).

2.1.2.1 Divergent plate boundary

One of the possible interactions resulting from tensional stress at a divergent plate boundary is rifting as shown in Figure 2.3. In rifting, as two lithospheric plates move away from each other, the mantle in the underneath asthenosphere rise into the surface to fill the gap caused by the movement of the two plates. Some of this rising mantle melt into liquid, forming magma, which in turn rise to Earth surface forming a new crust after it cools as shown in Figure 2.4. Most divergent plate boundaries are located in the ocean basins (Thompson & Turk, 1998). Thus, the newly formed oceanic crust is formed from magma, which is low in radioactive elements (Glassley, 2010).

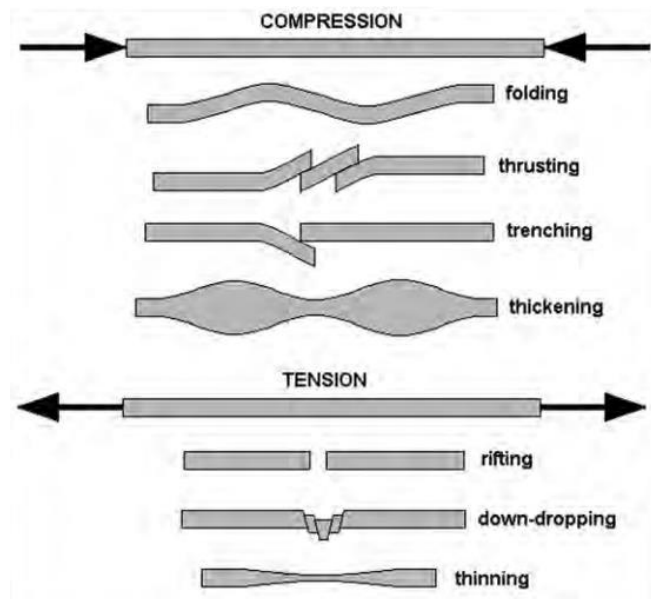


Figure 2.3. Schematic description of the various types of possible interactions that could result from tensional and compressional stresses (DiPippo, 2008).

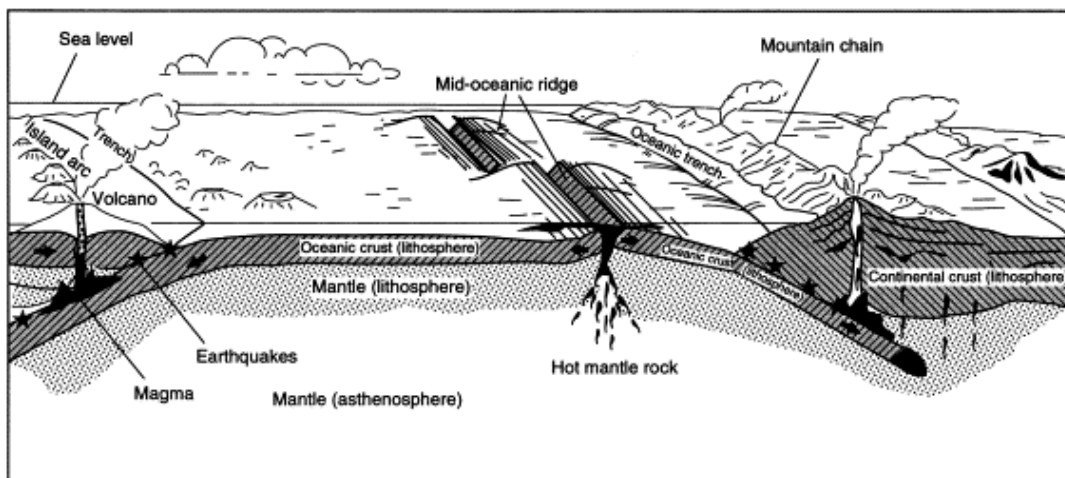


Figure 2.4. Schematic illustration of a divergent and convergent plate boundaries with their resultant geologic events (Barbier, 1997).

One of the most important geologic events that can result from a divergent plate boundary is an undersea mountain chain called mid-oceanic ridge (Thompson & Turk, 1998). If the sea floor is at relatively shallow depth, the undersea mountain chain could rise above sea forming an island as in the case of Iceland, where the Mid-

Atlantic ridge is passing through it (Barbier, 2002). Other possible interactions, that could result from tension, are thinning and down-dropping (horst and graben) as shown in Figure 2.3 (DiPippo, 2008).

2.1.2.2 Convergent Plate Boundary

At convergent plate boundary, two lithospheric plates converge into each other developing compressional stress. One of the possible interactions is trenching or subduction (DiPippo, 2008). In subduction, the denser plate sinks below the lighter plate due to density. As the oceanic crust is denser than the continental plate, the oceanic crust sinks into the mantle as shown in Figure 2.4 (Thompson & Turk, 1998). At the subduction interface, partial melting of the lithosphere give rise to magma due to its lower density and higher temperature relative to the lithospheric rock. This magma intrusion could solidify within the Earth's crust, forming plutons, which offer a great heat source for hydrothermal geothermal systems, and/or could abruptly and violently erupt into the Earth's surface through volcanos (Barbier, 2002; DiPippo, 2008). Other possible interactions resultant from compression are thickening, thrusting, and folding.

One of the most important zones regarding geothermal exploitation, is located at the edges of the Pacific plate or the so called "Pacific Ring of Fire". In general, beneath all land masses in contact with the Cocos, Naza, and Pacific plates, there are subduction zones, except the U.S. and Mexico, where transform boundaries exist (Bronicki & Lax, 2004; DiPippo, 2008). For example; the Pacific and Indian-Australian plates are converging beneath New Zealand, Nazca and South American plates are converging beneath Central America and Chile, Pacific and Eurasian plates are converging beneath Japan (Barbier, 2002).

2.1.2.3 Transform Plate Boundary

When two tectonic plates slide past each other horizontally in the opposite direction as shown in Figure 2.5, they form a transform (conservative) plate boundary, causing earthquakes and/or rock deformations. The boundary between the Pacific plate and North American plate, California's San Andreas fault, is an example of transform plate boundary (Thompson & Turk, 1998).

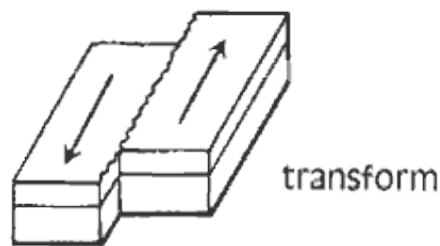


Figure 2.5. Simple Schematic illustration of a transform (conservative) plate boundary (Math/Science Nucleus, n.d.)

2.1.3 Heat Transfer Mechanisms within the Earth

Two types of heat transfer mechanisms take place in the Earth (Barbier, 2002):

- **Conduction:** This type involves the transfer of heat without the transfer of mass, and it is the primary heat transfer mechanism in solids. The introduced heat energy excites the molecules causing them to vibrate, where they strike their neighboring molecules and so on. Hence, the introduced heat energy is transferred through the induced kinetic energy (vibrations) through the molecules. Most rocks are poor conductors relative to metals, which are very good heat conductors.
- **Convection:** Contrary to conduction, convection involves the transport of heat energy with mass, and it is the common heat transfer mechanism in fluids. The heat is transferred due to the movement of the hot fluid from one

place to another. Due to the involved mass transport, convection is vastly more efficient heat transfer mechanism compared to conduction.

Consider a pan, which is in direct contact with the heat source (stove), shown in Figure 2.6. The heat is transferred from the stove through the pan material by conduction. The water at the bottom of the pan heats first, causing it to expand. Thus, its density becomes less relative to the rest of the water mass above. Hence, hot water rises and the cold water sinks in the pan, and so on transferring heat by convection (Libretexts, 2020). The movement of water in currents (hot water rises and cold water sinks) are called convection currents (or convection cells).

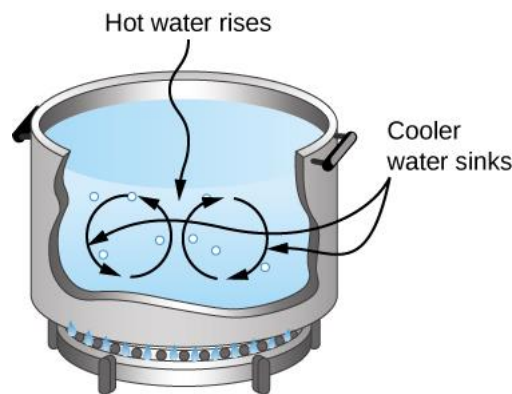


Figure 2.6. Schematic of a pan filled with water in direct contact with the stove (Libretexts, 2020).

2.2 Geothermal Resources

There are different types of geothermal resources, each has its own characteristics. In this section, the conventional hydrothermal geothermal (Dincer & Ozcan, 2018), and the unconventional geothermal resources; Engineered Geothermal Resources (EGS), Geopressured, and magma energy, are explained.

Special emphasis on hydrothermal geothermal resources is given since it is included in the scope of this thesis.

2.2.1 Hydrothermal Resources

Due to heat carrier or heat transport medium being water in this type of resources, they are called “hydrothermal” resources (Norton, 1984; Axelsson, 2016), which are considered the conventional geothermal resources as they are the only type that has been exploited for years and they are reasonably understood (Zarrouk & McLean, 2019). As of 2008, hydrothermal systems are the only resources that have been developed commercially for electric power generation (DiPippo, 2008).

Figure 2.7 shows the ideal hydrothermal system, which consists of the following elements (DiPippo, 2008):

1. heat source such as magma intrusion (at 600 – 1000 °C), or the thinning of the continental crust – the upwelling of crust-mantle boundary to shallower depths, or due to other particular tectonic situations (discussed previously in section 2.1.2) (Barbier, 2002).
2. Water or steam supply in the reservoir to act as the heat carrier.
3. permeable reservoir, which offers paths of lower resistance for fluid flow.
4. cap rock or impervious overlying rock acting as a lid.
5. reliable recharge mechanism.

Please note that these elements are for the ideal hydrothermal system. Hydrothermal resources, or geothermal resources in general, are site-specific (Barbier, 2002; Ganguly & Kumar, 2012). For example, some hydrothermal reservoirs do not contain a cap rock. However, the first, second, and third elements must exist in any hydrothermal reservoir. Without having a heat source, seeping of rainwater deep enough in a normal geothermal gradient can also create a hydrothermal reservoir.

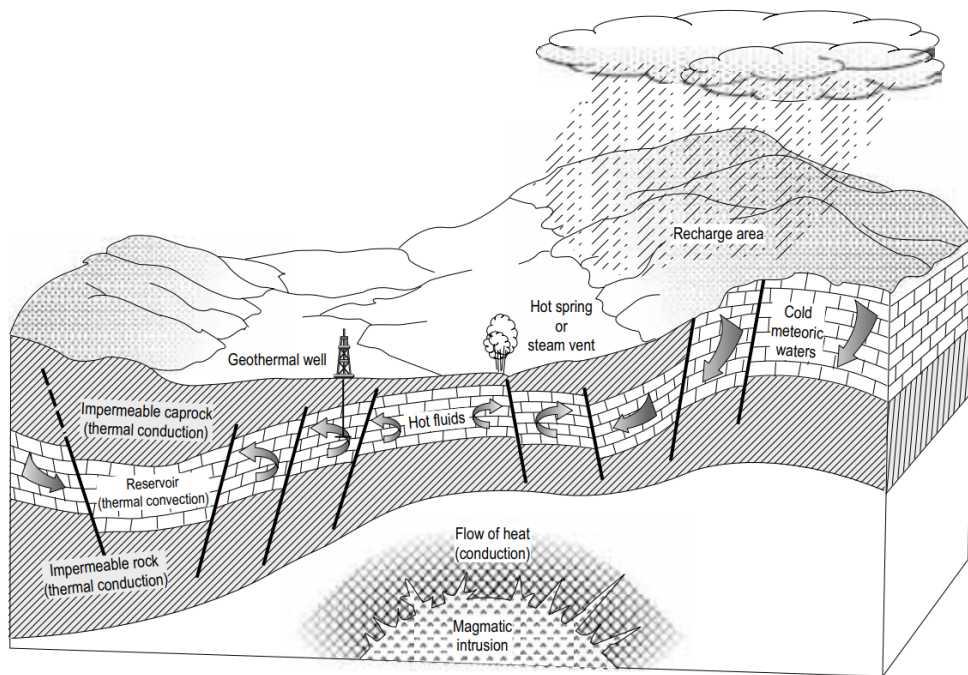


Figure 2.7. Schematic representation of a hydrothermal geothermal system (Dickson & Fanelli, 2003).

Geothermal reservoirs have distinctive features in which they generally extend to a great distance vertically, and their lateral and vertical extent may not be clear (Grant, 2011).

Geothermal fluid often contains dissolved chemicals such as: Arsenic (As), Mercury (Hg), Boron (B), and Sodium Chloride (NaCl), and Non-Condensable Gasses (NCGs) such as Carbon Dioxide (CO_2), Hydrogen Sulfide (H_2S), Methane (CH_4), and Ammonia (NH_3) (Barbier, 2002; Dickson & Fanelli, 2003). As they do not condense at the temperatures of the condenser, and at the pressure of the energy generation cycle, they are called Non-Condensable Gases (NCG's) (Barbier, 2002; DiPippo, 2008). Geothermal fluid composition differs from one field to the other, however. Rarely, the geothermal fluid is composed of freshwater only as the case in Iceland (Dickson & Fanelli, 2003).

Dissolved solids in geothermal fluids and NCG's are pollution sources if discharged to the environment. One of the techniques used to abate this pollution source during exploitation is the reinjection of the geothermal fluid back into the reservoir (Dickson & Fanelli, 2003).

2.2.1.1 The Mechanism of Hydrothermal Systems

The mechanism of a hydrothermal reservoir is shown in Figure 2.8, which can be considered as the front view of Figure 2.7. Relatively cold meteoric water percolates from the surface (Point A) into the formation through faults and fractures. The recharge water arrives to the permeable reservoir (point B), whose rocks have been heated by the conductive heat resultant from the magma intrusion below (Points G, F, and C). The water at the bottom boundary of the reservoir becomes less dense (thermal expansion) than the water at the upper boundary of the reservoir due to the temperature difference, inducing convection currents (cells) that circulate water within the reservoir. Due the high efficiency of convection as a heat transfer mechanism, the temperature difference between the fluid at the top boundary and the bottom boundary is not much. In fact, the lowest geothermal gradient values are found within the reservoir (Barbier, 2002). If the heated water in the reservoir encounters a fault (Point C), it rises to the surface losing pressure. Depending on the water pressure and temperature, it may flash to steam at a certain depth once the water pressure becomes equal to the saturation pressure at a given temperature (Point D). This depth is called the flash depth, or the flash horizon depth (DiPippo, 2008; Glassley, 2010). The steam emerges at the surface (Point E) as geothermal manifestations such as a hot spring, geyser, etc. These surface manifestations give off the location of most geothermal systems (Gupta & Roy, 2006; DiPippo, 2008; Ghosh & Prelas, 2011).

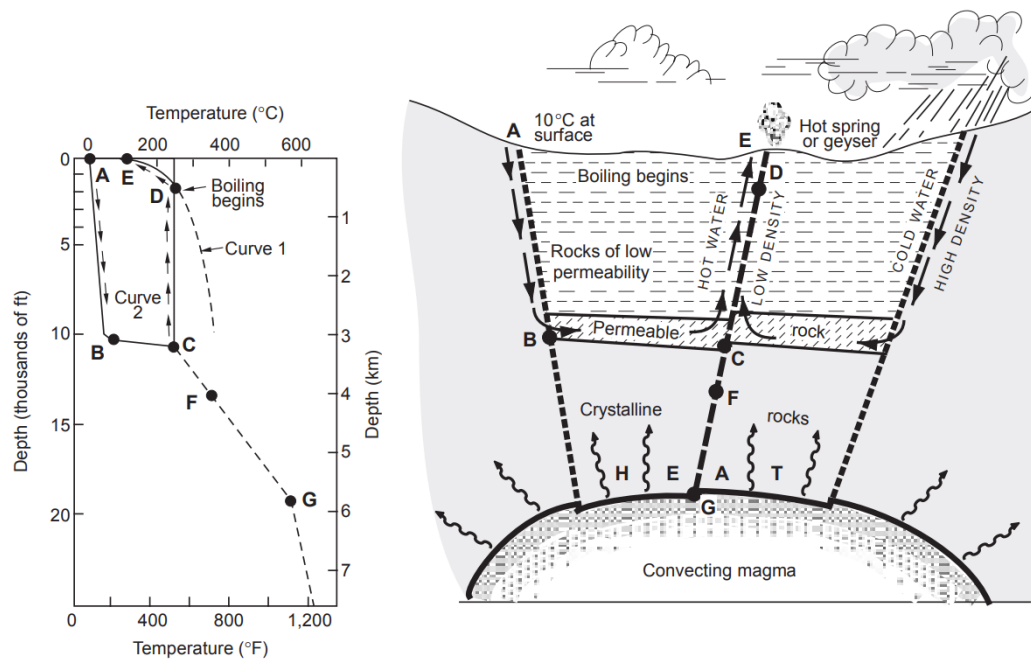


Figure 2.8. Schematic illustration of geothermal hydrothermal system (Dickson & Fanelli, 2003).

2.2.1.2 Classification of Hydrothermal Resources

Unfortunately, there is no consensus regarding common definitions and classifications of geothermal resources as there is no standard international terminology or classification (Dickson & Fanelli, 2003). There are many classifications of geothermal systems based on different criteria, such as: geological circumstances (Moeck et al., 2015), enthalpy (Kaya et al., 2011), reservoir temperature, level of geological knowledge, project status, and feasibility (Zarrouk & McLean, 2019).

Classification based on geothermal temperature is the most common criterion because it's the easiest to understand and measure (Lee, 2001). Table 2.1 shows several classifications that are based on reservoir temperature. The temperature ranges in these classifications are not consistent. The classifications are limited to

hydrothermal resources. According to Zarrouk & McLean (2019) the enthalpy classification (Kaya et al., 2011) is suitable for non-conventional systems.

Table 2.1. Geothermal resources classifications based on reservoir temperature criterion (Zarrouk & McLean, 2019).

Reference	Low- temperature resources (°C)	Intermediate- temperature resources (°C)	High- temperature resources (°C)
Muffler & Cataldi (1978)	< 90	90 – 150	> 150
Rybach (1981)	< 150	–	> 150
Hochstein (1988)	< 125	125 – 225	> 225
Benderitter & Cormy (1990)	< 100	100 – 200	> 200

Sanyal (2005) proposed a more rigorous classification, which was established as part of the national inventory for the U.S., for commercial purposes. In this thesis, Sanyal (2005) classification is used. Traditionally, hydrothermal resources are classified under two main categories, Liquid-dominated systems and vapor-dominated systems, depending on the pressure-controlling mobile phase (Barbier, 2002; Sanyal, 2005; Ganguly & Kumar, 2012). In Sanyal's classification, Classes 1, 2, 3, 4, 5, and 6 are liquid-dominated systems. While Class 7 is vapor-dominated systems as shown in Table 2.2. The scheme is illustrated on pressure-enthalpy-temperature diagram of pure water in Figure 2.9. According to the author, the temperature limits can be shifted by 5 to 10 °C without disturbing the logical structure of the classification.

Table 2.2. Sanyal (2005)'s Classification of hydrothermal resources according to reservoir temperature (Sanyal, 2005).

Resource class	Mobile phase in reservoir	Reservoir temperature (°C)	Production mechanism	Fluid state at wellhead
1. Non-electrical grade	Liquid water	< 100	Artesian self-flowing wells; pumped wells	Liquid water
2. Very low temperature		100 - 150	Pumped wells	Liquid water (for pumped wells) Steam-water mixture (for self-flowing wells)
3. Low temperature		150 - 190	Pumped wells; Self-flowing wells (only at the higher temperature end of the range)	
4. Moderate temperature		190 - 230	Self-flowing wells	Steam-water mixture (enthalpy equal to that of saturated liquid at reservoir temperature)
5. High temperature	Liquid water; Liquid-dominated two phase	230 – 300		Steam-water mixture (enthalpy equal to or higher than that of saturated liquid at reservoir temperature); Saturated steam
6. Ultra-high temperature	Liquid-dominated two phase	> 300		Steam-water mixture (enthalpy equal to or higher than that of saturated liquid at reservoir temperature); Saturated steam; Superheated steam
7. Steam Field	Steam	240 °C (33.5 bar-a pressure; 2800 kJ/kg enthalpy)		Saturated steam; Superheated steam

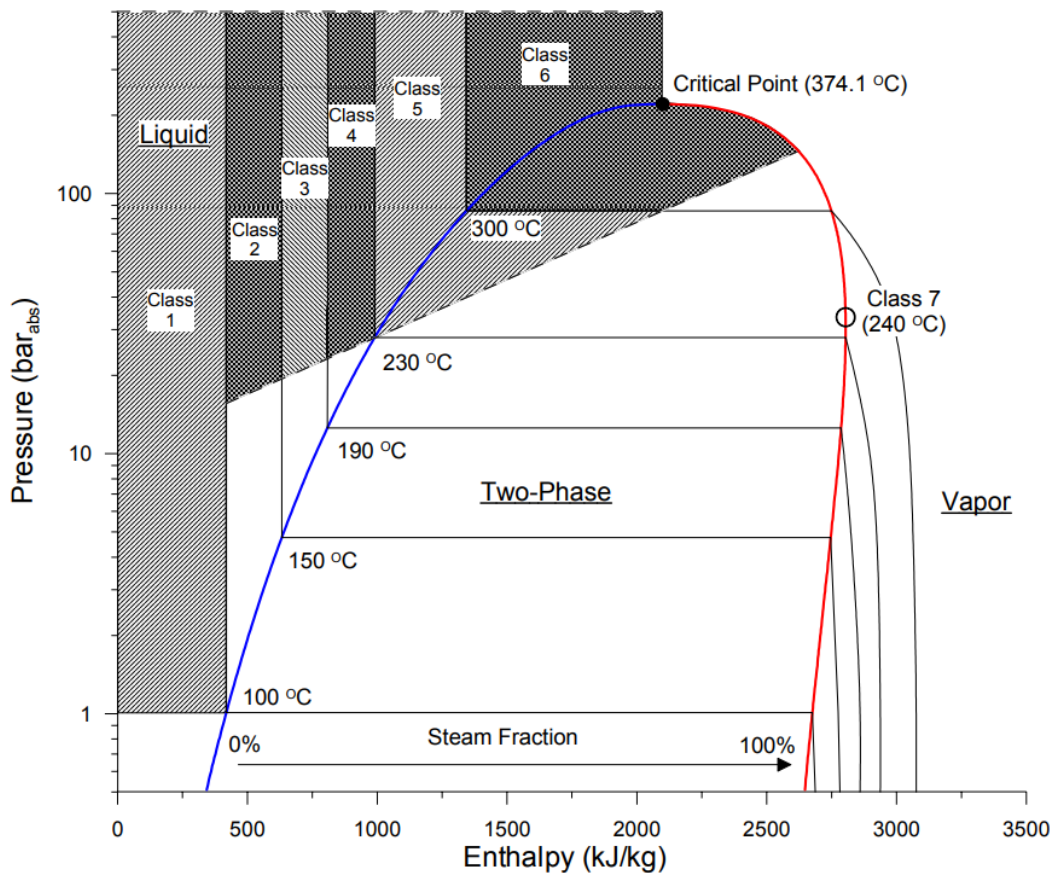


Figure 2.9. Classification scheme on pressure-enthalpy-temperature diagram of pure water (Sanyal, 2005).

2.2.1.2.1 Liquid-Dominated Reservoirs (Classes 1-6)

This is the most common type in hydrothermal resources. The vertical pressure distribution in these reservoirs is near hydrostatic (Grant, 2011). Generally, they have a cap rock but it's not an absolute necessity (Barbier, 2002). Reservoirs at initial conditions of Classes 1, 2, 3, and 4, contain only water even when reservoir pressure decreases during exploitation. While, in Class 5, initial steam cap may exist or develop during exploitation. In Class 6, reservoirs are characterized by the rapid development of steam saturation (Sanyal, 2005).

Low temperature (Class 3) reservoirs, which is included in the scope of this study, is called the “hot water (intermediate temperature)” in the enthalpy criteria classification of Kaya et al. (2011). However, the “hot water (intermediate temperature)” has a different temperature range, from 120 to 220 °C, than Sanyal’s class 3, from 150 to 190 °C. This class’s upper temperature limit is set to be the operating temperature limit for the available commercial downhole pumps, 190 °C (Sanyal et al., 2007). Figure 2.10 shows the temperature profile in such systems, where the conductive heat transfer in the impermeable rock transitions to a much steeper gradient due to the efficient convective heat transfer in the permeable rock (reservoir). The same can be noted in Figure 2.11, which is the temperature profile of well 6-2 in East Mesa (U.S.) plotted against the Boiling Point Depth (BPD, boiling hydrostat) curve. The pressure of these systems will decline during exploitation until there is an induced recharge matching the net production rate. Injection can be very beneficial in these systems to maintain its pressure. Fields in U.S. (East Mesa, Brady), Turkey (Aydin, Buharkent), and Russia (Pauzhetsky) are examples of low temperature (Class 3) hydrothermal resources (Zarrouk & McLean, 2019).

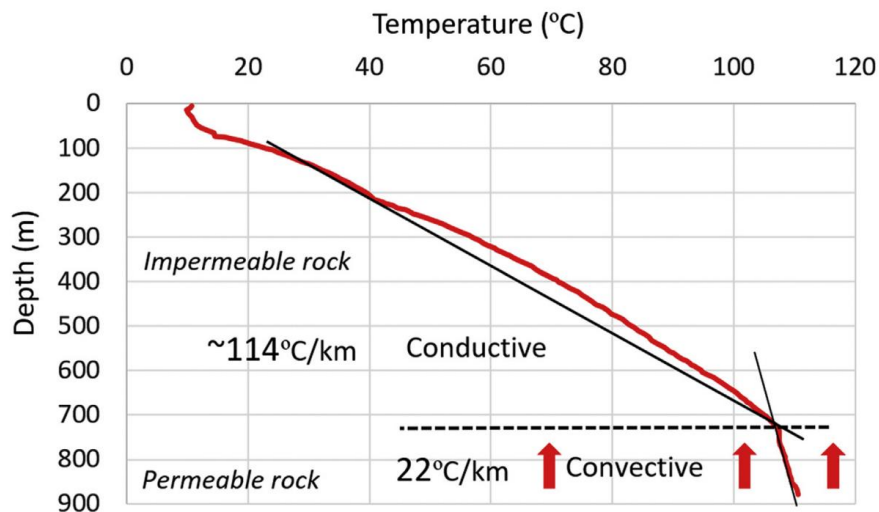


Figure 2.10. Temperature profile through the Alpine fault, New Zealand (Zarrouk & McLean, 2019).

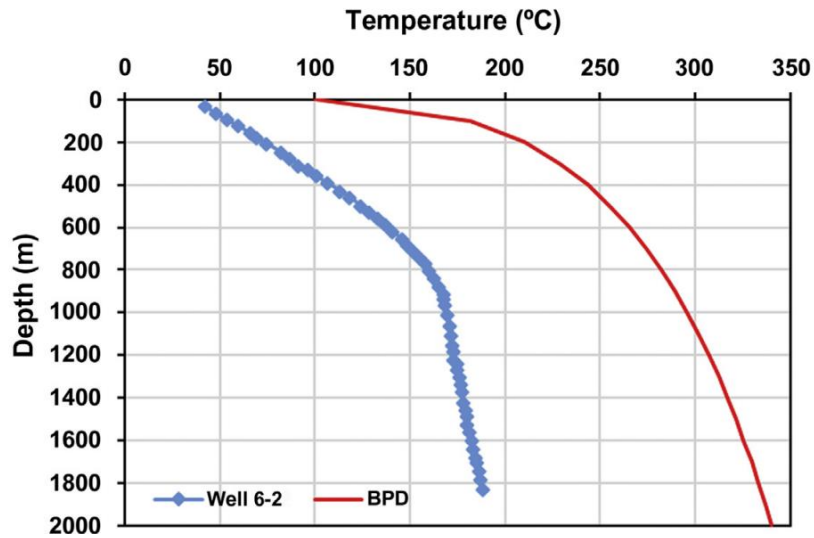


Figure 2.11. Temperature profile of well 6-2 in East Mesa hydrothermal system, U.S. (Zarrouk & McLean, 2019).

2.2.1.2.2 Vapor-Dominated Reservoirs (Class 7)

These reservoirs are very attractive, but rare, since they carry the highest amount of energy per kilogram of fluid extracted (Glassley, 2010). Vapor-dominated geothermal fields, such as Kamojang (Indonesia), Darajat (Indonesia), Larderello (Italy), The Geysers (California), and Mutsukawa (Japan), have all one unique and consistent initial pressure and temperature, around 33.5 bar-a and 240 °C, respectively (Sanyal, 2005). Steam is the mobile pressure-controlling phase (Grant, 2011). The vertical pressure distribution is close to steam-static (Grant, 2011). The existence of a cap rock in this type is a must (Barbier, 2002; Grant, 2014), and the permeability of these systems, in general, is less than the liquid-dominated systems (Barbier, 2002).

2.2.2 Non-conventional Geothermal Resources

Engineered Geothermal Systems (EGS), Geopressed systems, and magma energy are referred to as nonconventional resources due to the fact that they have not been used commercially yet, and they are still in the research and development stage (Zarrouk & McLean, 2019).

2.2.2.1 Engineered Geothermal Systems (EGS)

In hydrothermal resources, Geothermal fluid (water), reservoir permeability, and heat source are provided by nature. In Engineered (or Enhanced) Geothermal Systems (EGS), the hot rock contains insufficient or little natural permeability or fluid saturation (Dickson & Fanelli, 2003; Gupta & Roy, 2006; Dincer & Ozcan, 2018; Zarrouk & McLean, 2019). Because of the low permeability and/or low water saturation EGS was called Hot Dry Rock (HDR) formerly (Bronicki & Lax, 2004). The reservoir is man-made using hydraulic fracturing, chemical fracturing, or explosive fracturing to enhance the rock permeability and fill its fractures with an energy carrier fluid (e.g., cold water), after an injection well has been drilled into the hot rock (Barbier, 2002). Later, a production well is drilled to produce the injected water, which has been heated by the hot rock. The EGS system is shown in Figure 2.12 (Bronicki & Lax, 2004; DiPippo, 2008).

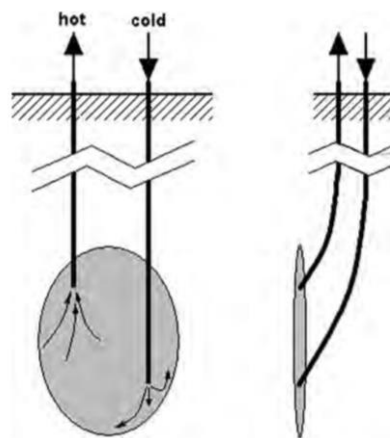


Figure 2.12. Schematic illustration of an EGS/HDR system (DiPippo, 2008).

2.2.2.2 Geopressed Systems

These systems formed through steady deposition of sediments, where subsidence took place in a relatively short geological time interval. The subsidence created steeply dipping faults, which isolates the formation hot water almost completely from the surrounding rock. Moreover, rock layers became more compacted due to the subsidence. A simplified geopressed reservoir is shown in Figure 2.13. These reservoirs are; fairly deep, highly pressurized (around lithostatic pressure gradient 1.0 psi/ft), hot, contain dissolved methane, and analogous to oil and gas reservoirs. The first geopressed system were discovered at a depth between 6-8 km under the Gulf of Mexico with pore pressure of up to 1300 bar (≈ 130 MPa) and temperatures in the range of 150-180 °C. There are three types of energy that can be harvested from geopressed systems: (1) mechanical energy from the high pressure fluid, (2) thermal energy from the fluid's internal energy, and (3) chemical energy by burning the dissolved methane (Barbier, 2002; Bronicki & Lax, 2004; Gupta & Roy, 2006; DiPippo, 2008; Ghosh & Prelas, 2011; Axelsson, 2016; Zarrouk & McLean, 2019).

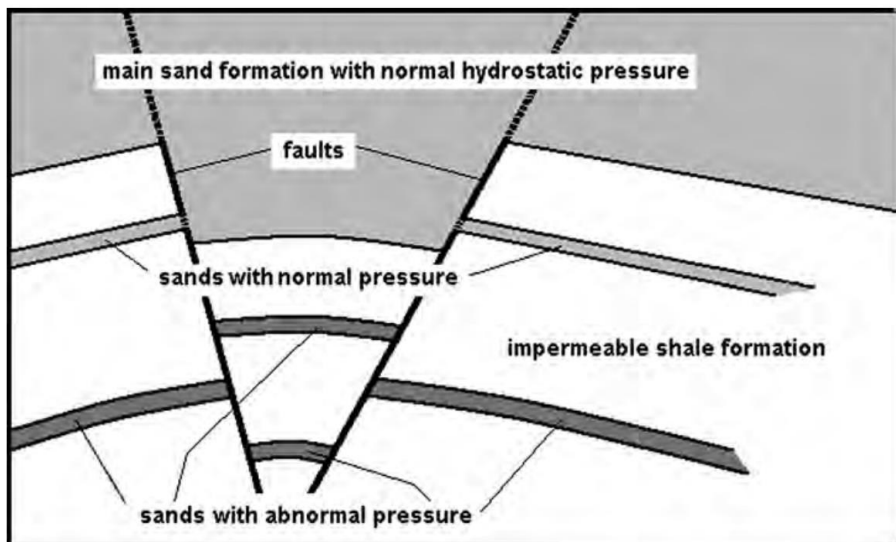


Figure 2.13. Schematic illustration for a cross-section of a geopressed system (DiPippo, 2008).

2.2.2.3 Magma Energy

In this type, the thermal energy of magma is extracted by drilling an injection well into magma, through the solidified cold lava, and injecting cold fluid at great pressure as shown in Figure 2.14. The injected cold fluid would solidify the molten magma into a glassy substance. Due to the thermal stress imposed on the glassy solidified magma, it should crack creating channels for the injected cold fluid to flow upwards back to the surface, harvesting the thermal energy of magma on its way to surface (DiPippo, 2008; Ghosh & Prelas, 2011).

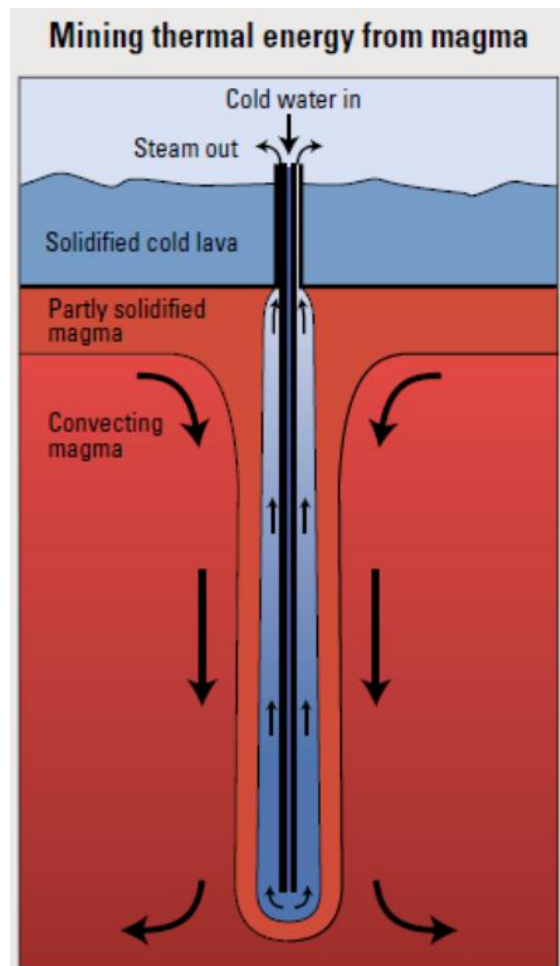


Figure 2.14. Schematic illustration for extracting the thermal energy contained in magma (Aydemir, 2021).

2.3 Utilization of Geothermal Systems

The thermal energy, carried by the geothermal fluid from the reservoir to the surface through production wells, can be utilized directly or converted to electricity using one of the available energy conversion systems, depending on the temperature of the geothermal fluid.

Lindal (1973) diagram is one of the most common diagrams which relates the suitable application based on the geothermal fluid temperature as shown in the left portion of Figure 2.15. As more applications of geothermal energy were found, the original Lindal diagram has been modified by many researchers, such as Haklidir & Haklidir (2020), shown on the right of the same figure.

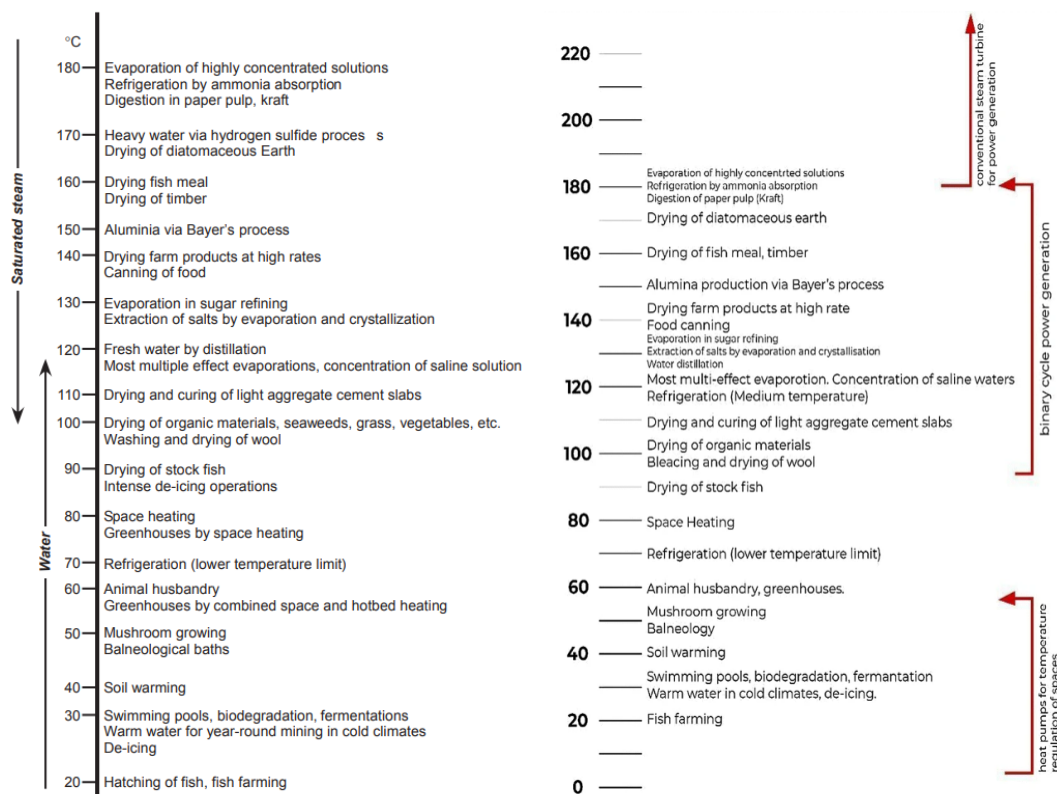


Figure 2.15. Lindal diagram relates the suitable application based on geothermal fluid temperature. Original diagram is on the left (Lindal, 1973), and a modified one by Haklidir & Haklidir (2020) is on the right.

2.3.1 Power Generation

The thermal energy of geothermal resources can be converted into electrical energy using steam power plant, flash power plant (single or double), or binary power plant depending on the geothermal fluid conditions.

The adopted hydrothermal resource classification of Sanyal (2005) takes power plant development into perspective as shown in Table 2.3, where appropriate power plant for every class is listed.

Table 2.3. Applicable power conversion system (power plant) for each hydrothermal resource class of Sanyal (2005).

Resource class	Mobile phase in reservoir	Reservoir temperature (°C)	Applicable power conversion system
1. Non-electrical grade	Liquid water	< 100	Direct use
2. Very low temperature		100 - 150	Binary
3. Low temperature		150 - 190	Binary; Double-flash; Hybrid
4. Moderate temperature		190 - 230	Single-flash; Double-flash; Hybrid
5. High temperature	Liquid water; Liquid-dominated two phase	230 – 300	Single-flash; Hybrid
6. Ultra-high temperature	Liquid-dominated two phase	> 300	Single-flash
7. Steam Field	Steam	240 °C (33.5 bar-a pressure; 2800 kJ/kg enthalpy)	Steam

2.3.1.1 Steam Power Plant

A simplified schematic diagram of the energy conversion system used in steam power plant is shown in Figure 2.16. The steam reaches the surface through the Production Well (PW), passing through the Wellhead Valve (WV), reaching to the

Particulate Remover (PR), which removes the particulate contained in the steam. The steam then reaches the Moisture Remover (MR), where any moisture that have formed through the Steam Pipe (SP) is removed. The PR and MR are very important equipment's used to protect the turbine blades from erosion that can be caused by the particulate and the moisture. After passing through the Control and Stop Valves (CSV), the steam is then directed into the powerhouse, which contains the Turbine (T) coupled with the Generator (G). The Steam is condensed using the cold water that cycles through the Condenser (C). Afterwards, the steam condensate is pumped, using Condensate Pump (CP), to the Cooling Tower (CT), where heat is rejected to the atmosphere by the moving air stream. A portion of the cooled condensate is pumped back to the condenser using the Cold Water Pump (CWP) while the other portion is injected back into the reservoir (DiPippo, 2008).

Steam ejectors with after condensers (SE/C) or/and vacuum pumps are used to extract the NCG's as they increase the overall pressure in the condenser and lower the turbine power output, if not removed (Barbier, 2002; DiPippo, 2008).

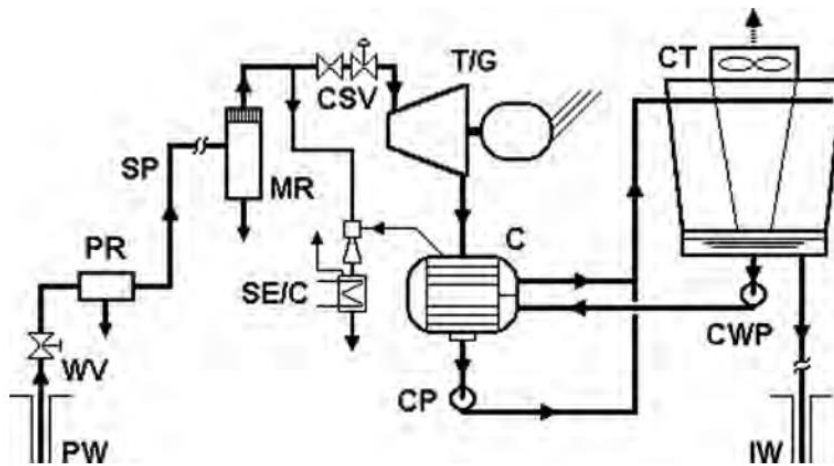


Figure 2.16. Simplified Schematic diagram of a steam power plant (DiPippo, 1998).

2.3.1.2 Flash Power Plant

Flash power plants are similar to steam power plant, however, the geothermal fluid undergoes a flashing process. Flashing is the phase change of geothermal fluid due to pressure dropping to the corresponding saturation pressure at a given temperature. A Silencer (S) is used to: abate the noise caused by the steam movement, facilitate flow rate measurement, and to divert the fluid flow when the powerhouse is under maintenance. The cyclone separators (CS), which use centrifugal forces to separate the liquid and steam, are used for flashing the geothermal fluid. If the CS in Figure 2.17 is replaced with a particulate remover (PR), it will be similar to a steam power plant (Figure 2.16). The separated liquid from the cyclone separator (CS) is directed towards the injection well (IW) through the Water or brine Pipes (WP) (DiPippo, 2008). Ball Check Valve (BCV) are used to stop any back pressure.

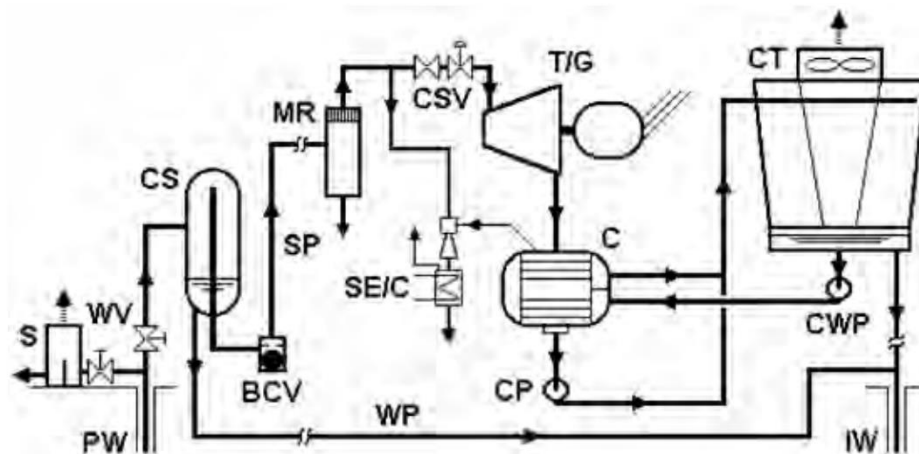


Figure 2.17. Simplified Schematic diagram of a single-flash power plant (DiPippo, 1998).

Because its energy conversion system contains one cyclone separator (CS) that undergoes the flashing process, it is called a single-flash power plant. If an additional flashing process is added to the single-flash power plant, making it a double-flash power plant.

The energy conversion system of a double-flash power plant does not differ much from the single-flash energy conversion system. Figure 2.18 shows the diagram of a double flash power plant. If compared with Figure 2.17, a flasher (F) is added to the system and the turbine is of a dual-admission type. The Separated water or brine from the cyclone separator (CS) is directed toward a flasher, where the second flashing process occurs, after it passes through a Throttle Valve (TV). The steam that emerges from the flasher has lower pressure relative to the steam that emerges from the cyclone separator (CS). Thereby, two steam pipes (SP) exist, the low-pressure steam is admitted into the turbine at a specific stage, where the high-pressure steam has partially expanded, to merge smoothly. The brine that emerges from the flasher (F), is directed to the injection well (IW) (DiPippo, 2008).

The power output would increase by 15-25% for the same geothermal fluid conditions. However, double-flash power plants are more costly, more complex, and require more maintenance (DiPippo, 2008).

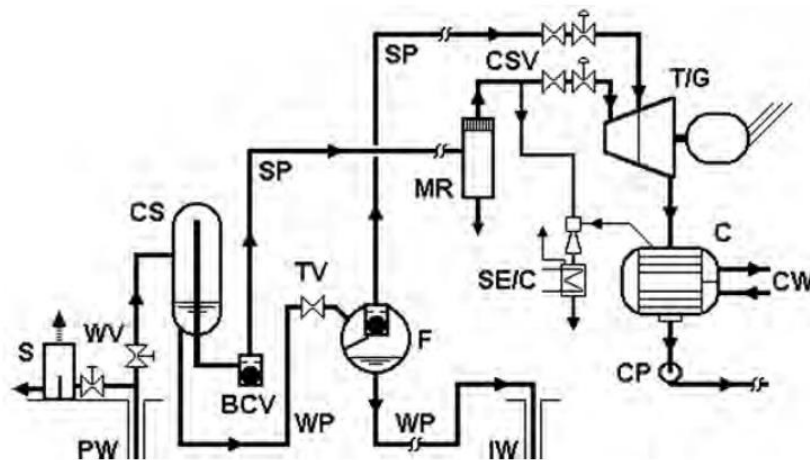


Figure 2.18. Simplified Schematic diagram of a double-flash power plant (DiPippo, 1998).

2.3.1.3 Binary Power Plant

Binary power plants can be utilized for very low and low temperature (100 – 190 °C) hydrothermal resources (Sanyal, 2005). The geothermal fluid heat is transferred into another fluid that has a much lower boiling point relative to water. Hence, the naming “binary” as it uses two fluids, the geothermal fluid and a working fluid (Dincer & Ozcan, 2018). Binary power plant:

- delivers sustainably zero-emissions energy as shown in Figure 2.19 (Bronicki & Lax, 2004; Glassley, 2010),
- prevents scaling problems (Dickson & Fanelli, 2003; DiPippo, 2008), and
- is very cost-effective (Dickson & Fanelli, 2003).

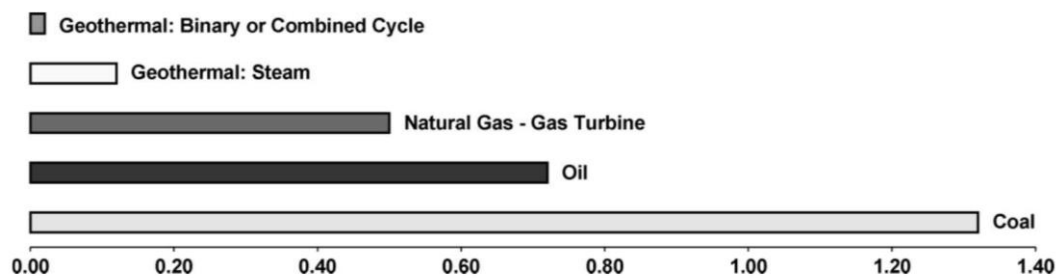


Figure 2.19. kgCO₂/kWh for various energy resources (Bronicki & Lax, 2004).

The energy conversion system of a binary power plant, which is operated by a conventional Rankine cycle (Dickson & Fanelli, 2003), is shown in Figure 2.20. The geothermal fluid is produced in its pressurized liquid state using a downhole pump (P), which is placed below the flash depth (or flash horizon depth) determined by the reservoir properties and the desired flow rate. Sand is removed from the geothermal fluid by the Sand Remover (SR), not to cause any erosion in the piping and heat exchanger tubes. Then, the geothermal fluid heat is transferred to the working fluid using a heat exchanger, which is composed of a Pre-Heater (PH) and an Evaporator (E). The PH brings the working fluid to its boiling temperature. The working fluid vaporizes in the evaporator (E) emerging as a saturated vapor. The vapor is then condensed back to its liquid phase after it passes through the powerhouse. The

working fluid repeats the same closed cycle again. While the geothermal fluid is injected back to the reservoir through the Injection Pump (IP). The geothermal fluid passes through a Final Filter (FF) before it goes through the injection well (IW). Makeup water (M) is needed for the condenser as the geothermal fluid does not feed the condenser cycle as in the steam and flash power plants (DiPippo, 2008).

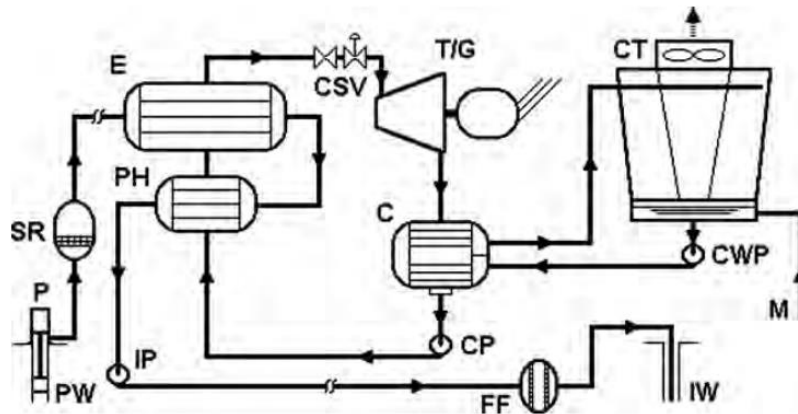


Figure 2.20. Simplified Schematic diagram of a binary power plant (DiPippo, 1998)

2.3.1.3.1 Scaling Issues

Calcite scaling occurs due to the breakout of steam and NCGs when the geothermal fluid flashes. Binary power plant solves this issue by maintaining (Dickson & Fanelli, 2003; DiPippo, 2008):

- geothermal fluid pressure higher than its saturation pressure corresponding to its temperature.
- geothermal fluid temperature higher than at which silica scaling could become an issue in the preheater (PH), piping, and injection well (IW).

2.3.1.3.2 Working Fluid

The working fluid has a great impact on the performance of the power plant, that is why it should be selected wisely as there are many options for working fluids. There are two main constraints that limit this selection, the thermodynamic properties of the working fluid, and its environmental, health, and safety properties (DiPippo, 2008). In general, hydrocarbons are preferred as the working fluid. Isopentane is used, mostly, in the U.S. (Ghosh & Prelas, 2011). In the Kalina binary-fluid cycle, a mixture of water and ammonia is used as the working fluid (Dickson & Fanelli, 2003). CO₂ could also be utilized as a working fluid, specially that it is a greenhouse gas, non-flammable, non-toxic, and has a low cost (Maghiar & Antal, 2001). Maghiar & Antal (2001) discussed the motivating results of a binary power plant that utilizes CO₂ as the working fluid in Romania.

2.3.1.3.3 Functional Correlations for Power Plant Efficiency and Operations

Zarrouk & Moon (2014) established a correlation between the efficiency of the binary power plant η_{act} (%) and the inlet enthalpy of the geothermal fluid h_{in} , Eq. 2.1, using the published data of 31 binary power plants.

$$\eta_{act}(\%) = 6.6869 \ln(h_{in}) - 37.929 \quad 2.1$$

Tester et al. (2006), established an equation that correlates the geothermal fluid outlet temperature T_{out} with its inlet temperature T_{in} , Eq. 2.2.

$$T_{out} = T_{in} + \frac{W/\dot{m}_p}{0.098701 - 0.0039645T_{in}} \quad 2.2$$

Where W is the running capacity of the binary power plant, and \dot{m}_p is the mass production rate.

2.3.2 Direct Use

As the name suggests, the thermal energy of the geothermal fluid is utilized directly rather than converting it to electricity. District heating, one of the direct use applications, is widely used in Reykjavik, Iceland, where 99% of the buildings are heated using the thermal energy of geothermal resources directly (Zarrouk & McLean, 2019). The accepted minimum practicable temperature for heating use is generally 55 °C (Dickson & Fanelli, 2003).

Depending on the chemical composition of the geothermal fluid, geothermal district heating systems are of two types, open loop and closed loop (Dickson & Fanelli, 2003). The closed loop systems are similar to binary systems in terms of transferring the geothermal fluid heat to a secondary fluid using heat exchangers as shown in the bottom portion of Figure 2.21. A high conversion efficiency of 80% to 90% is possible (Zarrouk & McLean, 2019). While, in the open loop systems, the geothermal fluid heat is utilized without transferring it to a secondary fluid as shown in top portion of Figure 2.21. The purity of geothermal fluid in Iceland is high enough, allowing the implementation of open loop district heat systems (Dickson & Fanelli, 2003).

In both types, a fossil-fueled boiler is installed to handle the usually very short peak heat demand periods. Radiators are the water-to-air heat exchangers, which are used to heat the air at the user end (Dickson & Fanelli, 2003).

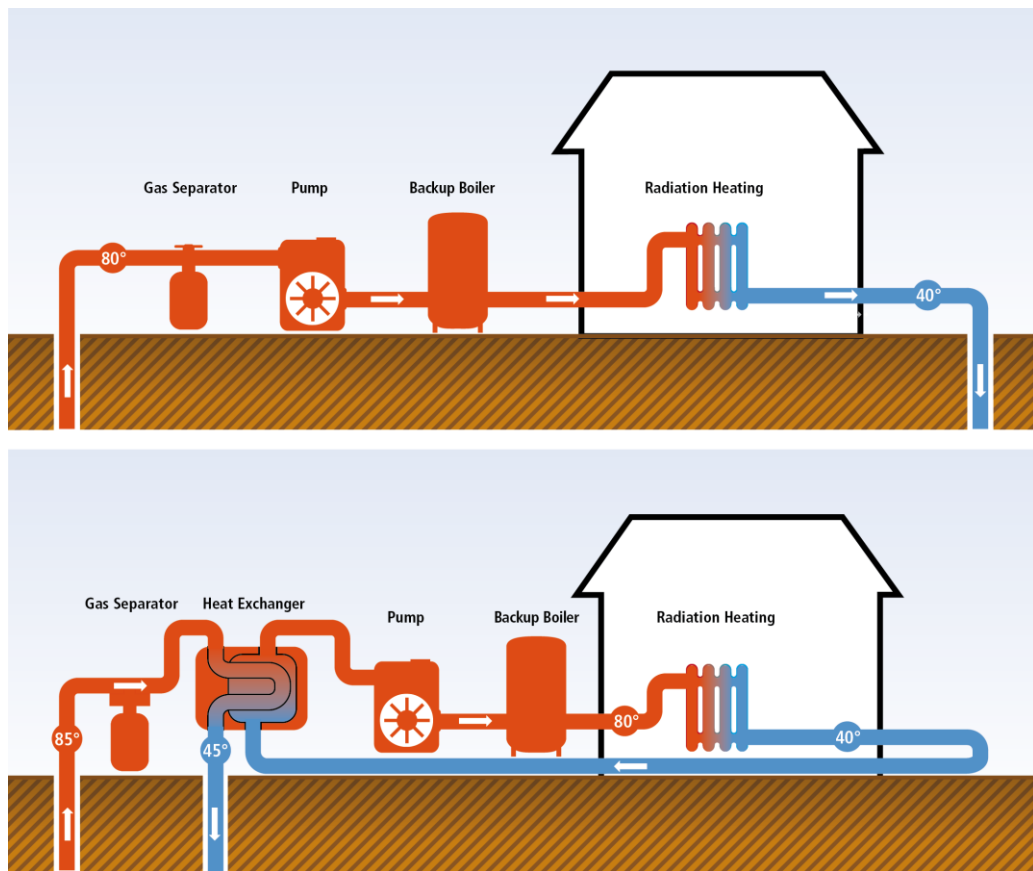


Figure 2.21. Geothermal district heating systems are of two types, open loop type (top), and closed loop type (bottom) (Edenhofer et al., 2011).

CHAPTER 3

GEOTHERMAL RESERVOIR MODELS

There are three methods for modeling the behavior of geothermal reservoirs; Decline Curve Analysis (DCA), Reservoir Simulators (often called Distributed-Parameter Models DPM³, Axelsson. 2016), and Lumped-Parameter models (LPM) (Bodvarsson et al., 1986; Sarak et al., 2005). All of these methods require historical data of the field to be available (Sanyal & Sarmiento, 2005), and they vary in cost and complexity (Bodvarsson et al., 1986).

DCA is based on fitting algebraic equations to the historic production flow rates to predict future production flow rates (Bodvarsson et al., 1986). While, Both DPMs and LPMs are a quantification of a conceptual model. The conceptual model is the first and most crucial step in the modeling process (Grant, 1983). All the important physical processes that; take place around or within the reservoir, affect the geothermal system. Therefore, such physical processes should be adequately defined in the conceptual model (Grant, 1983; Bodvarsson et al., 1986). The quantitative models are validated by testing its ability to produce a known behavior such as the pressure or temperature histories. These models are calibrated or the conceptual model itself is modified to produce a match (Grant, 1983). After history-matching, the quantitative model can be used to forecast various scenarios (Grant, 1983), and to answer important reservoir management questions (Bodvarsson et al., 1986). Thus, guiding reservoir management.

³ Distributed Parameter Models (DPM) are used interchangeably with numerical models as in e.g.: Grant (1983), Bodvarsson et al. (1986), Nurlaela (2016), and Qin et al. (2017).

In the following, first DCA is discussed, followed by DPM and LPM, respectively. Special emphasis is given to LPM since it is included in the scope of this study.

3.1 Decline Curve Analysis

Production of geothermal fluids declines with time naturally, same as production of oil and gas. DCA in geothermal industry have been adopted from the petroleum industry (Hidayat, 2016). In this empirical method, the decline of historic production rates through time is fitted with algebraic equations, which are then used to predict future production rates (Bodvarsson et al., 1986; Sanyal & Sarmiento, 2005; Taji & Alp, 2021). The general equation, Eq. 3.1 (Ripperda & Bodvarsson, 1987), stems from the assumption that decline rate D_r is proportional to the production rate q raised to the decline exponent b .

$$\left(\frac{1}{q}\right) \frac{dq}{dt} = -D_r q^b \quad 3.1$$

The decline exponent b ranges from 0 to 1 for the hyperbolic equation, Eq. 3.2 (Ripperda & Bodvarsson, 1987), but in special cases it can be greater than 1 (Gentry & McCray, 1978). The special cases of $b = 0$ and $b = 1$ yield the exponential and the harmonic equations, Eq. 3.3 and Eq. 3.4 (Ripperda & Bodvarsson, 1987), respectively. q_i is the initial production rate or $q(t = 0)$.

$$q(t) = \frac{q_i}{(1 + bD_r t)^{\frac{1}{b}}} \quad 3.2$$

$$q(t) = q_i e^{-D_r t} \quad 3.3$$

$$q(t) = \frac{q_i}{(1 + D_r t)} \quad 3.4$$

Figure 3.1 shows the historical production rate plotted against time, where Eq. 3.2, Eq. 3.3, and Eq. 3.4 are fitted to the historical production rate. For this example, it has been determined that it exhibits a hyperbolic decline with $b = 0.8$ (Ripperda & Bodvarsson, 1987). According to this, future production rates are forecasted.

However, one great limitation of the DCA is that operating conditions and particularly production/injection strategy, must remain constant for the extrapolations to be valid (Bodvarsson et al., 1986; Ripperda & Bodvarsson, 1987; Sanyal & Sarmiento, 2005). Furthermore, DCA is restricted to the prediction of future production rates only (e.g., cannot predict reservoir pressure and temperature behavior).

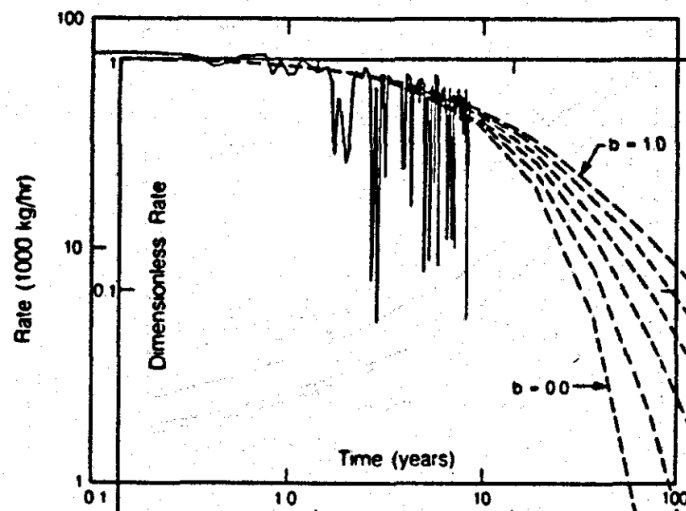


Figure 3.1. Production rate vs time fitted by the exponential, hyperbolic, and harmonic decline equations (Ripperda & Bodvarsson, 1987).

3.2 Reservoir Simulators or Distributed-Parameter Model

Distributed-parameter model or reservoir simulator is a computer code that takes into account multiple physical and chemical phenomena. Different types of input about the geothermal reservoir are provided by the user such as the geology (rock types, faults, surface topology etc.), well data (depths, temperature and pressure profiles, productivity curve, etc.), geochemistry (flow rates, temperatures, etc.), geophysics, and hydrology (DiPippo, 2008; Axelsson, 1989). The mathematical model containing Partial Differential Equations (PDEs) is solved using finite difference or finite element techniques. TOUGH, TOUGH2, STAR, MULKOM are examples of geothermal reservoir simulators (DiPippo, 2008). TOUGH2 (Pruess et al., 1999), is

one of the widely used geothermal simulators. PETRASIM software is the user interface for TOUGH2 code.

Antúnez et al. (1995), Boardman et al. (1996), Biagi et al. (2015), Pradhipta et al. (2019), and Yuono & Daud (2020), are examples of simulation studies that used TOUGH2. Yeltekin et al. (2002), Akin et al. (2010), Pathak et al. (2014), Chong et al. (2021), and Zhang et al. (2021) are examples of simulation studies that used STARS.

In reservoir simulation, a conceptual model representing the geothermal reservoir or field of interest is built using a number of discrete gridblocks, or tanks (Figure 3.2), where equations such as the energy and mass balances are solved for each block. The general form of the governing equations is written as, Eq. 3.5 (Pruess et al., 1999).

$$\frac{d}{dt} \int_{V_n} M^{(K)} dV_n = \int_{\tau_n} \vec{F}^{(K)} \cdot \vec{n} d\tau_n + \int_{V_n} q_v^{(K)} dV_n \quad 3.5$$

Where M represents the accumulation term within the gridblock or volume of the domain V_n . The change of M with time is a result of; the flow F across the boundary surface τ_n of the cell V_n , and sinks or sources volumetric rates q_v . K represents the component, which can be water, non-condensable gas, heat, and others. For example, for the heat balance ($K = \text{heat component}$), M (J/m³) is the amount of heat per unit volume in the domain volume V_n (m³), F (J m⁻² s⁻¹) is the heat flux through the boundary surface τ_n (m²) of the block, and q_v (J m⁻³ s⁻¹) is the heat source or sink. For the mass balance (water) ($K = \text{mass component}$), M (kg/m³) is the water mass per unit volume, F (kg m⁻² s⁻¹) is the mass flux (Darcy flow), and q_v (kg m⁻³ s⁻¹) is for the mass source/sink (injection/production wells) (Bodvarsson et al., 1986; Pruess et al., 1999).

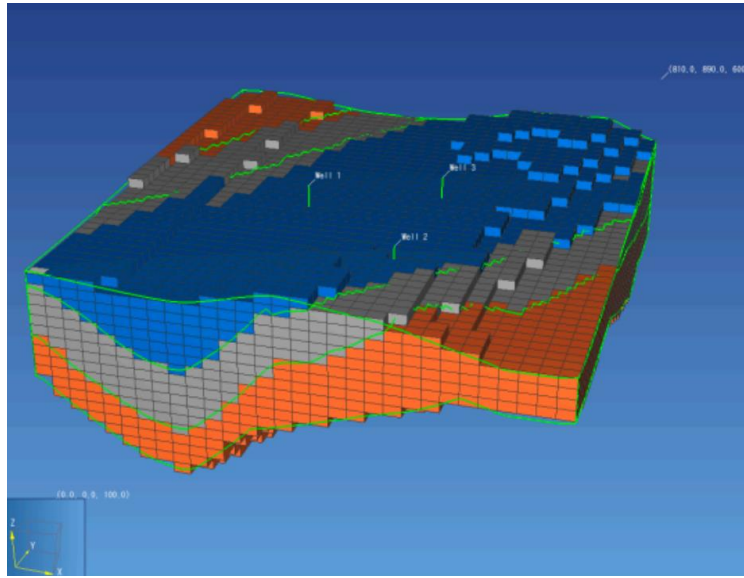


Figure 3.2. Example of a conceptual model built using a number of cells or tanks (Alcott et al., 2012).

DPMs offer many features to the user. They are able to; model the spatial differences in rock and thermodynamic properties, model the different rock layers of the geothermal system, cap rock, bed rock, the reservoir, model the multiphase and multicomponent flow within the system, and the modeling accuracy is controlled by the user through increasing the number of blocks (Bodvarsson et al., 1986; Sanyal & Sarmiento, 2005; Tureyen et al., 2009).

3.3 Lumped-Parameter Models

LPMs are in fact DPMs but with coarse or no spatial discretization. In this method, the reservoir is represented by one (Figure 3.3, Case a) or few blocks (Figure 3.3, Case b & c), where conservation of energy and mass is applied (V_n is equal to one or very few domains in Eq. 3.5) (Bodvarsson et al., 1986). Average properties are assigned to the geothermal system parts (Sarak et al., 2005). The governing equations, however, are reduced to Ordinary Differential Equations (ODE) that are solved semi-analytically (Bodvarsson et al., 1986). LPM offer a great alternative to DPM in case of limited funds, time, and field data (Axelsson, 1989). As the

formulation of the mass and energy ODE's are dependent on the fluid phase in the reservoir, the initial fluid state must be specified (Grant, 1983). The following discussion of LPM is restricted to single-tank LPM representing single-liquid phase geothermal reservoir since it is the scope of this study.

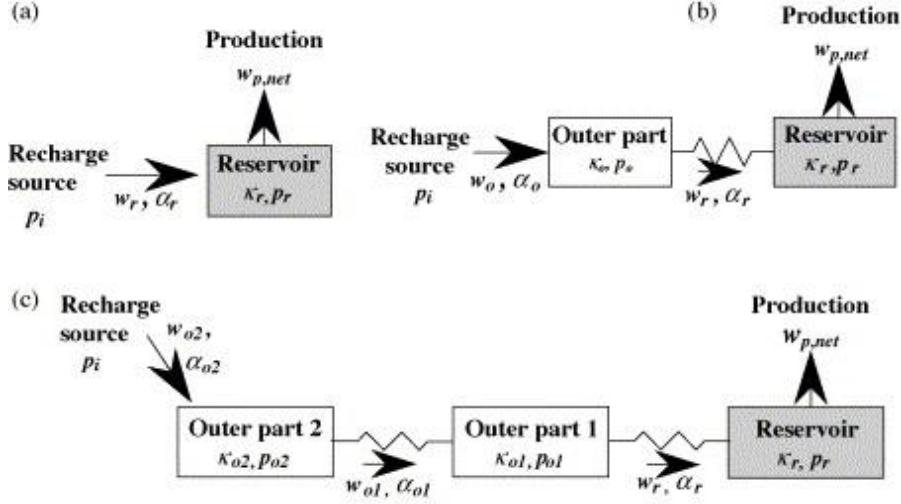


Figure 3.3. Three various lumped-parameter models where; case (a) is a single-tank LPM, Case (b) is a two-tank LPM, Case (c) is a three-tank LPM (Sarak et al., 2005).

3.3.1 Motivation for Lumped-Parameter Models

The motivation behind using LPM stems mainly from the fact that DPMs need extensive data and long development time, which both are not available in the early life of the reservoir. Reservoir development is constrained to the development of the power plant. If power plant construction is not committed, the reservoir will be abandoned. To commit to the construction of the power plant, reservoir performance should be forecasted 20 to 30 years (lifetime of a power plant). At the early stage of reservoir development, available data is insufficient for the development of DPM (Castanier et al., 1980). DPMs also require; an experienced modeler, higher computational power (Bodvarsson et al., 1986), more time to develop (several times

the 1 year a lumped-parameter model roughly consumes to develop, Grant, 1983), extensive amount of data, long run-times (Tureyen et al., 2009), and higher cost relative to LPM (Axelsson, 1989).

3.3.2 Single-Tank Lumped-Parameter Models

The explanation here is restricted to one-tank LPM representing geothermal reservoir, since it is used in the scope of this study. The same logic, however, applies for the multi-tank LPM whether it is of two-tank, three-tank, etc. Single-tank LPM is shown in Figure 3.4, where the reservoir receives energy and mass from recharge and injection, and losses energy and mass from production. Whilst the reservoir is gaining and losing energy through conduction. The reservoir (or control volume) of volume V_R contains rock of porosity ϕ_r and water of density ρ_w . Reservoir temperature T_r and reservoir pressure P_r are being affected by the water production at \dot{m}_p rate, injection of water at temperature T_{ri} and \dot{m}_{ri} rate, and the production induced recharge at temperature T_{re} and \dot{m}_{re} rate.

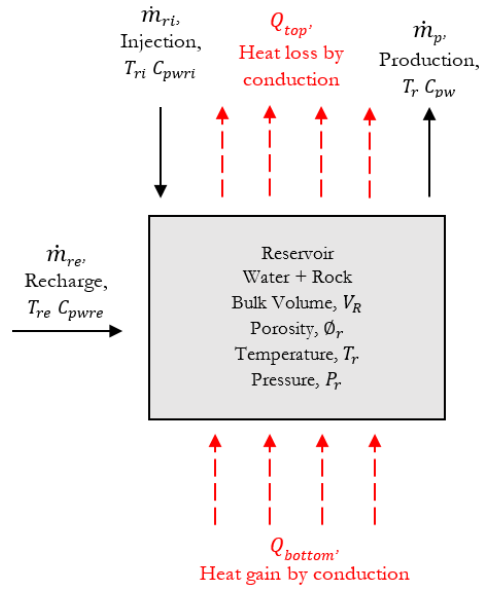


Figure 3.4. One tank, cell, or control volume lumped-parameter model for hot water hydrothermal systems.

The governing equations for the single-tank LPM shown in Figure 3.4, are the mass and energy balances. The mass balance ODE in the form of Eq. 3.5 (Pruess et al., 1999) is Eq. 3.6 (Onur et al., 2008).

$$V_R \frac{d(\rho_w \phi_r)}{dt} = \dot{m}_{re} - \dot{m}_p + \dot{m}_{ri} \quad 3.6$$

The accumulation term M , the Left-Hand Side (LHS) term, is mass of water in the reservoir. The water and rock are compressed due to the confinement of the reservoir. Once production commences, reservoir pressure decreases and thus, the pores and water expand (water density and rock porosity change throughout time). The Right-Hand Side (RHS) contains the mass flux (the recharge) across the reservoir boundary, and the mass source (injection well) and sink (production well), respectively.

Eq. 3.7 (Satman, 2010) is the Energy balance ODE in the form of Eq. 3.5 (Pruess et al., 1999).

$$V_R \rho_{av} C_{av} \frac{dT_r}{dt} = \dot{m}_{re} C_{pwre} T_{re} + Q_n - \dot{m}_p C_{pw} T_r + \dot{m}_{ri} C_{pwi} T_{ri} \quad 3.7$$

The LHS is the energy accumulation term, where $\rho_{av} C_{av}$ is the volumetric heat capacity of the reservoir, defined in Eq. 3.8 (Satman, 2010). The RHS is composed of four terms. The first two terms represent the energy flow across the reservoir boundary: the recharge having an isobaric heat capacity of C_{pwre} , and the net conductive heat flow Q_n . The other two terms represent: the heat sink (production) having an isobaric heat capacity of C_{pw} , and the heat source (injection) having an isobaric heat capacity of C_{pwi} .

$$\rho_{av} C_{av} = \phi_r \rho_w C_{pw} + (1 - \phi_r) \rho_m C_{pm} \quad 3.8$$

Where ρ_m is the matrix (rock) density, and C_{pm} is the isobaric heat capacity of the matrix.

In single-tank visualization of the reservoir, the reservoir is assumed to be in complete thermodynamic equilibrium (Whiting & Ramey Jr., 1969; Satman, 2010)

3.3.3 Literature Review

Whiting & Ramey Jr. (1969) discussed multiple various initial conditions for geothermal reservoirs and their behaviors under exploitation. The authors stated that geothermal reservoirs whose initial conditions are within the vapor region of water (vapor-dominated reservoirs) follow an isothermal path during exploitation, as well as geothermal reservoirs whose initial conditions are within the compressed liquid state of water (liquid-dominated reservoirs). Energy and material balances were applied to single-tank reservoir that contains steam, water, and rock. For reservoir containing compressed liquid only, the implicit energy and mass balances equation is reduced to the mass balance equation only. They applied their model to the Wairakei geothermal reservoir in New Zealand. Using a computer program, system constants, such as initial mass in the reservoir, aquifer size, influx constant, etc., were determined by matching the available pressure history using least-squares fitting techniques. The authors matched the pressure history successfully (excellent match between calculated and measured data) for the period of 1956 to 1961 as shown in Figure 3.5. The system constants they determined were, then, used to predict the performance until 1965, and forecast the reservoir performance under various annual production rates for the period of 1966 to 2000.

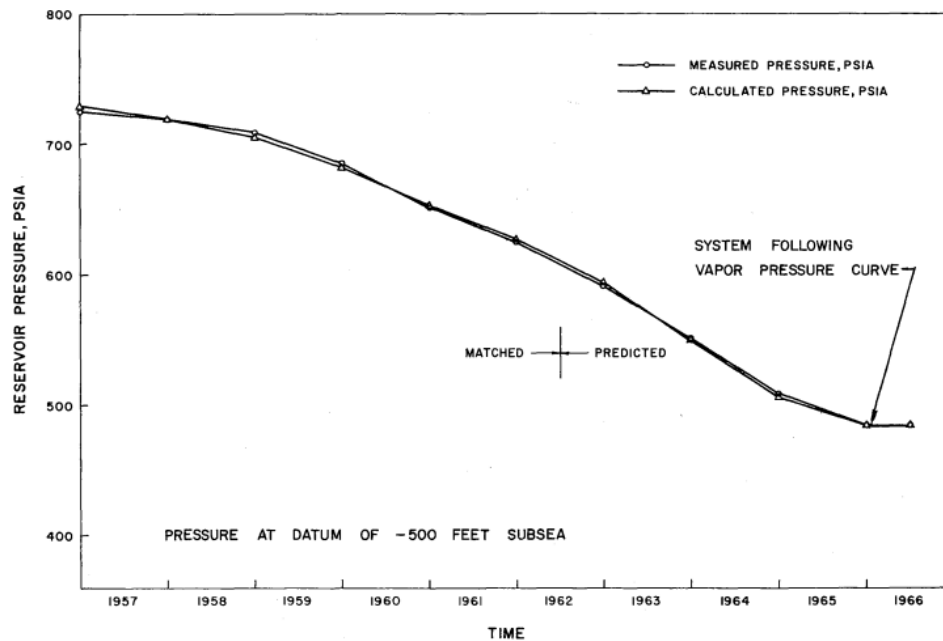


Figure 3.5. Reservoir pressure history of Wairakei geothermal reservoir from 1956 to 1961 matched by the model of Whiting & Ramey Jr. (1969). The model was used to predict and forecast the future performance of the reservoir Whiting & Ramey Jr. (1969).

Castanier et al. (1980) developed an analytical implicit model for simulating geothermal reservoir that contains liquid and steam, liquid only, and steam only. The authors divided the reservoir into three distinct radial zones (two-tanks) as shown in Figure 3.6; (1) the central zone: production occurs and injection is possible in this tank or zone, which is modeled by a LPM similar to that developed by Whiting & Ramey Jr. (1969), (2) intermediate zone: models only the mass and heat transfer from the outer zone into the central zone, and (3) an outer zone: where injection or the induced recharge occurs. If the width of the intermediate zone is equal to zero, the model reduces to single-tank LPM. The reservoir representation or division has allowed to capture the fluid flow and heat transfer more realistically relative to single-tank LPM (considering the whole reservoir as the central zone only). The authors tested their model by comparing its results against a simulation study of East Mesa hot water geothermal reservoir, which used a numerical complex three-

dimensional multi-layer simulator. Their model results were in good agreement with the simulation study results. The authors, then, conducted sensitivity analysis and studied multiple development scenarios.

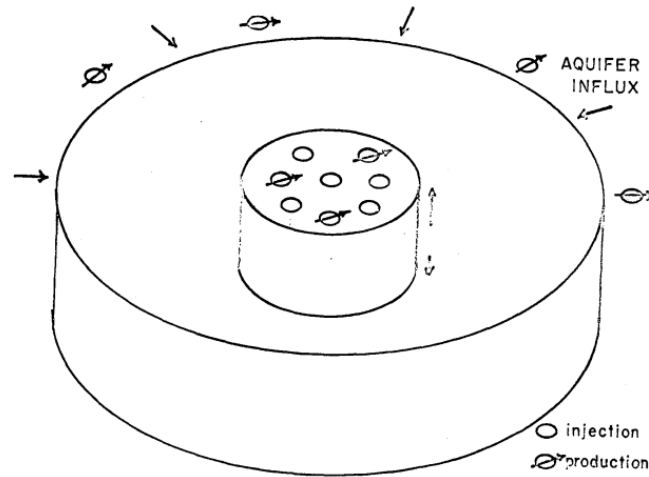


Figure 3.6. Reservoir representation of Castanier et al. (1980) analytical model divided into three distinctive radial zones; central, intermediate, and outer zone.

Gudmundsson & Olsen (1987) modeled Svartsengi geothermal field in Iceland using single-tank isothermal LPM that considers water only. Their model includes the mass balance only. The model matched reservoir drawdown history and forecasted the drawdown for several production rates.

Axelsson (1989) developed an implicit isothermal model in matrix-vector form for liquid-dominated geothermal reservoirs. The model tackles the simulation problem inversely as it automatically estimates the model constants by fitting the simulated results to the observed data. He applied conservation of mass only to a series of tanks (called capacitors in his work) that contain water. Pressure histories of four geothermal fields from Iceland were matched by three-tank (capacitor) LPM. The three tanks represent the reservoir's: innermost part, outer parts, and recharge part. Three of the four geothermal fields were only simulated using LPM due to limited data and/or research funds. While the other geothermal field, Laugarnes field, contained sufficient data allowing DPMs simulation to be conducted. His LPM model results achieved a great match with the pressure histories of the four

geothermal fields. Furthermore, Axelsson's model was able to match the pressure history of Laugarnes field to the same accuracy achieved by the DPM's but only with a fraction of the time needed to develop these DPMs. After pressure-history matching, the LPMs of the four geothermal fields were used to forecast reservoir pressure behavior under various scenarios. The author also developed a software program, LUMPFIT, that is based on his LPM model (Axelsson & Arason, 1992). Fajardo (2000), Weixing et al. (2003), Vallejos-Ruiz (2005), Syed (2011), and Bostanci (2018) are examples of studies that used LUMPFIT.

Alkan & Satman (1990) extended the work of Whiting & Ramey Jr. (1969) by including CO₂ component into Whiting & Ramey's model. They tested their extended model by matching the pressure history of three geothermal fields in Mexico, New Zealand, and Italy, where input data (system constants) were acquired from the literature. Their model calculated results matched the measured data excellently.

Sarak et al. (2005) developed explicit analytical expressions for the pressure drawdown of geothermal reservoir containing water, which work only under exploitation scenario. The authors' isothermal model is similar to that of Gudmundsson & Olsen (1987) and Axelsson (1989) discussed previously. The authors applied mass balance to a single-tank, two-tank, and three-tank representation of various parts of the reservoir as shown previously in Figure 3.3. The authors used the steady state Schilthuis (1936) water influx method to describe the recharge rate, Eq. 3.9.

$$\dot{m}_{re} = \alpha (P_{ri} - P_r(t)) = \alpha \Delta P_r \quad 3.9$$

Where α is the recharge index or constant, ΔP_r is the reservoir pressure drawdown.

For single-tank LPM, the reservoir pressure drawdown due to exploitation is modeled using Eq. 3.10.

$$\Delta P_r(t) = P_{ri} - P_r(t) = \frac{\dot{m}_{pn}}{\alpha} (1 - e^{-\frac{\alpha}{\kappa} t}) \quad 3.10$$

Where \dot{m}_{pn} is the net production rate defined in Eq. 3.11, κ is the storage capacity defined in Eq. 3.12.

$$\dot{m}_{pn} = \dot{m}_p - \dot{m}_{ri} \quad 3.11$$

$$\kappa = V_R \rho_w \phi_i c_t \quad 3.12$$

Where ϕ_i is the initial porosity, and c_t is the total (fluid + formation) isothermal compressibility ($c_t = c_f + c_r$), which is assumed constant, of the reservoir system as the fluid and rock are assumed to be slightly compressible.

As Eq. 3.10 is limited to a constant net production rate throughout the production period, the authors applied Duhamel's principle (i.e., the superposition method) to model variable net production rates, Eq. 3.13.

$$\Delta P_r(t) = \sum_{j=1}^n \frac{\Delta \dot{m}_{pn}(t_j)}{\alpha} (1 - e^{-\frac{\alpha}{\kappa} (t-t_{j-1})}) \quad 3.13$$

Where $\Delta \dot{m}_{pn}(t_{j+1})$ is the net production flow rate steps defined in Eq. 3.14.

$$\Delta \dot{m}_{pn}(t_j) = \dot{m}_{pn}(t_j) - \dot{m}_{pn}(t_{j-1}) \quad 3.14$$

Where j is the time index. The authors assumed that $t_0 = 0$, and $\dot{m}_{pn}(t_0) = 0$.

The authors tested their models using the pressure histories of two geothermal fields, Laugarnes geothermal field in Iceland, and Balcova-Narlidere Geothermal field in Turkey. Their model results were similar to Axelsson (1989) in matching the pressure history of Laugarnes geothermal field. Their model also matched the pressure history of the other geothermal field, and its constants were used to predict its behavior under different scenarios. Satman et al. (2005) is an example of a simulation study, conducted using Sarak et al.'s model, of the Kizildere geothermal field in Turkey.

Onur et al. (2008) argued that reservoir temperature must also be modeled for geothermal reservoir containing water only. They stated that reservoir temperature can change substantially when there are injection operations and when recharge is at temperature different than the reservoir. Even for a closed system, where there is no recharge, no injection, and only production, its temperature would slightly decrease due to the decrease in the system internal energy, which results from the pressure decline due to the mass removal through production, according to Onur et al. (2008). The authors applied mass and energy balances to one-tank representation of a reservoir that contains water (liquid phase) only and solved implicit equations numerically. They verified their implicit model against numerical simulator TOUGH2, and achieved a great match. The authors, then, used their model in a sensitivity study for the Balcova-Narlıdere geothermal field (Turkey), where reservoir pressure and temperature behavior is investigated for varying values of constants such as the recharge constant α , recharge temperature T_{re} , reservoir volume V_R , initial rock porosity ϕ_i , and rock compressibility c_r .

Tureyen et al. (2009) extended the work of Onur et al. (2008) to include multiple tanks. Their implicit model was solved semi-numerically. The authors used their model to match a synthetic reservoir pressure and temperature history, emphasizing that temperature history matching along with pressure history matching allows better estimation of system constants.

Satman (2010) developed an explicit analytical one-tank LPM for geothermal reservoirs containing water. His model simulates the behavior of the geothermal reservoir, in terms of reservoir pressure and temperature, when under exploitation (production) and shut-in (no production or injection). Satman used the Sarak et al. (2005)'s model for the simulation of reservoir pressure behavior, Eq. 3.10, and derived the following expression, Eq. 3.15, for simulating the reservoir temperature behavior T_r for a geothermal reservoir under exploitation,

$$T_r = T_{r_i} e^{-at} + \frac{b'}{a} \left(1 + \frac{D}{a-D} e^{-at} - \frac{a}{a-D} e^{-Dt} \right) + \left(\frac{g}{a} + \frac{x}{a} \right) (1 - e^{-at}) \quad 3.15$$

where T_{r_i} is the initial reservoir temperature, a , b' , D , g , and x are constants defined in Eq. 3.16, Eq. 3.17, Eq. 3.18, Eq. 3.19, and Eq. 3.20, respectively.

$$a = \frac{\dot{m}_p C_{pw}}{V_R \rho_{av} C_{av}} \quad 3.16$$

$$b' = \frac{\dot{m}_{pn} C_{pwre} T_{re}}{V_R \rho_{av} C_{av}} \quad 3.17$$

$$D = \frac{\alpha}{\kappa} \quad 3.18$$

$$g = \frac{\dot{m}_{ri} C_{pwi} T_{ri}}{V_R \rho_{av} C_{av}} \quad 3.19$$

$$x = \frac{Q_n}{V_r \rho_{av} C_{av}} \quad 3.20$$

When the reservoir is under shut-in, its pressure is modeled using Eq. 3.21, and its temperature is modeled using Eq. 3.22, or Eq. 3.23, depending on reservoir temperature at the end of the production period T_{rp} . If $T_{re} > T_{rp}$, Eq. 3.22 is used, while Eq. 3.23 is used if $T_{re} < T_{rp}$.

$$\Delta P_r(\Delta t_p) = P_{r_i} - P_r(\Delta t_p) = \frac{\dot{m}_{pn}}{\alpha} e^{-D\Delta t_p} (1 - e^{-Dt_p}) \quad 3.21$$

$$T_r(\Delta t_p) = T_{rp} + x\Delta t_p + \frac{C_{pwre} T_{re} \dot{m}_{pn}}{V_R \rho_{av} C_{av} D} (1 + e^{-Dt} - e^{-D\Delta t_p} - e^{-Dt_p}) \quad 3.22$$

$$T_r(\Delta t_p) = T_{rp} + x\Delta t_p - \frac{C_{pwre} (T_{rp} - T_{re}) \dot{m}_{pn}}{V_R \rho_{av} C_{av} D} (1 + e^{-Dt} - e^{-D\Delta t_p} - e^{-Dt_p}) \quad 3.23$$

where T_{rp} is the reservoir temperature at the end of the production period t_p . Δt_p is the difference between time t and the end of production period time t_p ($\Delta t_p = t - t_p$).

The above expressions in Satman (2010) LPM model are limited to:

- Constant production and injection rates (constant net production rate), and constant injection temperature.
- Constant fluid properties for geothermal fluid, recharge, and injection. In other words, fluid densities and isobaric heat capacities are all constants.
- Constant net conductive heat flow.

The author used his model to study the effects of multiple system constants, such as reinjection rate, Recharge temperature, net conductive heat flow, etc., on reservoir temperature and pressure behaviors for a synthetic geothermal reservoir (sensitivity analysis). The author, then, used the model to estimate system constants (e.g., reservoir volume, recharge temperature, net conductive heat flow, and the product of the porosity and total isothermal compressibility) of Wairakei geothermal field in New Zealand.

Tureyen & Akyapı (2011) extended the work of Onur et al. (2008), and Tureyen et al. (2009) by including the effects of heat conduction, Eq. 3.24.

$$Q = \gamma_{i,j_l}(T_{j_l} - T_i) \quad 3.24$$

Where Q is the conductive heat flow, γ_{i,j_l} is the conduction index between tanks i and j_l , whose temperatures are T_i and T_{j_l} , respectively.

Their implicit model is solved numerically, and it was verified against the numerical simulator TOUGH2. The authors, then, used their model to match a synthetic reservoir pressure and temperature history, emphasizing that temperature history matching along with pressure history matching allows better estimation of system constants.

Nurlaela (2016) developed a single-tank LPM for two phase (water and steam) geothermal reservoir based on Onur et al. (2008). His/Her implicit model couples energy and mass balances, which are solved numerically. The author verified his/her model against TOUGH2 code. Two different cases were verified: without recharge

($\alpha = 0$), and with recharge. The author's model results achieved a good match with the results of TOUGH2 for no recharge case. While it achieved a good conformity with the results of TOUGH2 for the recharge case. The author attributed the difference between the results of her/his model and TOUGH2 to the equation solving method since ODE constitute the developed LPM while PDE constitute the numerical simulator TOUGH2.

Qin et al. (2017) developed a multiple-tank LPM for geothermal reservoirs containing two-phase (steam and water) or superheated vapor. The implicit model is based on the mass and energy balances, which are numerically solved. The authors used their model of three-tanks to generate the pressure and temperature histories and match it.

Firanda et al. (2021) developed a single-tank LPM for two-phase (water and steam) or water only. The LPM is based on mass and heat balance. The authors, however, did not mention the solution technique for these equations. Their LPM was coupled with flow of water and steam through porous media for a radial reservoir using Pseudo-Steady State (PSS) Darcian flow, to calculate the bottomhole pressure. The Authors modeled the flow in the well using Bernoulli equation to determine the wellhead pressure, assuming fluid flow in the well is isothermal. They also calculated the power generation from a single-flash power plant using analytical calculations.

This study uses analytical, explicit, non-isothermal, single-tank LPM for water, and extends Satman (2010)'s LPM by its ability to model:

- Varying production and injection rates (varying net production rate), and varying injection temperature.
- Varying fluid properties for geothermal fluid, recharge, and injection. In other words, fluid densities and isobaric heat capacities are not constants.
- Varying net conductive heat flow modeled using Eq. 3.24 (Tureyen & Akyapı, 2011).

This LPM developed in this study is verified in 3 stages, and it is coupled with analytical expressions, which model:

- Geothermal fluid Steady State (SS) flow through porous media.
- Geothermal fluid non-isothermal flow in injection and production wellbores.
- Power generation from a binary power plant, using correlations.

Table 3.1 summarizes the important features of all the LPM models discussed in this section, and compares to the model developed in this study. Note that all mentioned LPM models are numerical implicit, but three LPM models are analytical explicit: Sarak et al. (2005), Satman (2010), and this study's model.

Table 3.1. Summary of the important features of all the LPM models discussed in the literature review, including this study.

Author	Number of tanks	Phases	Non-isothermal/Isothermal	Solution type	Explicit/Implicit	Reservoir to well flow	Wellbore flow	Power plant
Whiting & Ramey Jr. (1969)	Single-tank	water & steam or water only ²	Non-isothermal for two-phase, Isothermal for water ²	Analytical ³	Implicit *	No	No	No
Castanier et al. (1980)	Two-tank	Steam and/or water	Non-isothermal	Analytical	Implicit *	No	No	No
Gudmundsson & Olsen (1987)	Single-tank	Water	Isothermal	Not stated	Implicit *	No	No	No
Axelsson (1989)	Multiple-tank	Water	Isothermal	Numerical *	Implicit ⁵	No	No	No
Alkan & Satman (1990)	Single-tank	water & steam, or water, both with CO ₂	Non-isothermal for two-phase, Isothermal for water	Not stated	Implicit *	No	No	No
Sarak et al. (2005)	Up to three-tank	Water	Isothermal	Analytical	Explicit	No	No	No
Onur et al. (2008)	Single-tank	Water	Non-isothermal	Numerical ⁶	Implicit ⁵	No	No	No
Tureyen et al. (2009)	Multiple-tank	Water	Non-isothermal	Semi-numerical	Implicit ⁵	No	No	No
Satman (2010)**	Single-tank	Water	Non-isothermal	Analytical	Explicit	No	No	No
Tureyen & Akyapı (2011)	Multiple-tanks	Water	Non-isothermal	Numerical	Implicit ⁵	No	No	No
Nurlaela (2016)	Single-tank	water & steam	Non-isothermal	Numerical *	Implicit ⁵	No	No	No
Qin et al. (2017)	Multiple-tank	water & steam, or superheated steam	Non-isothermal	Numerical	Implicit ⁵	No	No	No
Firanda et al. (2021)**	Single-tank	water & steam, or water only	Non-isothermal	Numerical *	Implicit *	Yes (PSS)	Isothermal	Analytical
This study	Single-tank	Water	Non-isothermal	Analytical	Explicit	Yes (SS)	Thermal	Correlations

² According to Tureyen & Akyapı (2011)

³ Castanier et al. (1980) stated that his model is the same as Whiting & Ramey Jr. (1969), which is analytical.

⁴ According to Sarak et al. (2005)

⁵ Fully implicit Newton-Raphson procedure was implemented.

⁶ Tureyen et al. (2009) and Tureyen & Akyapı (2011) are both an extension of Onur et al., (2008)'s work. However, Tureyen et al. stated that his model is solved semi-numerically, while the other stated that his model is solved numerically, and all used fully implicit Newton-Raphson method.

* Not stated

CHAPTER 4

METHODOLOGY

This chapter discusses the methodology followed in this study, which is conducted using MS. Excel. The explicit model developed in this study covers the whole cycle of the geothermal fluid in a binary power plant utilizing low temperature geothermal reservoir as shown in Figure 4.1. The following assumptions are made:

- The single-liquid phase geothermal reservoir is radial.
- The reservoir is confined by two shale layers.
- The thickness of the overlying layer is equal to the thickness of the underlying layer.
- The reservoir is surrounded by an aquifer, of equal thickness.
- The reservoir is always at thermodynamic equilibrium. In other words, reservoir pressure and temperature can vary with time, but they do not vary spatially as the reservoir is represented by a single tank (control volume).
- Heat and mass losses due to convection (the flow out from surface manifestations such as springs) are neglected.
- The geothermal fluid is pure water.
- The whole system is at equilibrium in the natural state or prior to exploitation.
- Production and injection wells are drilled to the mid-point of the reservoir in vertical axis.
- Production and injection wells have same properties, i.e., radius, depth, etc.
- Heat losses and pressure losses in the pipes and the heat exchangers in the binary power plant are neglected.

The geothermal fluid cycle, at exploitation, is explained in the following according to the numbers depicted in Figure 4.1, which also includes a table indicating the geothermal fluid state (pressure, temperature) at each point.

- Geothermal fluid flows from the reservoir, point [1], into the bottom hole of the production well, point [2].
- The geothermal fluid flows up the production well from the bottom hole, point [2], into the well head, point [3].
- Geothermal fluid goes through the binary power plant, where its heat is converted to electrical energy, reaching to the well head of the injection well, point [4].
- The geothermal fluid is injected back into the reservoir through an injection well, where it travels from the wellhead into the bottom hole, point [5].
- Finally, geothermal fluid flows from the bottom hole of the injection well through porous media back into the reservoir, point [6].

Please note that the purpose of Figure 4.1 is to describe the model schematically. The model is not restricted to one production well and one injection well as the figure shows.

The spreadsheet model developed in this study uses macros coded by Magnus Holmgren based on 1997 International Association for the Properties of Water and Steam (IAPWS) (Sabol, 2016). The macros determine water properties such as density, isobaric heat capacity, and dynamic (absolute) viscosity at the pressure and temperature of interest. The units considered for these properties are mentioned in the first sheet of the spreadsheet. Geothermal fluid properties such as density, isobaric heat capacity, viscosity, are computed at two points in this model; at reservoir conditions (P_r, T_r) , and at the injected fluid conditions at the surface $(P_{Wh(PW)}, T_{ri})$.

Conversion factors used in this study are shown in Table 4.1. If a particular Conversion Factor (cf) was used in a particular equation mentioned here, a cf symbol is used to indicate its value and the units converted.

Table 4.1. Conversion factors (cf) used in this thesis.

From	To	Conversion factor (cf)
Pa	bar	1E-05
mD	m ²	9.869E-16
kJ	J	1E+03
MW	W	1E+06

4.1 Input Parameters and Preliminary Calculations

Parameter description is mentioned once as they hold throughout the study, unless stated otherwise. The system of notation and units is explained based on the following examples, ρ_{me} , ρ_{wj} , ρ_{wj-1} , ρ_{w0} , and ρ_{wi} .

- The main character (ρ): used to distinguish the parameter from others. The (ρ) represent density.
- The primary subscript (me/w): used to identify the main character more specifically. The (w) represents water, while (me) represents mercury.
- The secondary subscript ($j/j - 1$): used for the time index, which starts from 1, for parameters that vary with time only (mercury density ρ_m has no double subscript as it does not vary with time in this example). The time index is used in the first subscript if the parameter has no first subscript. ($j - 1$) is used to indicate the previous time index. Note that for ρ_{wj-1} , the time index is zero for ($j = 1$), ρ_{w0} , which means that the water density is computed at the initial conditions (i), $\rho_{w0} = \rho_{wi}$.

- Assuming the unit used for ρ_{me} is kg/m³, this unit also holds for ρ_w .

4.1.1 Input Parameters

Two groups of inputs must be provided to the model:

1. Production/injection scenario, which is a series of planned; production rates \dot{m}_p (kg/s) from the reservoir, injection rates \dot{m}_{ri} (kg/s) into the reservoir, and injection temperatures T_{ri} (°C) for a period of 30 years. These are provided in a tabulated form for \dot{m}_{p_j} , \dot{m}_{ri_j} and T_{ri_j} acting on the time step $\Delta t = t_j - t_{j-1}$ (seconds). For shut-in, a value of 1E-05 is substituted for both \dot{m}_p and \dot{m}_{ri} .
2. Table 4.2 shows the other necessary input parameters.

Table 4.2. Essential parameters that must be supplied into the developed model.

Parameter	Description	Unit
T_{ri}	Initial reservoir temperature	°C
ρ_m	Matrix density	kg/m ³
c_r	Rock (matrix) compressibility	1/bar
C_{pm}	Matrix isobaric heat capacity	J/(kg °C)
ϕ_i	Initial reservoir porosity	fraction
k_R	Reservoir permeability	mD
L_R	Reservoir thickness	m
r_R	Reservoir radius	m
λ_R	Reservoir thermal conductivity	W/(m °C)
Aquifer Properties		
k_A	Aquifer permeability	mD
r_A	Aquifer radius	m
T_{re}	Recharge temperature	°C
Confining layers properties		
* $\lambda_{top/bottom}$	Overlying or underlying layer thermal conductivity	W/(m °C)
* $L_{top/bottom}$	Overlying or underlying layer thickness	m
Well properties		
r_W	Well radius	m
h_{comp}	Completion thickness	m
r_n	Insulation layer inner radius	m
s	Insulation layer thickness	m
λ_n	Thermal conductivity of the installation layer	
L_W	Well length	m
ε	Well pipe absolute roughness	mm
Others		
c_w	Water compressibility	1/bar
T_s	Surface temperature	°C
η_{DHP}	Efficiency of down hole pump	fraction
η_{IP}	Efficiency of injection pump	fraction
* the forward slash “/” stands for or		

From the assumptions made earlier, the following parameters are identified for the input:

- Aquifer thickness L_A (m) is equal to L_R .
- L_{bottom} is equal to L_{top} .
- Cross-sectional area between the overlying (or underlying) layer and the reservoir $A_{top/bottom}$ (m²) is equal to the reservoir surface area A_R .
- Thermal conductivity of the overlying or underlying layers $\lambda_{top/bottom}$ (W m⁻¹ °C⁻¹) are equal to the thermal conductivity of shale λ_s .
- Due to thermodynamic equilibrium assumption for the reservoir at all times, $T_{W(PW)} = T_r$.
- As heat and pressure losses in the pipes and heat exchangers of the binary power plant are neglected,
 - Geothermal fluid temperature T_{in} and pressure P_{in} at the binary power plant inlet are equal to $T_{Wh(PW)}$ and $P_{Wh(PW)}$, respectively.
 - $P_{Wh(IW)}$ is equal to the addition of pressure supplied by the Injection Pump (IP) ΔP_{IP} to $P_{Wh(PW)}$.
 - $T_{Wh(IW)}$ is equal to the injection temperature T_{ri} .

4.1.2 Preliminary Calculations

Preliminary calculations are completed using the supplied parameters.

From the provided production/injection scenario, net production rate \dot{m}_{pn} (kg/s) is calculated using Eq. 4.1.

$$\dot{m}_{pn_j} = \dot{m}_{p_j} - \dot{m}_{ri_j} \quad 4.1$$

Reservoir initial pressure P_{r_i} (bars) is calculated based on the hydrostatic pressure corresponding to the center point depth of the reservoir, Eq. 4.2. Yet, the user can overwrite reservoir pressure to model under pressured or over pressured reservoirs.

$$P_{ri} = (cf) \rho_w g L_W \quad 4.2$$

Where cf is equal to 1E-05 (conversion from Pa to bar), water density for this calculation is taken to be 1000 kg/m³, g is the gravitational constant (9.81 m/s²).

Isothermal total compressibility c_t (bar⁻¹) is calculated using Eq. 4.3.

$$c_t = c_w + c_r \quad 4.3$$

Reservoir surface area A_R (m²) is calculated using Eq. 4.4.

$$A_R = \pi r_R^2 = A_{top} = A_{bottom} \quad 4.4$$

Volume of the reservoir V_R (m³) is calculated using Eq. 4.5.

$$V_R = A_R L_R \quad 4.5$$

Initial Pore Volume PV_i (mass) (kg) of the reservoir is calculated using Eq. 4.6.

$$PV_i = V_R \phi_i \rho_{wi} \quad 4.6$$

Initial Heat Content HC_i (J) of the reservoir is calculated using Eq. 4.7.

$$HC_i = T_{ri} V_R (\phi_{ri} \rho_{wi} C_{pw_i} + (1 - \phi_{ri}) \rho_m C_{pm}) = T_{ri} V_R (\rho_{av} C_{av})_i \quad 4.7$$

Geothermal gradient G (°C/m) is determined using Eq. 4.8.

$$G = \frac{T_{ri} - T_s}{L_W - \frac{L_R}{2}} \quad 4.8$$

The distance between the centers of the reservoir and the overlying or underlying layer $d_{top/bottom}$ (m) is calculated using Eq. 4.9.

$$d_{top/bottom} = \frac{L_{top/bottom}}{2} + \frac{L_R}{2} \quad 4.9$$

Temperature at the center of the overlying layer T_{top} (°C) is calculated using Eq. 4.10.

$$T_{top} = T_s + G \left(L_W - \frac{L_R}{2} - \frac{L_{top}}{2} \right) \quad 4.10$$

Temperature at the center of the underlying layer T_{bottom} (°C) is calculated using Eq. 4.11.

$$T_{bottom} = T_{r_i} + G \left(\frac{L_{bottom}}{2} \right) \quad 4.11$$

4.2 Reservoir Model

Temperature and pressure changes of a single-liquid phase geothermal reservoir under exploitation of variable production/injection rates and shut in, is estimated using an explicit single-tank LPM.

4.2.1 Modified Lumped-Parameter Model

The LPM developed in this study, is a modification to the ones developed by Satman (2010) and Sarak et al. (2005). Satmans explicit model was modified to model variable production rate, injection rate, and injection temperature. In addition, geothermal fluid properties (density and heat capacity) were updated for every time index rather than assuming a constant density and constant isobaric heat capacity as in Satman's work. Furthermore, heat transfer due to conduction was also modeled rather than assuming it constant as in Satmans work. The same nomenclature used by Satman (explained in 3.3.3 Literature Review) is used here unless stated otherwise.

Water influx from a lateral radial aquifer surrounding the radial geothermal reservoir (edge drive), as shown in Figure 4.2, flowing at steady state is modeled using Schilthuis (1936) method. The recharge rate \dot{m}_{re} (kg/s) is determined by applying Darcy equation, Eq. 4.12 (the reader is referred to Appendix A for a detailed derivation).

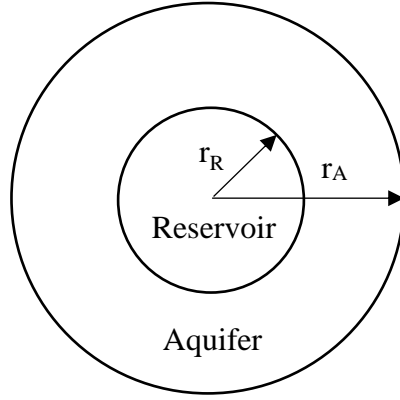


Figure 4.2. Top view of a radial aquifer surrounding radial reservoir.

$$\dot{m}_{rej} = \alpha (P_{re} - P_{rj}) = \alpha (P_{ri} - P_{rj}) = \alpha \Delta P_{rj} \quad 4.12$$

Where recharge constant or recharge index α ($\text{kg bar}^{-1}\text{s}^{-1}$) is defined in Eq. 4.13, P_{re} is the constant pressure of the recharge source, which equals the initial reservoir pressure P_{ri} (bar) or reservoir pressure P_r (bar) at time zero ($P_{re} = P_r(t = 0) = P_{ri}$) due to equilibrium at time equal zero (Sarak et al., 2005). The difference between initial reservoir pressure and the reservoir pressure at time t, is the reservoir pressure drawdown ΔP_r .

$$\alpha = cf \frac{2\pi L_A k_A \rho_w}{\mu_w \ln\left(\frac{r_A}{r_R}\right)} \quad 4.13$$

Recharge water viscosity μ_w (bar.s) and its density ρ_w (kg/m^3), are computed at P_{ri} and T_{re} . cf is equal to $9.869\text{E-}16$ (conversion from mD to m^2)

Pressure of a low temperature geothermal reservoir, under exploitation or shut-in, at time t P_{rj} (bar) is modeled using Eq. 4.14 (Alp, 2021). The reader is referred to Appendix B for the detailed derivation.

$$P_{rj} = P_{rj-1} + \left(\Delta P_{rj-1} - \frac{\dot{m}_{pnj}}{\alpha} \right) (1 - e^{-D_{j-1}\Delta t}) \quad 4.14$$

Constant D is defined in Eq. 4.15.

$$D_{j-1} = \frac{\alpha}{\kappa_{j-1}} = \frac{\alpha}{V_r c_t \phi_{r,j-1} \rho_{w,j-1}} \quad 4.15$$

Change of porosity with reservoir pressure is defined in Eq. 4.16.

$$\phi_{r,j-1} = \phi_i (1 - c_r \Delta P_{r,j-1}) \quad 4.16$$

Temperature of a low temperature geothermal reservoir, under exploitation or shut-in, at time t T_r (°C) is modeled using Eq. 4.17 (the reader is referred to Appendix C for the detailed derivation).

$$\begin{aligned} T_{r,j} = & T_{r,j-1} e^{-a_{j-1} \Delta t} \\ & + \frac{c_{j-1}}{a_{j-1}} \left(\Delta P_{r,j-1} (1 - e^{-a_{j-1} \Delta t}) \right. \\ & \left. - \left(\Delta P_{r,j-1} - \frac{\dot{m}_{pn,j}}{\alpha} \right) ((1 - e^{-a_{j-1} \Delta t}) \right. \\ & \left. - \frac{a_{j-1}}{a_{j-1} - D_{j-1}} (e^{-D_{j-1} \Delta t} - e^{-a_{j-1} \Delta t}) \right) + \left(\frac{g_{j-1}}{a_{j-1}} + \frac{x_{j-1}}{a_{j-1}} \right) (1 \\ & - e^{-a_{j-1} \Delta t}) \end{aligned} \quad 4.17$$

Constants; a , c , g , and x are defined in Eq. 4.18, Eq. 4.19, Eq. 4.20, and Eq. 4.21, respectively.

$$a_{j-1} = \frac{\dot{m}_{p,j} C_{pw,j-1}}{V_R (\rho_{av} C_{av})_{j-1}} \quad 4.18$$

$$c_{j-1} = \frac{\alpha C_{pwre} T_{re}}{V_R (\rho_{av} C_{av})_{j-1}} \quad 4.19$$

$$g_{j-1} = \frac{\dot{m}_{ri,j} C_{pwri,j} T_{W(IW),j}}{V_R (\rho_{av} C_{av})_{j-1}} \quad 4.20$$

$$x_{j-1} = \frac{Q_{n,j-1}}{V_R (\rho_{av} C_{av})_{j-1}} \quad 4.21$$

Note that parameters which depend on reservoir pressure and temperature, such as density of water ρ_w , isobaric heat capacity of water C_{pw} , net conductive heat flow

Q_n (J/s), and reservoir heat content per unit volume per unit temperature $\rho_{av}C_{av}$ (J °C⁻¹m⁻³), defined in Eq. 4.22, are always computed at t_{j-1} except C_{pwri_j} as it is computed at $(P_{W(IW)}, T_{W(IW)})$.

$$(\rho_{av}C_{av})_{j-1} = \phi_{rj-1}\rho_{wj-1}C_{pwj-1} + (1 - \phi_{rj-1})\rho_mC_{pm} \quad 4.22$$

In case reservoir temperature at the beginning of shut-in period (end of a production period) is higher than the recharge temperature $T_r > T_{re}$, constant c in Eq. 4.17 is replaced by constant c' , Eq. 4.23. The recharge in such case cools the reservoir rather than heating it.

$$c'_{j-1} = -\frac{\alpha C_{pwre}(T_{rj-1} - T_{re})}{V_R(\rho_{av}C_{av})_{j-1}} \quad 4.23$$

Conductive heat flow is modeled for both Q_{bottom} and Q_{top} using Eq. 4.24, which is based on Eq. 3.24 of Tureyen & Akyapı (2011)'s model (Fourier's law).

$$Q_{topj-1} = \gamma_{top}(T_{top} - T_{rj-1}) \quad 4.24$$

Where γ is the conduction index (W/°C) defined in Eq. 4.25, T_{top} is the constant temperature at the center of the overlying layer. Subscript “top” is replaced by “bottom” for the calculation of Q_{bottom} . Note that Q_{top} is less than 0 (loss) when reservoir temperature is higher than T_{top} . While Q_{bottom} is higher than zero (gain) when reservoir temperature is less than T_{bottom} .

$$\gamma_{top} = \frac{\lambda_{A_{top}}A_{top}}{d_{top}} \quad 4.25$$

where λ_A is the average thermal conductivity of the medium determined using harmonic averaging (Eq. 4.26). Subscript “top” is replaced by “bottom” for the calculation of γ_{bottom} .

$$\lambda_{A_{top}} = \frac{L_R + L_{top}}{\frac{L_R}{\lambda_R} + \frac{L_{top}}{\lambda_{top}}} \quad 4.26$$

Subscript “top” is replaced by “bottom” for the calculation of $\lambda_{A_{top}}$. Note that $\lambda_{A_{top}} = \lambda_{A_{bottom}}$ and $\gamma_{top} = \gamma_{bottom}$.

Net conductive heat flow is the sum of Q_{top} and Q_{bottom} as in Eq. 4.27. Note that at $t = 0$, $Q_{bottom} = Q_{top}$ ($Q_n = 0$).

$$Q_{n_{j-1}} = Q_{bottom_{j-1}} + Q_{up_{j-1}} \quad 4.27$$

4.2.1.1 Verification of the Modified LPM

The verification of the modified LPM used in this study has been done on three stages. The objective of the first stage is to verify the ability of Eq. 4.14 to model the pressure behavior for a low temperature geothermal reservoir under variable production/injection rates (net production rate). The objective of the second stage is to verify the ability of Eq. 4.14 and Eq. 4.17 to model the pressure behavior and temperature behavior under exploitation and shut-in, which also verifies the ability of Eq. 4.17 to model the temperature behavior for variable production/injection rates (net production rate) if successful. In the final stage, the modified LPM is verified against TOUGH2 code (using PETRASIM) to find the accuracy of the LPM derived in this study for exploitation and shut in.

4.2.1.1.1 First Stage

Derived pressure behavior equation, Eq. 4.14, is verified against Eq. 3.13 of Sarak et al. (2005), for the modelling of various production/injection rates (net production rate). The net production rate scenario used is shown in Figure 4.3. The production/injection scenario lasts for 80 years, where the production/injection rate (net production rate) is changing every 20 years from 10, to 30, to 40, and to 80 kg/s, respectively. The rest of the involved parameters such as α , κ , and P_{ri} are set constant and equal to 45 kg/(bar.s), $4.3E+9$ kg/bar, and 50 bar, respectively.

$$\Delta P_r(t) = \sum_{j=1}^n \frac{\Delta \dot{m}_{pn}(t_j)}{\alpha} (1 - e^{-\frac{\alpha}{\kappa}(t-t_{j-1})}) \quad 3.13$$

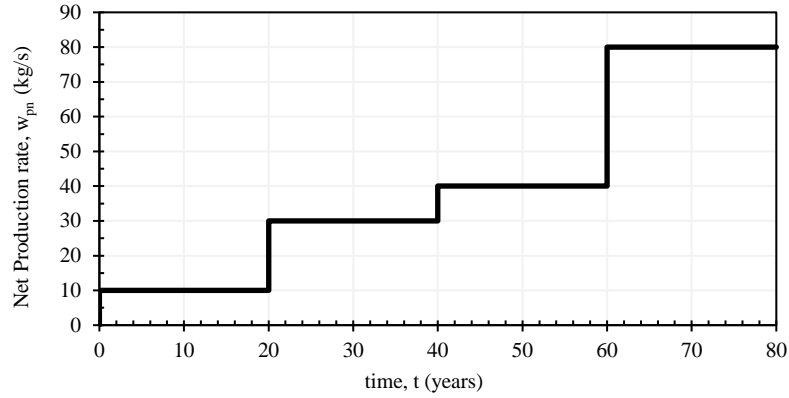


Figure 4.3. Net production rate scenario used for verification of Eq. 4.14 results.

As shown in Figure 4.4, the results obtained from the derived pressure behavior equation for a single-liquid phase geothermal reservoir, Eq. 4.14, matches perfectly with the results obtained from Eq. 3.13, which verifies the ability of Eq. 4.14 to model variable production/injection rates (net production rate).

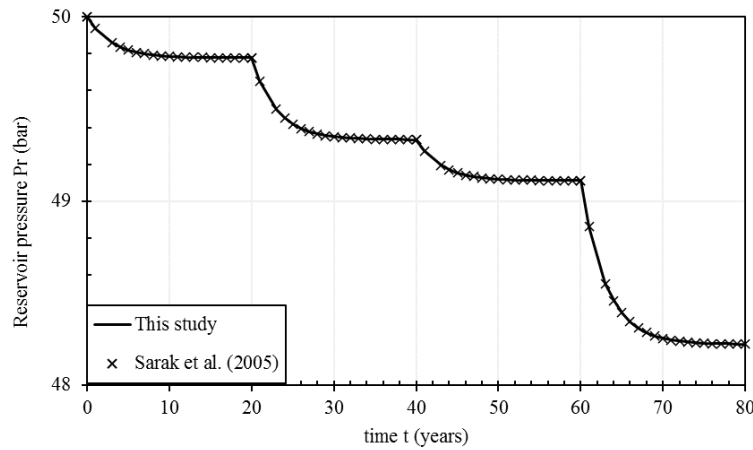


Figure 4.4. Verification of the results obtained using the derived Eq. 4.14 in this study against the results of Eq. 3.13 of Sarak et al. (2005)'s.

4.2.1.1.2 Second Stage

Derived temperature behavior equation, Eq. 4.17, is verified against the model developed by Satman (2010) for exploitation and shut-in using the set of data in Satman's work, Table 4.3. The reservoir in this verification is produced for 80 years under a constant production/injection rate and then shut-in for the next 80 years. Thus, production/injection rates are varied.

Table 4.3. Data set used for the verification of Eq. 31 (Satman, 2010).

Parameter	Value	Unit
T_{ri}	210	°C
P_{ri}	50	bar
\dot{m}_p	270	kg/s
\dot{m}_{ri}	135	kg/s
\dot{m}_{pn}	135	kg/s
$\rho_{av}C_{av}$	2.50E+06	J/(m ³ °C)
V_R	1.20E+10	m ³
C_{pw}	4100	J/(kg °C)
κ	4.30E+09	kg/bar
Q_n (constant)	3.00E+07	J/s
α	41.22	kg/(bar s)
T_{re}	180	°C
T_{ri}	90	°C
C_{pwre}	4387.94	J/(kg °C)
C_{pwri}	4193.58	J/(kg °C)

In Satman's model, Eq. 3.10 and Eq. 3.15, are used to model the pressure and temperature behaviors of the reservoir under exploitation, respectively. While, in the current model Eq. 4.14 and Eq. 4.17 are used. Constants of the modified model; a , D , c , g , and x , are kept constant through the production period to be consistent with Satman's model limitations. Parameter $T_{W(IW)}$ in constant g (Eq. 4.20) of Eq. 4.17 is replaced by T_{ri} as Satman's model is limited to the reservoir only (does not encompass a well model).

$$\Delta P_r(t) = P_{r_i} - P_r(t) = \frac{\dot{m}_{pn}}{\alpha} (1 - e^{-\frac{\alpha}{\kappa} t}) \quad 3.10$$

$$T_r = T_{r_i} e^{-at} + \frac{b'}{a} \left(1 + \frac{D}{a-D} e^{-at} - \frac{a}{a-D} e^{-Dt} \right) + \left(\frac{g}{a} + \frac{x}{a} \right) (1 - e^{-at}) \quad 3.15$$

As shown in Figure 4.5 and Figure 4.6, The modified LPM matches the results obtained by Satman's model perfectly for reservoir pressure and reservoir temperature, respectively, for the first 80 years production period.

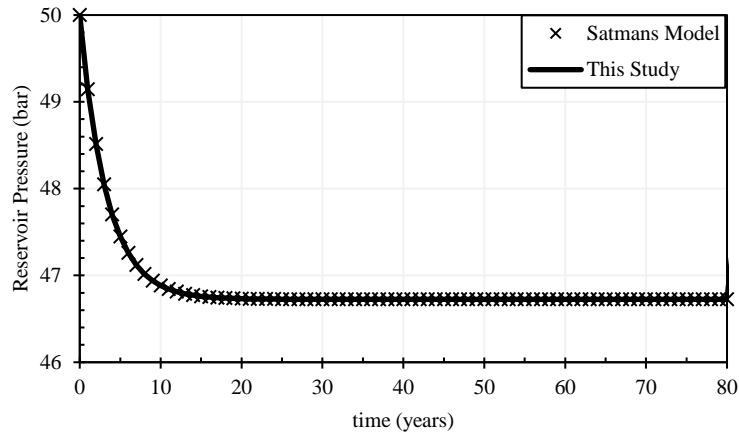


Figure 4.5. Results of reservoir Pressure obtained using Satman's Model and this study's LPM for the first 80 years production period.

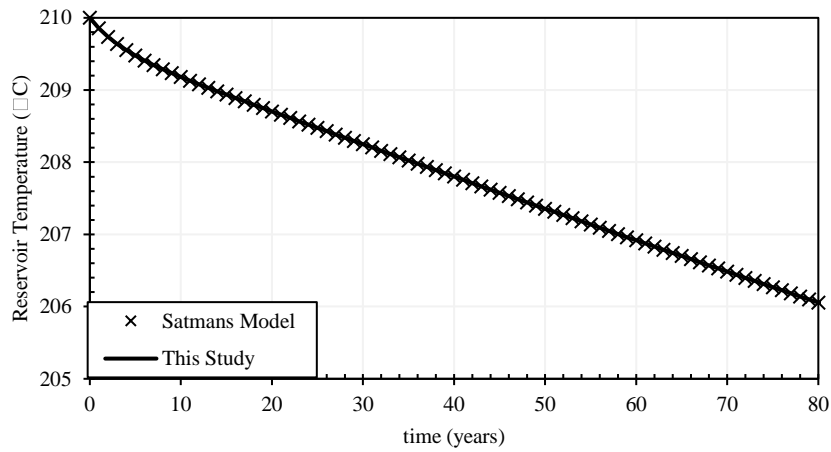


Figure 4.6. Results of reservoir temperature obtained using Satman's Model and this study's LPM for the first 80 years production period.

For the second 80 years shut-in period, Eq. 3.21 and Eq. 3.23 of Satman's were used. Note that Eq. 3.23 is used as the reservoir temperature at the end of the production period, which is approximately 206 °C, is higher than that of recharge $T_{re} < T_{rp}$. For the modified LPM model, the same equations used in the production period, Eq. 4.14 and Eq. 4.17, are also used for modelling reservoir pressure and temperature behaviors, respectively. However, constants a and g are recalculated due to the small value of production rate and injection rate ($\dot{m}_p = \dot{m}_{ri} = 10^{-5}$), and constant c of Eq. 4.17 is replaced by constant c' , Eq. 4.23.

$$\Delta P_r(\Delta t_p) = P_{ri} - P_r(\Delta t_p) = \frac{\dot{m}_{pn}}{\alpha} e^{-D\Delta t_p} (1 - e^{-Dt_p}) \quad 3.21$$

$$T_r(\Delta t_p) = T_{rp} + x\Delta t_p - \frac{C_{pwre}(T_{rp} - T_{re})\dot{m}_{pn}}{V_R \rho_{av} C_{av} D} (1 + e^{-Dt} - e^{-D\Delta t_p} - e^{-Dt_p}) \quad 3.23$$

A perfect match was obtained between the results of Satman's model and the modified LPM, as well, for both reservoir pressure and reservoir temperature for the second 80 years shut-in as shown in Figure 4.7 and Figure 4.8, respectively. This verifies; the ability of Eq. 4.14 and Eq. 4.17 to model low temperature geothermal reservoir behavior in terms of pressure and temperature under exploitation and shut-in, and the ability of Eq. 4.17 to model temperature behavior for variable production/injection rates.

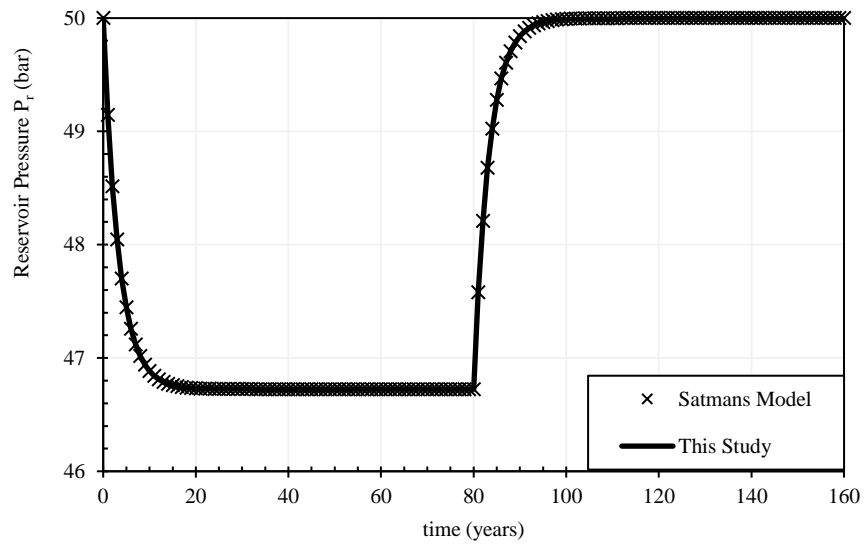


Figure 4.7. Results of reservoir Pressure obtained using Satman's Model and this study's LPM for 80 years of production and another 80 years of shut-in.

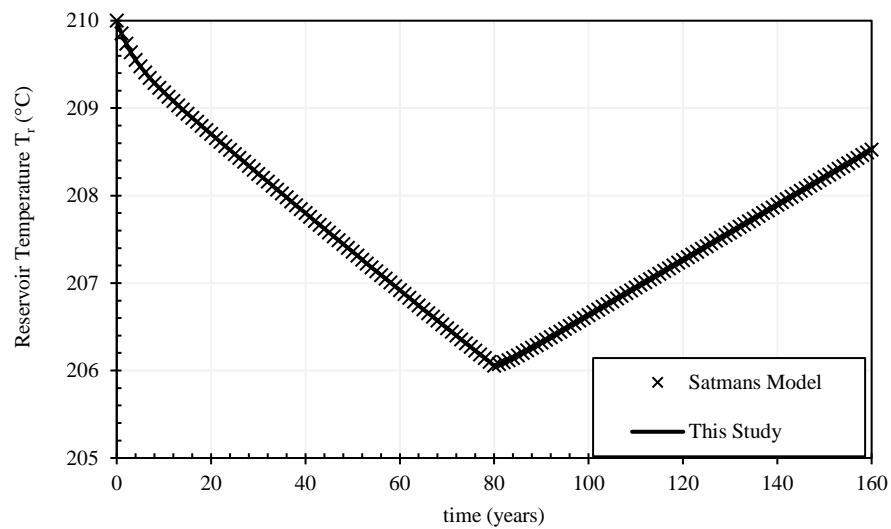


Figure 4.8. Results of reservoir temperature obtained using Satman's Model and this study's LPM for 80 years of production and another 80 years of shut-in.

4.2.1.1.3 Third Stage

The reservoir model created for TOUGH2 in Onur et al. (2008) to verify their LPM model, was duplicated in this study for the same purpose to find the accuracy of the modified LPM.

The reservoir model is composed of 21 cells (or grid blocks), where an injection well and a production well exist in the middle of the model (11th cell) as shown in Figure 4.9. Parameters assigned for this model are shown in Table 4.4, where h_{ri} is the injection enthalpy. Constant pressure and temperature boundary is assigned at the sides of the reservoir (1st and 21st cells) to model the recharge into the reservoir. Reservoir permeability is determined using the relationship derived by Ay (2005), Eq. 4.28, which finds the reservoir permeability k_R that equates the amount of flow from the outer boundaries to the wells, with the recharge constant α assigned for the modified LPM.

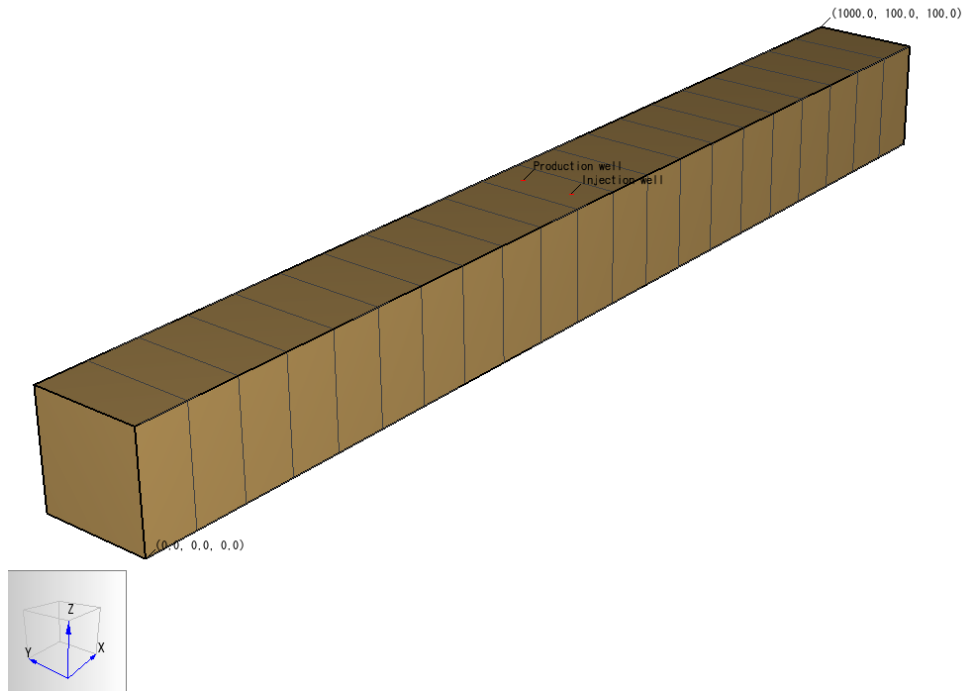


Figure 4.9. Reservoir model created on PETRASIM to verify the modified LPM used in this study against TOUGH2.

Table 4.4. TOUGH2 model input parameters (Onur et al., 2008).

Parameter	Value	Unit
ϕ_i	0.2	[fraction]
c_r	1.33E-04	bar ⁻¹
ρ_w^*	928.5	kg/m ³
μ_w^*	2.024E-09	bar.s
ρ_m	2650	kg/m ³
C_m	1000	J/(kg °C)
V_R	1E+07	m ³
P_{ri}	50	bar
$T_{ri} = T_{re}$	140	°C
T_{ri}	60	°C
h_{ri}	255.3	kJ/kg
Q_n	0	J/s
α	1	kg s ⁻¹ bar ⁻¹
k_R	2.719E-14	m ²
*At reservoir initial condition (P_{ri}, T_{ri})		

$$\alpha = 8 \frac{w L_R}{L_x} \frac{k_R}{\mu_w} \rho_w \quad 4.28$$

where the product of reservoir width w and its thickness L_R is the cross-sectional flow area, L_x is the length of the reservoir along the x-axis, and μ_w is the water viscosity.

For a recharge constant of unity, given water density and viscosity at the initial conditions, given cross-sectional flow area, and given length, reservoir permeability is determined to be 2.719E-14 m² (≈ 27.6 mD). This permeability and given porosity of 0.2 are assigned to all 21 cells.

For the modified LPM, $C_{p_{wri}}$ is computed at initial reservoir pressure and injection temperature, and $C_{p_{wre}}$ is computed at the initial reservoir pressure and recharge temperature.

Parameter $T_{W(IW)}$ in constant g (Eq. 4.20) of Eq. 4.17 is replaced by T_{ri} as TOUGH2 is a reservoir simulator only (does not encompass a well model).

The assigned production/injection scenario is shown in Figure 4.10, Which is composed of 2 production periods that have a net production rate of 5 kg/s, separated by a shut-in period. Each period lasts for 10 days.

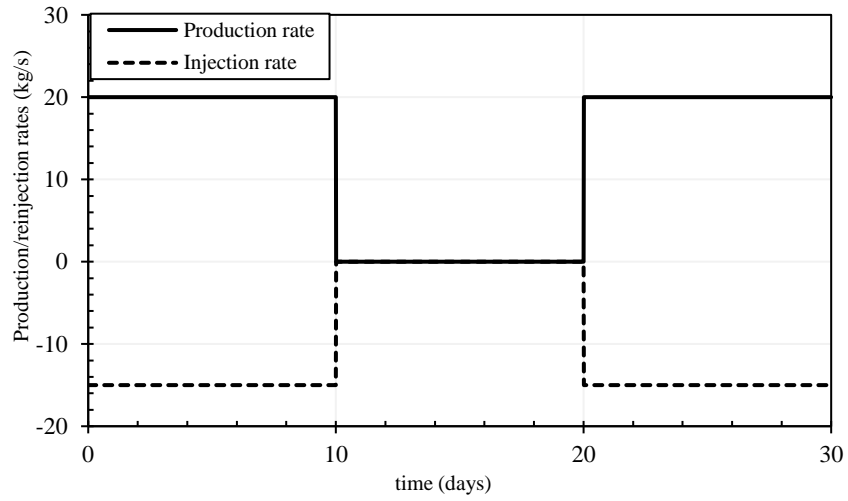


Figure 4.10. Production/injection scenario used for the third stage verification (Onur et al., 2008).

After running the code (simulation), the results from the 21 cells (in terms of cell pressure and cell temperature) are averaged to determine reservoir pressure and reservoir temperature, which are compared with the reservoir pressure results and reservoir temperature results obtained from the modified LPM used in this study. The comparison of the results is based on the error percentage, which is determined using Eq. 4.29.

$$Error (\%) = \frac{x_{MLPM} - x_{TOUGH2}}{x_{TOUGH2}} * 100 \quad 4.29$$

where x is the parameter to be investigated (e.g., reservoir pressure P_r , or reservoir temperature T_r). Subscript *MLPM* stands for the Modified LPM used in this study.

Figure 4.11 shows the reservoir pressure results obtained from TOUGH2 and this study, and the error percentage between the results. Given the narrow y-axis scale, the results of the modified LPM in this study are in an excellent match with TOUGH2 results. The error percentage did not exceed $\pm 1\%$.

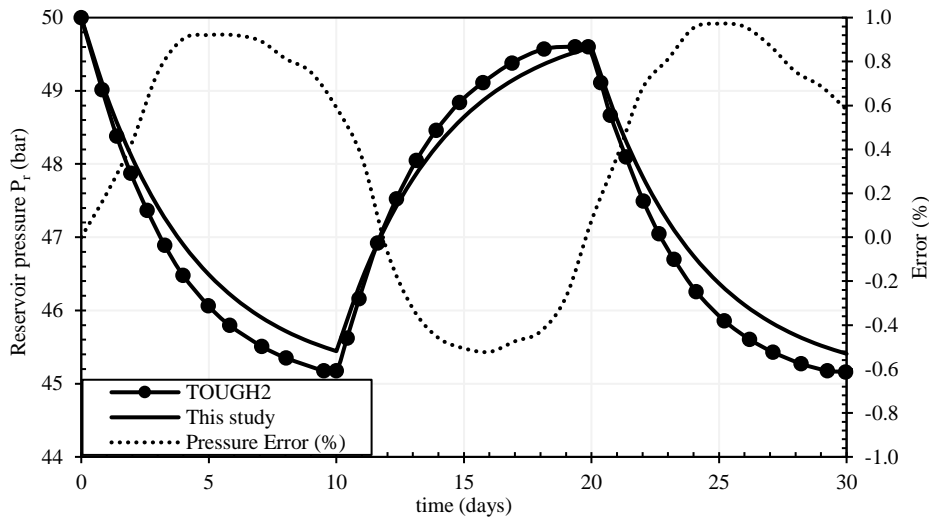


Figure 4.11. Results of reservoir pressure obtained from TOUGH2, and this study.

In addition to error percentage between the results of TOUGH2 and this study.

Figure 4.12 shows the reservoir temperature results obtained from TOUGH2 and this study, and the error percentage between the results. Given the narrow y-axis scale, the results of the modified LPM in this study are in an excellent match with TOUGH2 results. The error percentage is much less $\pm 1\%$.

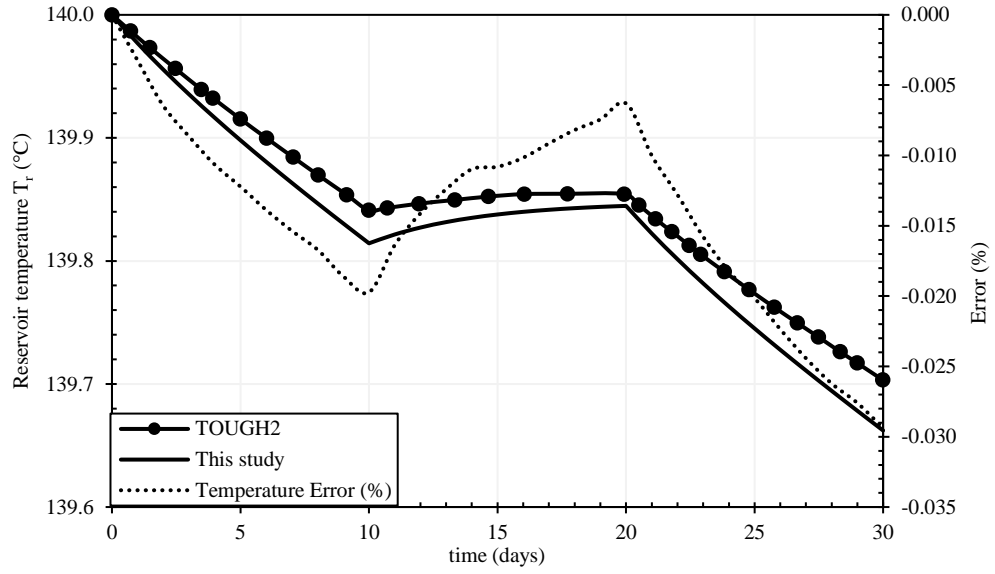


Figure 4.12. Results of reservoir temperature obtained from TOUGH2, and this study. In addition to error percentage between the results of TOUGH2 and this study.

The conductive heat flow, Eq. 4.24, and the following parts of the modified LPM have not been verified separately as they are well-established in the literature.

4.3 Production Well Model

The simple steady state production well model includes the flow of the geothermal fluid from the reservoir to the inlet of the binary power plant through the production well.

Please note that; all the production wells have the same properties (e.g., well length, absolute roughness, etc.). Fluid properties are determined at reservoir conditions (P_r, T_r) at the beginning of the time step. Based on these fluid properties, secondary flow parameters are calculated, and they are assumed to prevail during that time step Δt .

4.3.1 Preliminary Calculations

Number of production wells are determined based the production rates and the average flow rate from a single production well. The average production rate from a single well, according to Snyder et al., (2017), for binary power plant is 112 L/s (according to the author, the average flow rate is volume-based as all operators provide their monthly reports in volume-based rates rather than mass-based rates). Assuming water density of 997 kg/m³ (at 1 atm and 25 °C), the mass-based average flow rate is 112 kg/s approximately. For further simplicity, the average flow rate is taken as 100 kg/s. This assumption is valid as the density of water at production conditions (higher temperature and higher pressure) is lower than 997 kg/m³. 100 kg/s is assumed to be the average production rate from a single production/injection well. Thus, number of production wells n_p is calculated using Eq. 4.30. If the production rate is less than the average production rate from a single production well, single production well is used.

$$n_{p_j} = \frac{\dot{m}_{p_j} - \text{Remainder} \left(\frac{\dot{m}_{p_j}}{100} \right)}{100} \quad 4.30$$

The production rate from a single production well $\dot{m}_{p(PW)}$ is calculated using Eq. 4.31.

$$\dot{m}_{p(PW)_j} = \frac{\dot{m}_{p_j}}{n_{p_j}} \quad 4.31$$

4.3.2 Steady State Reservoir-Production Well Model

The flow of fluid in an idealized porous medium under steady state conditions, is modeled using Darcy's law, Eq. 4.32.

$$\dot{V}_w = \frac{k_R A}{\mu_w} \frac{dP}{dr} \quad 4.32$$

For a production well located at the center of a radial homogeneous reservoir as shown in Figure 4.13, bottom-hole production pressure $P_{W(PW)}$ is calculated using Eq. 4.33 (DiPippo, 2008). The reader is referred to Appendix D for the detailed derivation of Eq. 4.33.

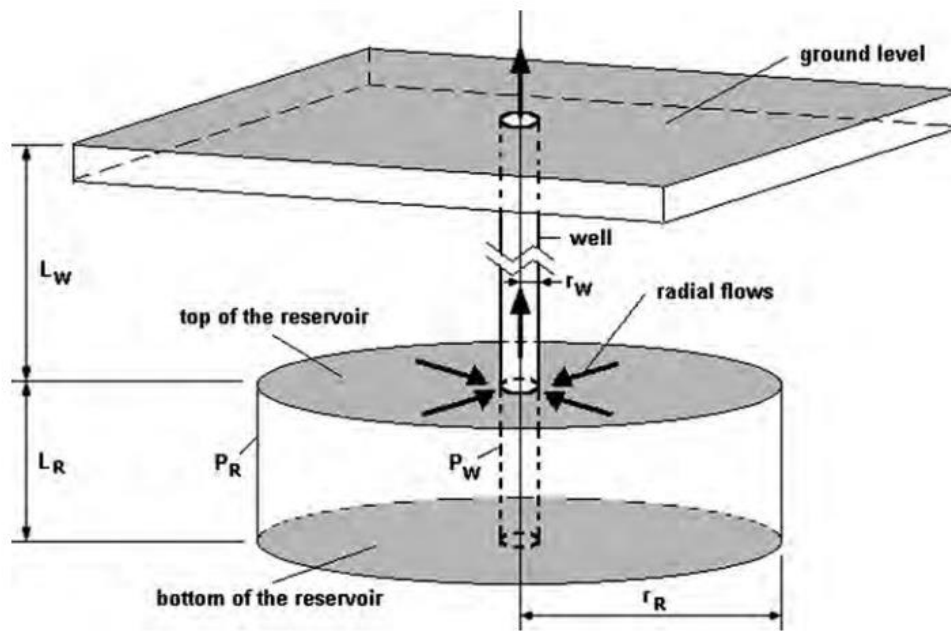


Figure 4.13. Schematic of radial reservoir, where the fluid flows from the undisturbed far-field reservoir into the well (DiPippo, 2008)

$$P_{W(PW)_j} = P_{r_{j-1}} - C_{Dj-1} \dot{m}_{p(PW)_j} \quad 4.33$$

Where C_D is the drawdown coefficient (bar.s.kg^{-1}) defined in Eq. 4.34, which is equal to the inverse of the productivity index J (DiPippo, 2008) and the injectivity index II (Leaver, 1986).

$P_{W(PW)_j}$ implies that, per steady state reservoir-to-wellbore flow model, $P_{W(PW)}$ is assumed constant during Δt duration between time j and $j - 1$. However, in the next

timestep, it changes as other parameters change. The same applies for the rest of the calculated parameters in this section.

$$C_{Dj-1} = \frac{1}{J_{j-1}} = \frac{1}{II_{j-1}} = \frac{1}{cf} \frac{\ln\left(\frac{r_R}{r_W}\right)}{2\pi k_R h_{comp}} \frac{\mu_{wj-1}}{\rho_{wj-1}} \quad 4.34$$

4.3.3 Liquid Steady State Model for the Flow in the Production Well

This model includes the calculation of pressure and temperature of the geothermal fluid within the production well, where the geothermal fluid travels from the bottom-hole to the well head of the production well.

The production well is assumed to have constant properties throughout its length. Figure 4.14 shows the top view of the well. The well has an inner radius of r_W (well radius) surrounded by an insulation layer of an inner radius r_n and thickness of s .

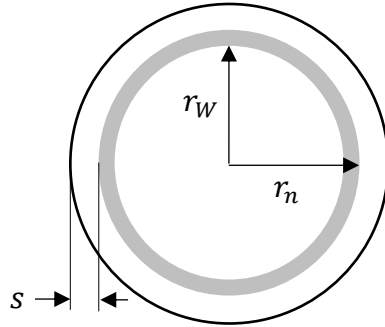


Figure 4.14. Schematic illustration of the top view of the well.

Cross-sectional flow area in the well A_f (m^2) is calculated using Eq. 4.35.

$$A_f = \pi r_W^2 \quad 4.35$$

The flow velocity of the geothermal fluid in the production well v_{PW} (m/s) is calculated using Eq. 4.36.

$$v_{PWj} = \frac{\dot{m}_{p(PW)j}}{A_f \rho_{w_{j-1}}} \quad 4.36$$

4.3.3.1 Temperature Behavior

For the steady state flow of the geothermal fluid in an element of the production well ΔL shown in Figure 4.15. Heat balance is applied, Eq. 4.37.

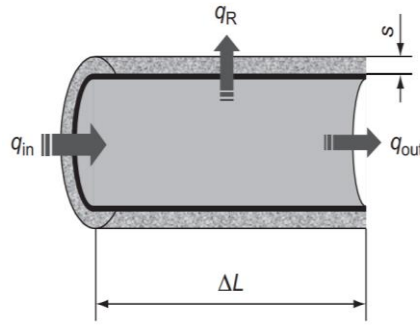


Figure 4.15. Side view schematic of a portion of the well (Guo et al, 2013).

$$q_{in} - q_{out} - q_R = q_{acc} \quad 4.37$$

Where q_{in} (J) is the heat energy entering the well element by the geothermal fluid due to convection, q_{out} is the heat energy existing the well element by the geothermal fluid due to convection, q_R is the heat energy transferred through the insulation layer due to conduction, and q_{acc} is the accumulated heat energy in the well element. These terms are further formulated and discussed in Appendix F, where the detailed derivation of the following equations in this section are also discussed.

For a fluid flowing up through the production well, its temperature at elevation L_W from the bottom-hole (well head production temperature) $T_{Wh(PW)}$ is determined using Eq. 4.38 for steady state conditions (Guo et al, 2013).

$$T_{Wh(PW)j} = \frac{1}{\alpha_c^2}_{j-1} (\beta_c - \alpha_c \beta_c L_W - \alpha_c \gamma_c - e^{-\alpha_c(L_W + c_{prod})}) \quad 4.38$$

Where constants α_c , β_c , γ_c , and C_{prod} , are defined in Eq. 4.39, Eq. 4.40, Eq. 4.41, and Eq. 4.42, respectively.

$$\alpha_{c_{j-1}} = \frac{2\pi r_n \lambda_n}{s A_f} \frac{1}{v_{PW_j} \rho_{w_{j-1}} C_{pw_{j-1}}} \quad 4.39$$

$$\beta_{c_{j-1}} = \alpha_{c_{j-1}} G \cos(\theta) \quad 4.40$$

$$\gamma_{c_{j-1}} = -\alpha_{c_{j-1}} T_{f,0_{j-1}} = -\alpha_{c_{j-1}} T_{r_{j-1}} \quad 4.41$$

Where $T_{f,0}$ is the temperature of the medium outside the insulation layer at the bottom hole of the production well, which is equal to the reservoir temperature as the reservoir is assumed to be always in thermodynamic equilibrium.

$$C_{prod_{j-1}} = -\frac{1}{\alpha_{c_{j-1}}} \ln \left(\beta_{c_{j-1}} - \alpha_{c_{j-1}}^2 T_{W(PW)_{j-1}} - \alpha_{c_{j-1}} \gamma_{c_{j-1}} \right) \quad 4.42$$

4.3.3.2 Pressure Behavior

Momentum equation (Newton's Second Law of Motion) of fluid mechanics is applied to the flow of liquid only in the production well, Eq. 4.43, where the following equations presented in this section are different solutions of Eq. 4.43. The reader is referred to Appendix G for the detailed derivation and discussion.

$$-dP - \frac{dF}{A_f} - \rho_w g dz = \rho_w v dv \quad 4.43$$

Where F is the friction force calculated using the friction factor f (unitless) computed using Swamee-Jain equation, Eq. 4.44 (Swamee & Jain, 1976). Please note that DiPippo (2008) has made a slight mistake in the definition of this constant, regarding Fanning and Darcy friction factors. This has been corrected here. The reader is referred to Appendix G for further information,

$$f_{j-1} = \frac{0.25}{\left(\log_{10} \left(\frac{\varepsilon/D}{3.7} + \frac{5.74}{Re^{0.9}_{j-1}} \right) \right)^2} \quad 4.44$$

where Re is Reynolds number (unitless) calculated using Eq. 4.45.

$$Re_{j-1} = cf \frac{D_W}{A_f} \frac{\dot{m}_{p(PW)_j}}{\mu_{w_{j-1}}} \quad 4.45$$

Where cf is 1E-05 (conversion factor from bar to Pa)

4.3.3.3 Flash Horizon

Flash horizon L_f (m), which is the elevation (from the bottom hole) where geothermal fluid pressure becomes equal to the saturation pressure (vaporization starts), is calculated using Eq. 4.46 (DiPippo, 2008).

$$L_{fj} = \frac{1}{cf} \frac{P_{W(PW)_j} - P_{sat}(T_{r_{j-1}})}{(C_{2j-1} w_{p(PW)_j}^2 + \rho_{w_{j-1}} g)} \quad 4.46$$

Where cf is equal to 1E-05 (conversion from Pa to bar), constant C_2 ($\text{kg}^{-1} \text{m}^{-2}$) is defined in Eq. 4.47, $P_{sat}(T_{r_{j-1}})$ is the saturation pressure at reservoir temperature – Geothermal fluid temperature does decrease while traveling up the production well. Thus, the saturation pressure also decreases up along the wellbore. However, as a worst-case scenario L_f is placed at the lowest point below the wellhead using the reservoir temperature to calculate P_{sat} .

$$C_{2j-1} = \frac{8}{\pi^2 D_W^5} \frac{f_{j-1}}{\rho_{w_{j-1}}} \quad 4.47$$

Where f is the friction factor.

In case, $L_f \geq (L_W + 50 \text{ m})$, there would be no need for a downhole pump $\Delta P_{DHP} = 0$ (50 m is added arbitrarily as a safety margin so that geothermal fluid does not reach the well head of the production well having a pressure equal exactly to the saturation

pressure). Otherwise, downhole pump supplies the geothermal fluid with the needed pressure ΔP_{DHP} so that $L_f = (L_W + 50 \text{ m})$ as in Eq. 4.48.

$$\Delta P_{DHPj} = cf \left(C_{2j-1} w_{p(PW)_j}^2 + \rho_{wj-1} g \right) ((L_W - L_f) + 50 \text{ m}) \quad 4.48$$

Where cf is equal to 1E-05 (conversion from Pa to bar).

DHP power requirement W_{DHP} (MW) is calculated using Eq. 4.49.

$$W_{DHPj} = \frac{cf}{\eta_{DHP}} \Delta P_{DHPj} \frac{\dot{m}_{p(PW)_j}}{\rho_{wj-1}} \quad 4.49$$

Where cf is equal to 10 (conversion from bar to Pa and from W to MW).

Well head production pressure $P_{Wh(PW)}$ is calculated using Eq. 4.50.

$$P_{Wh(PW)_j} = P_{W(PW)_j} + \Delta P_{DHPj} - cf \left(C_{2j-1} \dot{m}_{p(PW)_j}^2 + \rho_{wj-1} g \right) L_W \quad 4.50$$

Where cf is equal to 1E-05 (conversion from Pa to bar).

4.4 Binary Power Plant

This model is mostly based on two correlations, which are used to determine: the conversion efficiency of a binary power plant from thermal energy to electrical energy η_{act} , and the geothermal fluid temperature at the outlet of the binary power plant (after the energy conversion) T_{out} .

Enthalpy of the geothermal fluid at binary power plant inlet h_{in} (kJ/kg) is determined based on geothermal fluid pressure and temperature at the wellhead of the production well, Eq. 4.51.

$$h_{inj} = h(P_{Wh(PW)_j}, T_{Wh(PW)_j}) \quad 4.51$$

The conversion efficiency of a binary power plant η_{act} (%) is determined using Zarrouk & Moon (2014) correlation, Eq. 2.1.

$$\eta_{actj}(\%) = 6.6869 \ln(h_{inj}) - 37.929 \quad 2.1$$

The running capacity of a binary power plant W (MW_e) is determined using Eq. 4.52 (Zarrouk & Moon, 2014).

$$W_j = cf \frac{\eta_{actj}}{100} \dot{m}_{pj} h_{whj} \quad 4.52$$

where cf is equal to 1E-03 (conversion from kJ to J and from W to MW).

Fluid temperature after its thermal energy has been converted to electrical energy, or at the binary power plant outlet T_{out} , is calculated using Tester et al. (2006) correlation, Eq. 2.2.

$$T_{outj} = T_{Wh(IW)_j} = T_{inj} + cf \frac{W_j / \dot{m}_{pj}}{0.098701 - 0.0039645 T_{inj}} \quad 2.2$$

Where cf is equal to 1E+03 (conversion from MW to kW). Note that $T_{outj} = T_{rij}$ in case the direct injection of geothermal fluid after it passes through the binary power plant is desired. In such case, no need for providing injection temperatures to the model

4.5 Injection Well Model

The simple steady state injection well model includes the flow of the geothermal fluid from the binary power plant back into the reservoir through the injection well. The injection well model is based on the same equations used in the production well model. However, the equations are solved to accommodate for:

- Change of mass rate: from production rate to injection rate.
- Change of geothermal fluid movement direction: as it is the opposite of that in the production well model.

Geothermal fluid properties are computed at $(P_{out} = P_{Wh(PW)}, T_{ri})$.

4.5.1 Preliminary Calculations

Number of injection wells n_{ri} is calculated using Eq. 4.53.

$$n_{ri_j} = \frac{\dot{m}_{ri_j} - \text{Remainder}\left(\frac{\dot{m}_{ri_j}}{100}\right)}{100} \quad 4.53$$

The injection rate from a single injection well $\dot{m}_{ri(IW)}$ is calculated using Eq. 4.54.

$$\dot{m}_{ri(IW)_j} = \frac{\dot{m}_{ri_j}}{n_{ri_j}} \quad 4.54$$

4.5.2 Liquid Steady State Model for the Flow in the Injection Well

This model includes the calculation of geothermal fluid state at the rest of the cycle (back into the reservoir through the injection well).

The flow velocity of the geothermal fluid in the injection well v_{IW} (m/s) is calculated using Eq. 4.55.

$$v_{IW_j} = \frac{\dot{m}_{ri(IW)_j}}{A_f \rho_{w_{j-1}}} \quad 4.55$$

4.5.2.1 Temperature Behavior

For a fluid flowing down through the injection well, its temperature at elevation $L = 0$ from the wellhead, bottom hole injection temperature $T_{W(IW)}$ is determined using Eq. 4.56 for steady state conditions (Guo et al, 2013). The reader is referred to Appendix F for the detailed derivation.

$$T_{W(IW)_j} = \frac{1}{\alpha_c^2}_{j-1} (\beta_c - \alpha_c \gamma_c - e^{-\alpha_c(c_{inj})}) \quad 4.56$$

Where constants α_c , β_c , γ_c , and C_{prod} are defined in Eq. 4.57, Eq. 4.58, Eq. 4.59, and Eq. 4.60, respectively.

$$\alpha_{c j-1} = \frac{2\pi r_n \lambda_n}{s A_f} \frac{1}{v_{IWj} \rho_{w j-1} C_{pw j-1}} \quad 4.57$$

$$\beta_{c j-1} = \alpha_{c j-1} G \cos(\theta) \quad 4.58$$

$$\gamma_{c j-1} = -\alpha_{c j-1} T_{f,0 j-1} = -\alpha_{c j-1} T_{r j-1} \quad 4.59$$

$$C_{inj j-1} = -L_W - \frac{1}{\alpha_{c j-1}} \ln \left(\beta_{c j-1} - \alpha_{c j-1}^2 T_{Wh(IW)_j} - \alpha_{c j-1} \beta_{c j-1} L_W - \alpha_{c j-1} \gamma_{c j-1} \right) \quad 4.60$$

Please note that $T_{Wh(IW)_j} = T_{ri j}$.

4.5.2.2 Pressure Behavior

The injection pump must supply the geothermal fluid with additional to increase bottomhole pressure more than the reservoir pressure, so the injected fluid enters the reservoir. Pressure supplied by the injection pump is calculated using Eq. 4.61. Eq. 4.61 calculates the difference between reservoir pressure and the pressure of the geothermal fluid when it reaches the reservoir (after it flows through the injection well from the well head with $P_{Wh(PW)}$ pressure to the bottom hole with pressure of $(P_{Wh(PW)} - cf (C_{2 j-1} \dot{m}_{ri(IW)_j}^2 - \rho_{w j-1} g) L_W)$, back to the reservoir from the bottom hole to the reservoir through porous media $\left(P_{r j-1} - (P_{Wh(PW)} - cf (C_{2 j-1} \dot{m}_{ri(IW)_j}^2 - \rho_{w j-1} g) L_W - C_{D j-1} \dot{m}_{ri(IW)_j}) \right)$. The 10 bars pressure addition is an arbitrary safety margin so that the injected geothermal fluid reaches the reservoir having a pressure 10 bars higher than that of the reservoir. The reader is referred to Appendix E and G for the detailed derivation.

$$\Delta P_{IPj} = P_{rj-1} - \left(P_{Wh(PW)_j} - cf \left(C_{2j-1} \dot{m}_{ri(IW)_j}^2 - \rho_{wj-1} g \right) L_W - C_{Dj-1} \dot{m}_{ri(IW)_j} \right) + 10 \text{ bars} \quad 4.61$$

Where cf is equal to 1E-05 (conversion from Pa to bar), C_2 and C_D has been defined earlier in the production well model, Eq. 4.47 and Eq. 4.34, respectively. Note that the only difference between the values of C_2 and C_D in the production well model and C_2 and C_D values in the injection well model is due to the difference in the thermodynamic state at which geothermal fluid properties are computed.

IP requirement W_{IP} is calculated using Eq. 4.62.

$$W_{IPj} = \frac{cf}{\eta_{IP}} \Delta P_{IPj} \frac{\dot{m}_{ri(IW)_j}}{\rho_{wj-1}} \quad 4.62$$

Well head injection pressure $P_{Wh(IW)}$ is calculated using Eq. 4.63.

$$P_{Wh(IW)_j} = P_{Wh(PW)_j} + \Delta P_{IPj} \quad 4.63$$

Bottom hole injection pressure $P_{W(IW)}$ is calculated using Eq. 4.64.

$$P_{W(IW)_j} = P_{Wh(IW)_j} - cf \left(C_{2j-1} \dot{m}_{ri(IW)_j}^2 - \rho_{wj-1} g \right) L_W \quad 4.64$$

Reservoir pressure from injection $P_{r(IW)}$ is calculated using Eq. 4.65.

$$P_{r(IW)_j} = P_{W(IW)_j} - C_{Dj-1} \dot{m}_{ri(IW)_j} = P_{rj-1} + 10 \text{ bars} \quad 4.65$$

4.6 Postliminary Calculations

Cumulative; produced pore volume PV_p (fraction), injected pore volume PV_{ri} , recharged pore volume PV_{re} , or net produced pore volume PV_{pn} as a fraction of the initial reservoir pore volume PV_i is calculated using Eq. 4.66.

$$PV_{pj} = PV_{pj-1} + \frac{M_{pj}}{PV_i} \quad 4.66$$

Where M_p is the produced mass (kg) calculated using Eq. 4.67. Subscript "p" is replaced with; "ri" for the cumulative injected PV, "re" for the cumulative recharged PV, and "pn" for the net produced PV. Note that $PV_{p_0} = PV_{ri_0} = PV_{re_0} = PV_{pn_0} = 0$.

$$M_{p_j} = \dot{m}_{p_j} \Delta t \quad 4.67$$

Subscript "p" is replaced with; "ri" for the injected mass, and "pn" for the net produced mass. The recharged mass M_{re} is calculated using Eq. 4.68, as it can vary during Δt (the reader is referred to Appendix H for the detailed derivation).

$$M_{re_j} = \alpha \left(\Delta P_{r_{j-1}} \Delta t - \left(\Delta P_{r_{j-1}} - \frac{\dot{m}_{pn_j}}{\alpha} \right) \left(\Delta t - \frac{1}{D_{j-1}} (1 - e^{-D_{j-1} \Delta t}) \right) \right) \quad 4.68$$

Cumulative; Produced heat H_p , injected heat H_{ri} , recharged heat H_{re} , or net conductive heat H_{Qn} as a fraction of the initial heat content of the reservoir HC_i are calculated using Eq. 4.69, Eq. 4.70, Eq. 4.71, and Eq. 4.72, respectively.

$$H_{p_j} = H_{p_{j-1}} + \frac{M_{p_j} C_{pw_{j-1}} T_{r_{j-1}}}{HC_i} \quad 4.69$$

$$H_{ri_j} = H_{ri_{j-1}} + \frac{M_{ri_j} C_{pw_{ri_j}} T_{ri_j}}{HC_i} \quad 4.70$$

$$H_{re_j} = H_{re_{j-1}} + \frac{M_{re_j} C_{pw_{re}} T_{re}}{HC_i} \quad 4.71$$

$$H_{Qn_j} = H_{Q_{j-1}} + \frac{Q_{n_j} \Delta t}{HC_i} \quad 4.72$$

Note that $H_{p_0} = H_{ri_0} = H_{re_0} = H_{Q_0} = 0$. Subscript Qn in Eq. 4.72 is replaced by Q_{top} and Q_{bottom} for the calculation of cumulative conductive heat from the overlying layer and underlying layer, respectively.

The cumulative total heat gained by the reservoir H_G is calculated using Eq. 4.73.

$$H_{G_j} = H_{ri_j} + H_{re_j} + H_{Q_j} \quad 4.73$$

The running capacity calculated earlier (Eq. 4.52) is not the actual running capacity of the power plant as there is a DHP for each production well and an IP for each injection well, consuming energy. Total requirement of pumps W_{pumps} is calculated using Eq. 4.74.

$$W_{pumps_j} = n_{p_j} W_{DHP_j} + n_{ri_j} W_{IP_j} \quad 4.74$$

The net (actual) running capacity of the binary power plant W_n is calculated using Eq. 4.75.

$$W_{n_j} = W_j - W_{pumps_j} \quad 4.75$$

Electricity produced E (MWh) is calculated using trapezoidal approximation, Eq. 4.76.

$$E_j = E_{j-1} + cf \left(\frac{W_{n_j} + W_{n_{j-1}}}{2} \right) \Delta t \quad 4.76$$

Where cf is equal to 1/3600 (conversion from sec to hour). Note that $E_0 = 0$.

CHAPTER 5

RESULTS AND DISCUSSION

In this chapter, the results obtained from the developed LPM model for four production/injection scenarios are discussed and compared. First, model inputs are discussed, followed by the discussion of each case, and their comparison, respectively.

5.1 Inputs

Model inputs are shown in Table 5.1, for a hypothetical low temperature reservoir utilized by a binary power plant through the circulation of geothermal fluid by production/injection wells.

Table 5.1. Model input parameters.

Parameter	value	Unit	Reference/note
Reservoir Properties			
T_{ri}	190	°C	Low temperature reservoir (Sanyal, 2005)
ρ_m	2650	Kg/m ³	Onur et al. (2008)
c_r	1.33E-04	1/bar	Onur et al. (2008)
C_{pm}	1000.0	J/(kg °C)	Onur et al. (2008)
ϕ_i	0.2	fraction	Onur et al. (2008)
k_R	70.0	mD	DiPippo (2008)
L_R	1000.0	m	Gudmundsson & Olsen (1987), Tureyen & Akyapi (2011)
r_R	1954.4	m	Adjusted based on reservoir volume V_R
λ_R	3.06	W/(m C°)	Thermal conductivity of sandstone (Tang et al., 2019)
Aquifer Properties			
k_A	10	mD	Adjusted based on recharge index α
r_A	7000	m	Adjusted based on recharge index α
T_{re}	190	°C	Equal to T_{ri}
Confining layers properties			
$\lambda_{top/bottom}$	2.48	W/(m C°)	Thermal conductivity of shale (Tang et al., 2019)
$L_{top/bottom}$	400	m	Based on the depth of the confining layers constant temperatures $T_{top/bottom}$
Well properties			
r_W	0.091	m	Firanda et al. (2021)
h_{comp}	100	m	Arbitrary
r_n	0.1	m	Arbitrary
s	0.044	m	Wu et al. (2020)
λ_n	0.3	W/(m C°)	Thermal conductivity of cement (Wu et al., 2020)
L_W	2600	m	Based on geothermal gradient G
ε	0.01	mm	DiPippo (2008)
Others			
c_w	5.92E-05	1/bar	Onur et al. (2008)
T_s	25	°C	Arbitrary
η_{DHP}	0.9	fraction	Arbitrary
η_{IP}	0.9	fraction	Arbitrary

5.1.1 Preliminary Outputs

Based on the model inputs provided in Table 5.1, parameters shown in Table 5.2 are calculated

Table 5.2. Preliminary outputs obtained from the input.

Parameter	value	Unit	Reference/note
Reservoir Properties			
P_{r_i}	255	bar	Satman (2010)
A_R	1.2E+07	m ²	
V_R	1.2E+10	m ³	
PV_i	2.14E+12	kg	
HC_i	6.60E+18	J	
Aquifer Properties			
α	29.38	kg/(bar.s)	Satman (2010), Tureyen & Akyapı (2011)
C_{pwre}	4339.16	J/(kg °C)	
Confining layers properties			
* $d_{top/bottom}$	700	m	
$\lambda_{A_{top/bottom}}$	2.87	W/(m C°)	
$\gamma_{top/botton}$	4.92E+04	W/°C	
T_{top}	174.3	°C	
T_{bottom}	205.7	°C	
Well properties			
A_f	0.026	m ²	
Others			
c_t	1.92E-04	1/bar	
G	0.079	°C/m	
ρ_{w_i}	892.27	kg/m ³	At initial reservoir pressure and temperature
C_{pw_i}	4339.16	J/(kg °C)	At initial reservoir pressure and temperature
μ_{w_i}	1.48E-09	bar.s	At initial reservoir pressure and temperature

The temperature profile at the natural state of this low temperature geothermal hydrothermal system is shown in Figure 5.1. At this state, system is in the thermal equilibrium, i.e., conductive heat flux entering the reservoir from bottom is equal to conductive heat flux exiting the reservoir from top.

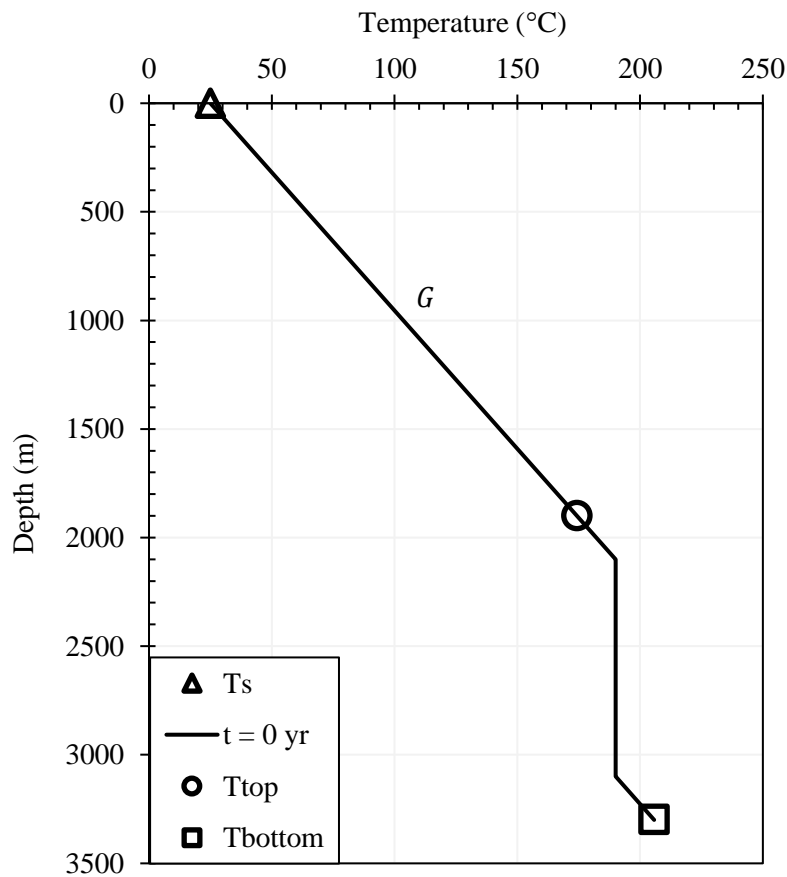


Figure 5.1. Temperature profile from the surface to the center of the underlying layer at the natural state.

5.2 Investigated Cases

Five production/injection scenarios have been investigated in this study. A simple production/injection scenario was used in the 1st case to highlight the details and the relations between the parameters. In the rest of the cases, however, the main points are highlighted only.

Note that in the first four cases (Case 1, 2, 3, and 4), the recharge temperature is set to be equal to the initial reservoir temperature. Thus, for these cases, the aquifer is connected to the reservoir through faults at reservoir extent (r_R) as shown in Figure 5.2, rather than being concentric with the reservoir as shown previously in Figure 4.1, which corresponds to Case 4b as recharge temperature is set to be different from initial reservoir temperature.

Figure 5.2. Illustration; of the LPM developed in this study for low temperature geothermal system, and the developed model for cases from 1 to 4. The numbers correspond to the geothermal fluid state (pressure, temperature) at different points.

5.2.1 Case 1

Case 1 is a simple production/injection scenario, where constant production rate of 500 kg/s and constant injection rate of 300 kg/s are maintained throughout 30 years of exploitation as shown in Figure 5.3. The figure also shows the production induced recharge rate and the injection temperature, which is the temperature of the geothermal fluid after its thermal energy has been utilized by the binary power plant T_{out} . It can be noted that the recharge rate coincides with the net production rate at the 2nd year approximately.

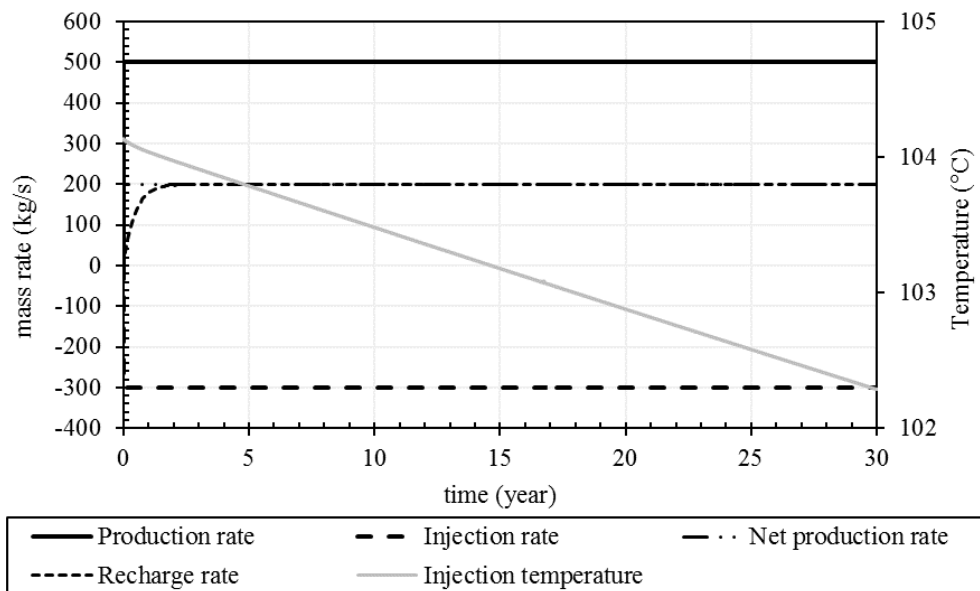


Figure 5.3. Production/injection scenario, net production rate, recharge rate, and injection temperature of Case 1.

Reservoir pressure P_r and temperature T_r behavior with time as a result of the production/injection scenario of this case are shown in Figure 5.4 and Figure 5.5, respectively. Reservoir pressure has reached to steady state around the second year, where the recharge rate has coincided with the net production rate. Reservoir temperature behavior is of a constant decreasing rate, where it decreased by 3 °C approximately from the beginning to the end of exploitation.

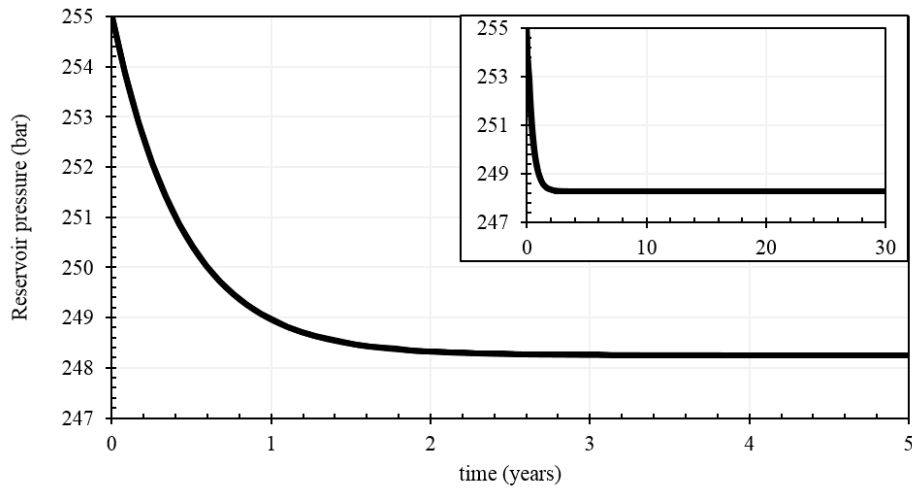


Figure 5.4. Reservoir pressure behavior with time in response to Case 1 shown for the first 5 years, and throughout the 30 years.

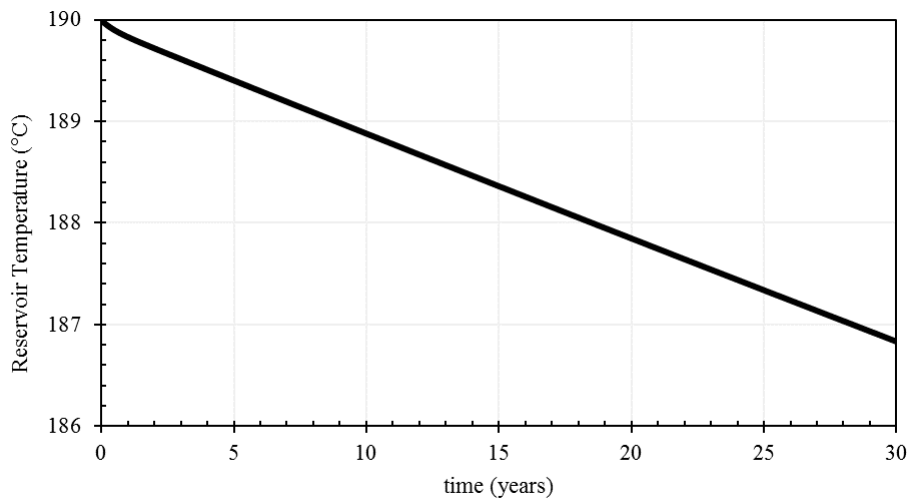


Figure 5.5. Reservoir temperature behavior with time in response to Case 1.

Cumulative; produced pore volume PV_p , injected pore volume PV_{ri} , recharged pore volume PV_{re} , and net produced pore volume PV_{pn} are shown in Figure 5.6. The cumulative injected PV at year 30 equals 60% of the cumulative produced PV for the same year, which coincide with the injection rate over production rate ratio of this case.

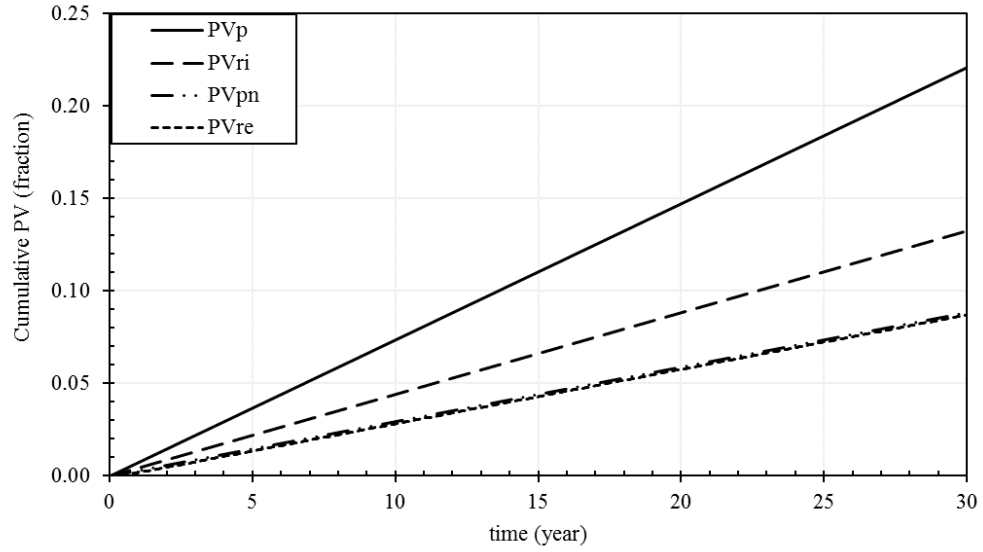


Figure 5.6. Cumulative pore volume produced, injected, recharged, and net produced through exploitation for Case 1.

Figure 5.7 shows the cumulative; produced heat H_p , injected heat H_{ri} , recharged heat H_{re} , net conductive heat H_{Qn} , and total heat gained by the reservoir H_G . At year 30, the cumulative total heat gained equals approximately 70% of the cumulative heat produced. Thus, 30% of the reservoirs heat has not been replenished. This is due to the lower injection temperature, injection rate, and recharge rate relative to production. Moreover, the cumulative net conductive heat ratio is approximately zero at the end of exploitation. The next set of figures investigate the behavior of the conductive heat.

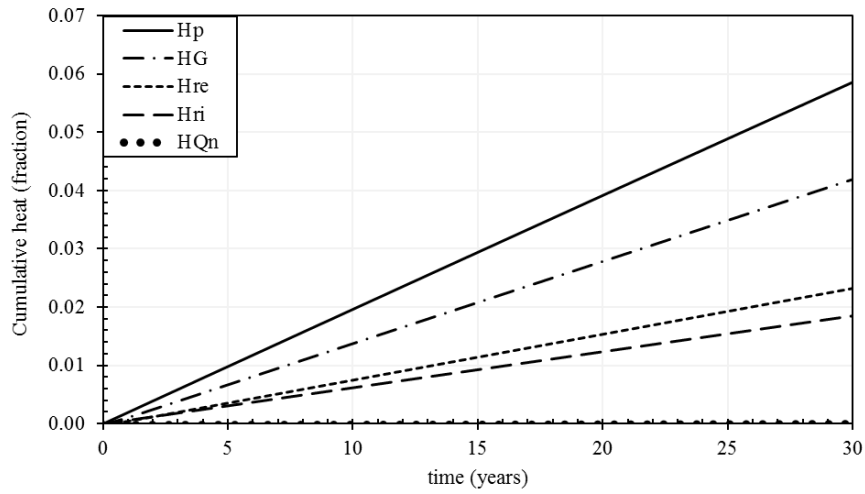


Figure 5.7. Cumulative heat produced, heat injected, heat recharged, and net conductive heat as a fraction of the initial reservoir heat content.

Figure 5.8 shows; the behavior of the conductive heat flow from the underlying shale layer Q_{bottom} , the conductive heat loss from the reservoir to the overlying shale layer Q_{top} , and their net Q_n . It can be noted that Q_n equals zero at the natural state ($t = 0$), and its increasing in time same as Q_{bottom} . While Q_{top} is decreasing with time. This can be seen more clearly in Figure 5.9, which shows the cumulative conductive heat from the underlying layer $H_{Q_{bottom}}$, cumulative conductive heat to the overlying layer $H_{Q_{top}}$, and net conductive heat H_{Q_n} . The increase of $H_{Q_{bottom}}$ and the decrease of $H_{Q_{top}}$ with time is due to exploitation which is causing reservoir temperature to decrease with time. The divergence of $H_{Q_{bottom}}$ and $H_{Q_{top}}$ can be noted at the 5th year approximately, where H_{Q_n} growth is higher than the preceding 5 year period.

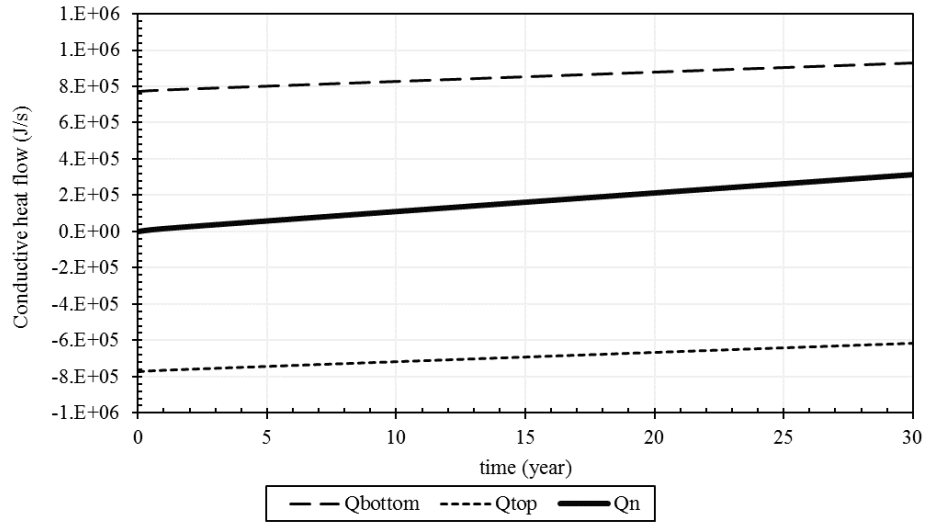


Figure 5.8. Conductive heat flow; from the underlying layer, to the overlying layer, and net conduction through time.

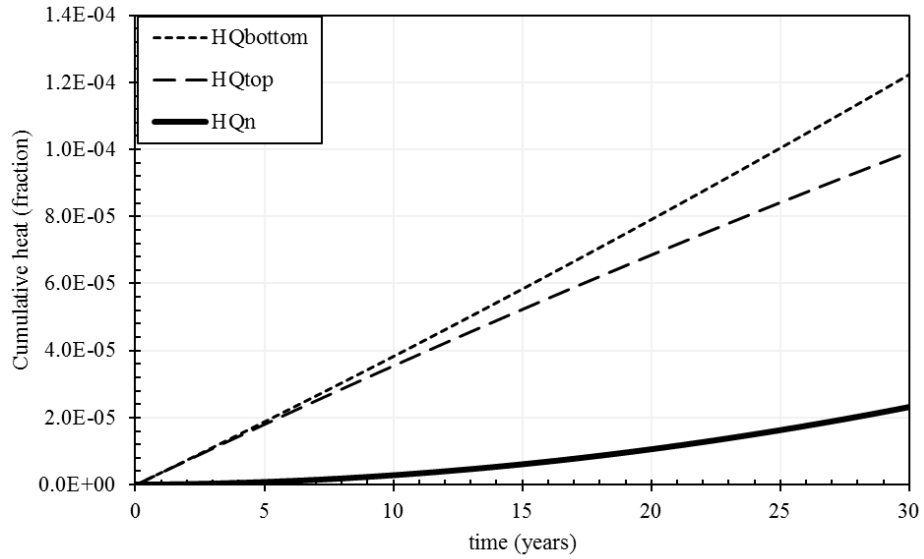


Figure 5.9. Cumulative conductive heat; gained from the underlying layer, lost to the overlying layer, and net conduction during the 30 years.

For this case, as the production flow rate from the reservoir and injection flow rate into the reservoir are constant, production rate from a single production well $\dot{m}_{p(PW)}$, injection rate from a single injection well $\dot{m}_{ri(IW)}$, number of production wells n_p , and number of injection wells n_{ri} , are also constants as shown in Figure 5.10. Five

Production wells and three injection wells are in operation where each well has a mass rate of 100 kg/s.

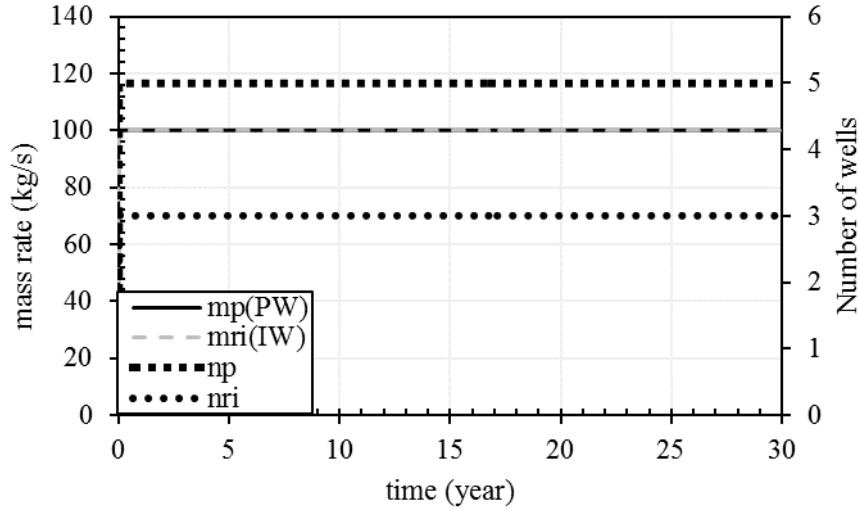


Figure 5.10. Number of injection wells and production wells, Production rate of a single production well, and injection rate of a single injection well throughout exploitation time.

As a side note, all the following figures related to production wells and injection wells are presented for a single production well and a single injection well. The rest of the production wells and injection wells follow the same pattern presented since they have the same properties.

Figure 5.11 shows the change in bottomhole production pressure $P_{W(PW)}$ throughout exploitation, in which it exhibits the same pattern as reservoir pressure. $P_{W(PW)}$ significantly decreases until steady state. After steady state, the gentle decrease is attributed to the increase of geothermal fluid density through time as its temperature in the reservoir decreases (Figure 5.12). Note the slight decrease in fluid pressure at the first year due to the significant decrease in reservoir pressure before reaching steady state.

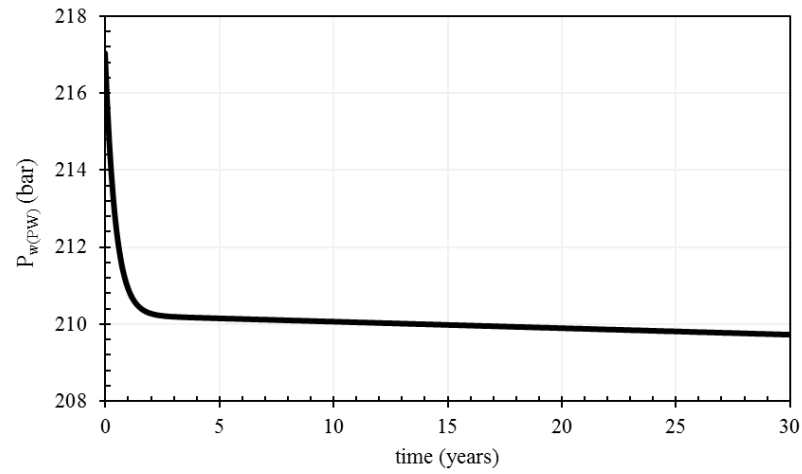


Figure 5.11. Bottom-hole production pressure throughout exploitation.

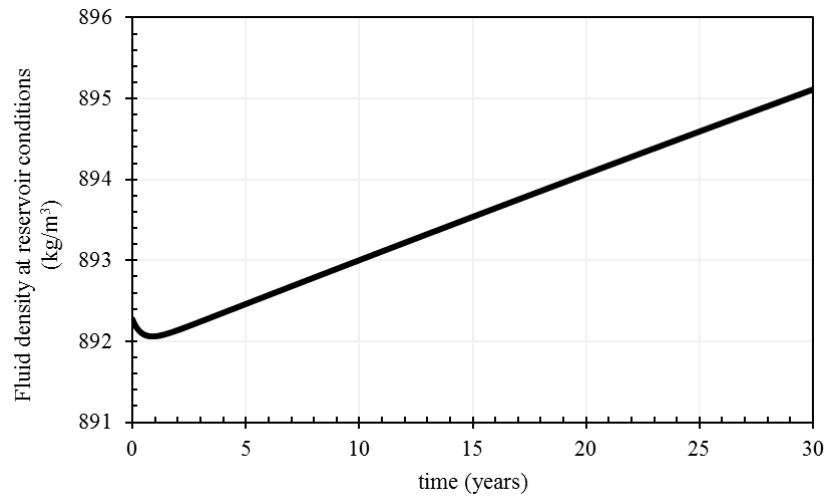


Figure 5.12. Fluid density change, computed at reservoir conditions through exploitation time.

Figure 5.13 shows the change in geothermal fluid pressure with radius as it flows from the reservoir to the bottomhole of the production well at the beginning, middle, and end of exploitation.

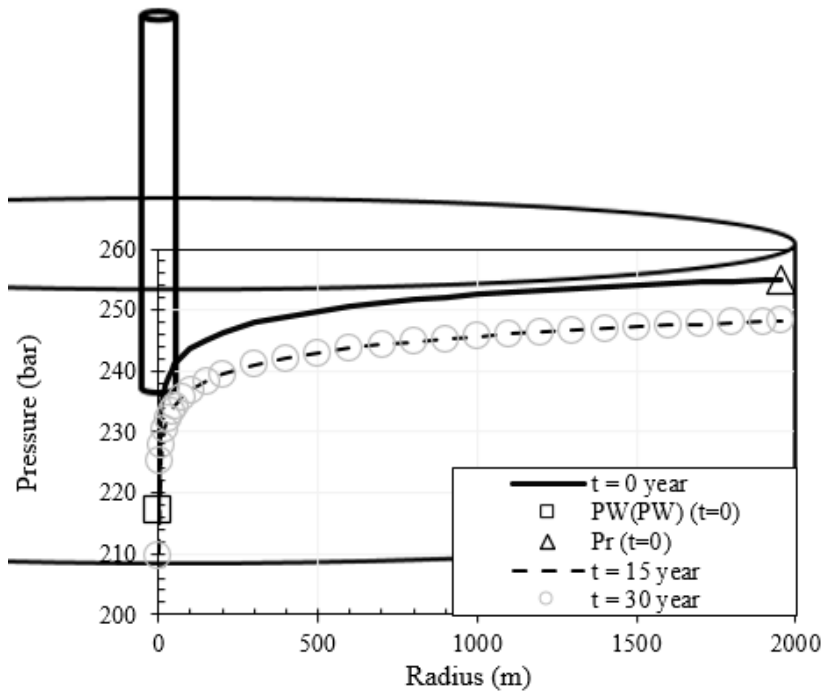


Figure 5.13. Change of geothermal fluid pressure while it flows through the porous media from the reservoir to the bottomhole of the production well at different instances.

Flash depth change with time is shown in Figure 5.14, where it decreases exponentially until steady state, following the reservoir pressure. After steady state, it gently decreases due to the decrease in saturation pressure with reservoir temperature $P_{sat}(T_r)$, as shown in Figure 5.15. The pressure supplied to the geothermal fluid by the downhole pump ΔP_{DHP} through time, mirrors the flash depth behavior as shown in the Figure 5.14.

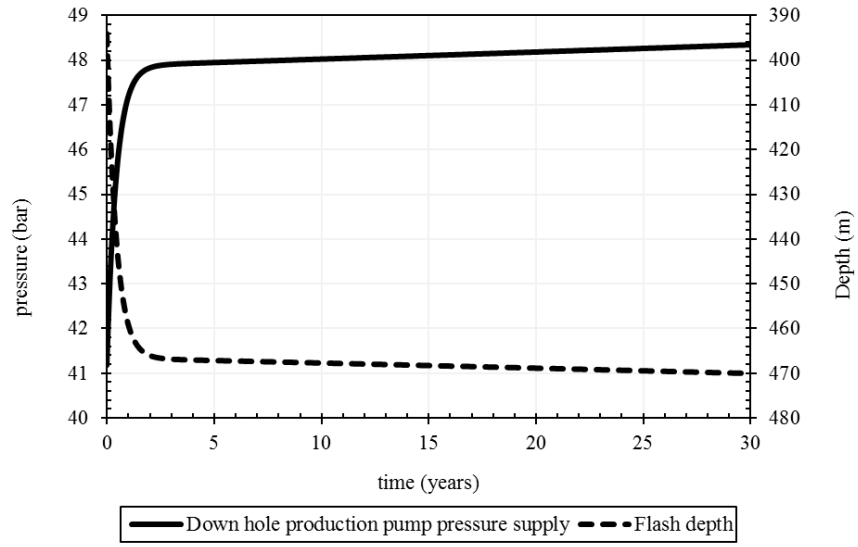


Figure 5.14. Downhole production pump and flash horizon depth behaviors with time.

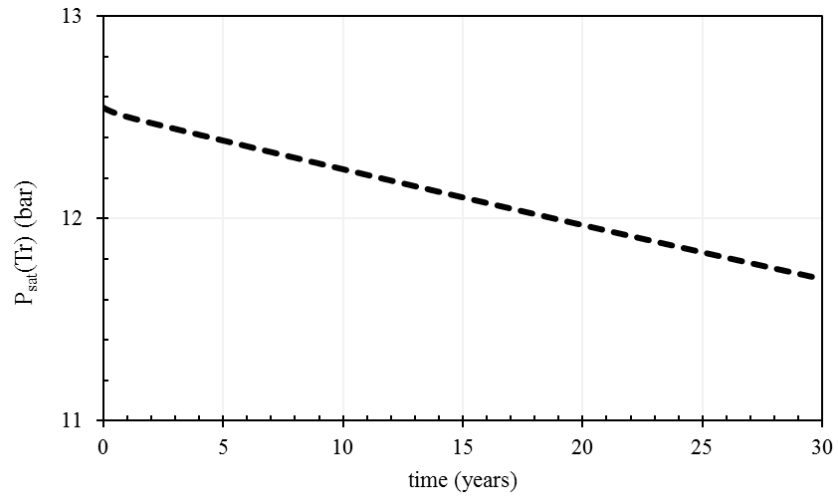


Figure 5.15. Change of geothermal fluid saturation pressure, computed at reservoir temperature, through exploitation.

The increase in fluid density with time also causes wellhead production pressure $P_{Wh(PW)}$ to decrease with time as shown in Figure 5.16.

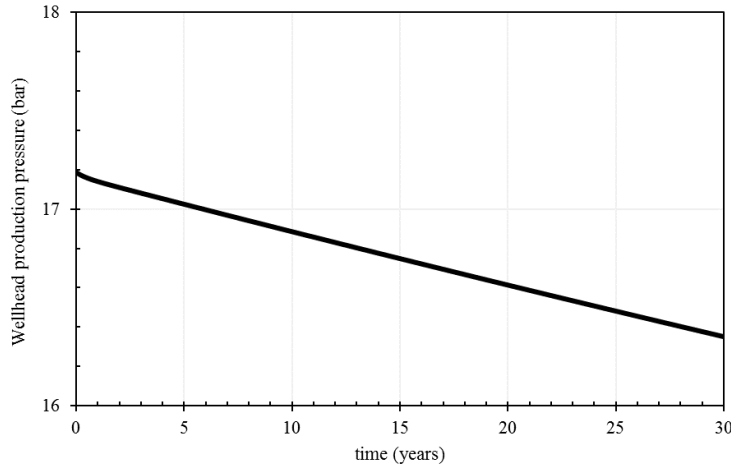


Figure 5.16. Wellhead production pressure behavior with time.

Figure 5.17 is a schematic of production well showing the flash depth L_f , geothermal fluid pressure change from the bottomhole $P_{W(PW)}$, to the wellhead $P_{Wh(PW)}$, at different instances. After the reservoir reaches steady state, geothermal fluid pressure in the production well does not differ almost since reservoir pressure has stabilized. This can be noted from the difference between geothermal fluid pressure before the reservoir reaches steady state ($t = 0$), and geothermal fluid pressure after the reservoir has reaches steady state at $t = 15$, and 30 years. The same can be noted for the flash depth which is equal to around 400 m once production commence. At the 15th year, it drops an additional 70 m approximately and stabilizes there. Downhole pump in such case must be placed below the highest flash depth during exploitation period, which is equal to 470 m at the 30th year according to Figure 5.14.

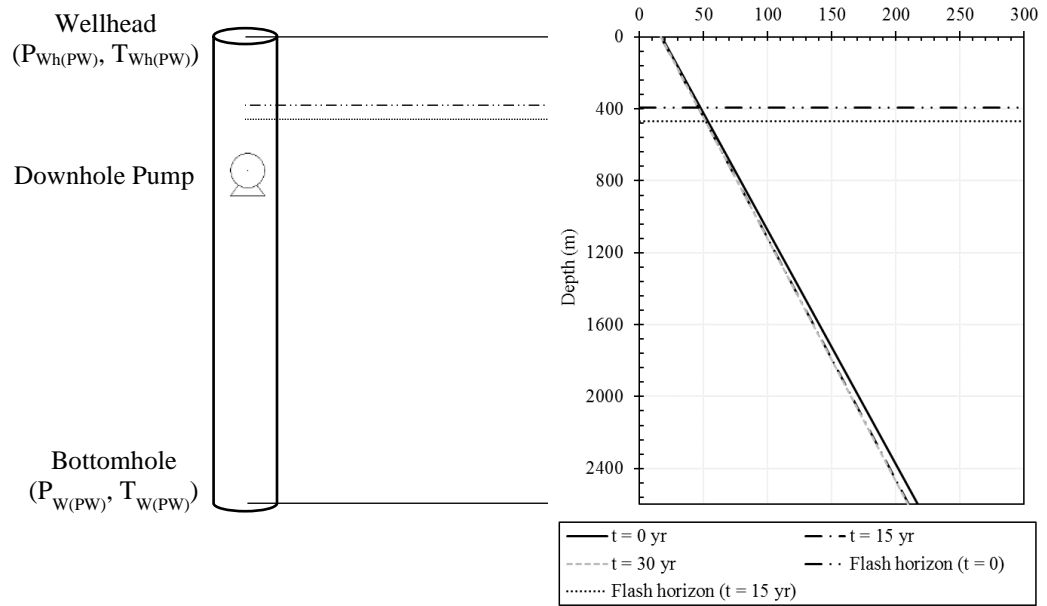


Figure 5.17. Production well schematic showing flash depth, pressure at the wellhead and pressure at the bottomhole, at the beginning, mid, and end of exploitation.

As the geothermal fluid travels up the production well, it losses some of its heat to the surrounding rock due to conduction as shown in Figure 5.18. Figure 5.19 shows that the decreasing slope of well head temperature $T_{Wh(PW)}$ with time is equal to that of geothermal fluid temperature at the reservoir. Thus, the heat loss from the geothermal fluid while traveling through the production well is constant and equal to 3°C approximately. This is due to the constant properties of the production well with depth (i.e., the cross-sectional flow area A_f).

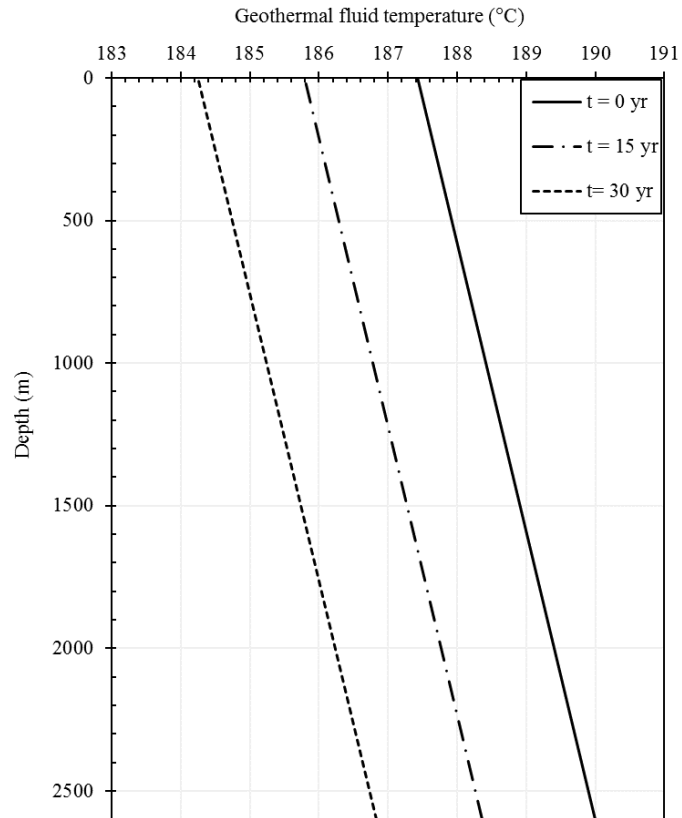


Figure 5.18. Geothermal fluid temperature change throughout the production well at beginning, middle and end of exploitation.

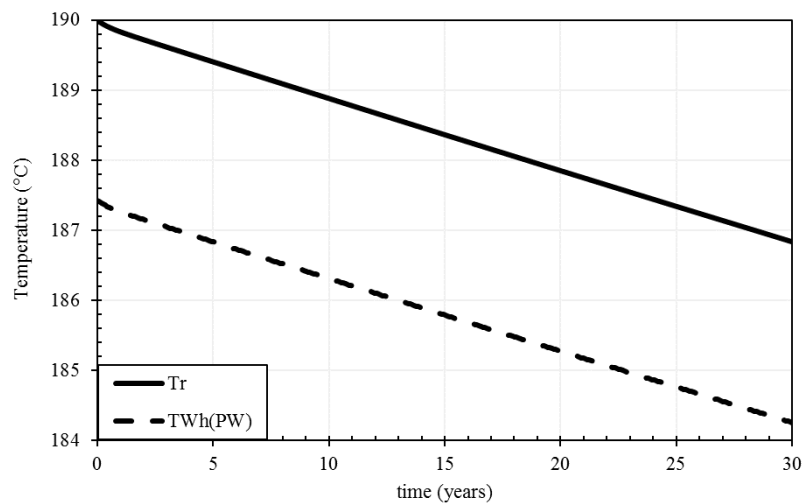


Figure 5.19. Geothermal fluid temperature at the wellhead production and at the reservoir throughout the exploitation.

The temperature of the geothermal fluid after its heat has been converted to electrical energy, or at the outlet of the binary power plant, T_{out} during exploitation is shown in Figure 5.20. The decrease of T_{out} through time is due to the decrease of well head temperature with time.

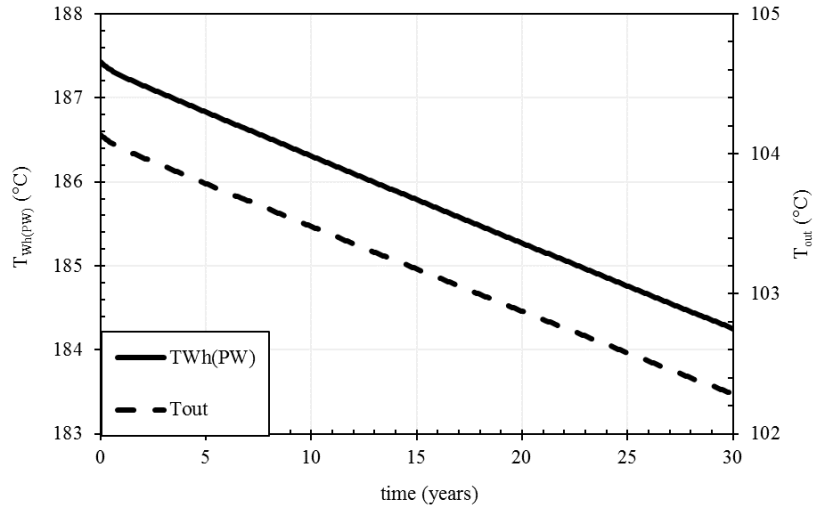


Figure 5.20. Geothermal fluid temperature before and after its heat is utilized by the binary power plant throughout exploitation.

Before steady state, the decrease in reservoir pressure causes the pressure supplied by the injection pump ΔP_{IP} to decrease as shown in Figure 5.21. After steady state, the gentle increase of ΔP_{IP} substitutes the following:

- The decrease of wellhead production pressure through exploitation time, and
- The increase in injected fluid density with time as shown in Figure 5.22 due to the decrease in its temperature with time T_{out} . Thus, higher pressure is needed for the injected fluid to flow through porous media from the bottomhole of the injection well to the reservoir.

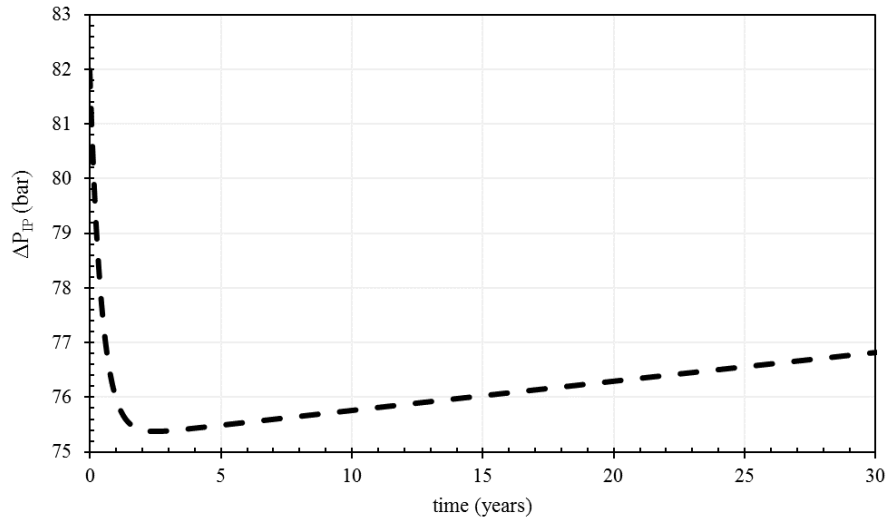


Figure 5.21. Wellhead injection pressure, and pressure supplied by the injection pump through exploitation time.

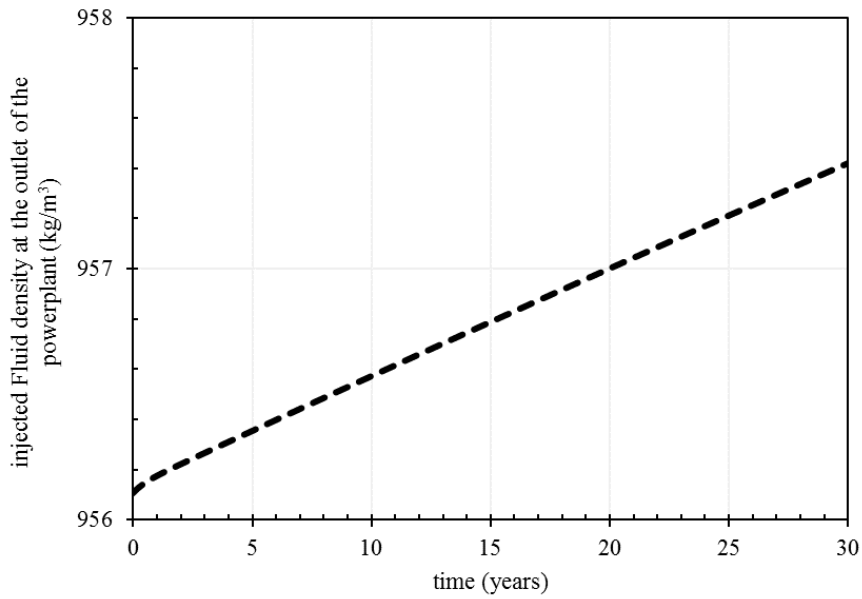


Figure 5.22. Change of geothermal fluid density, computed at the power plant outlet, through time.

The wellhead injection pressure $P_{Wh(IW)}$ follows the same pattern of ΔP_{IP} , Figure 5.23, as it's the addition of wellhead production pressure to the pressure supplied by the injection pump. Bottomhole injection pressure $P_{W(IW)}$ also follows the same

pattern, Figure 5.24, as the geothermal fluid travels from the wellhead to the bottomhole gaining pressure.

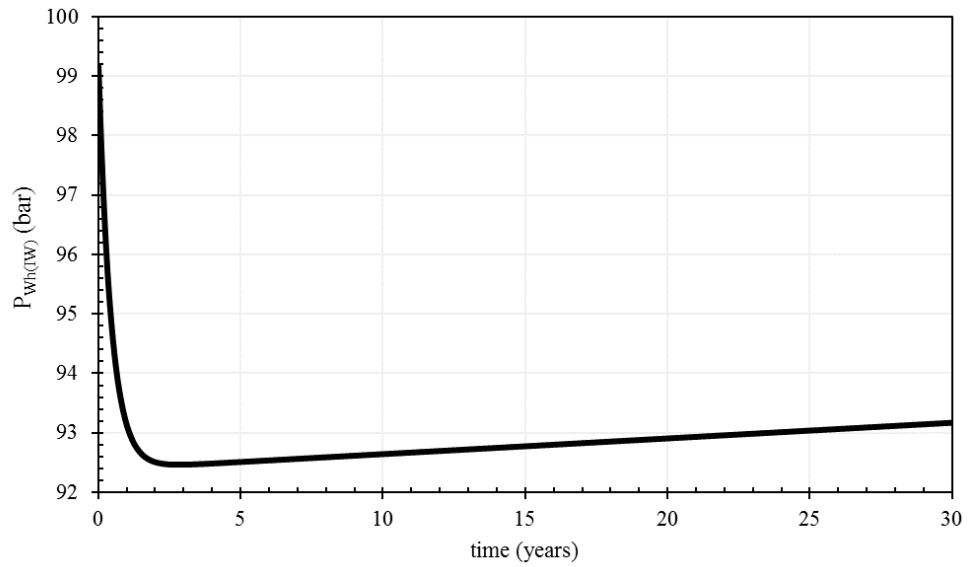


Figure 5.23. Behavior of wellhead injection pressure through exploitation.

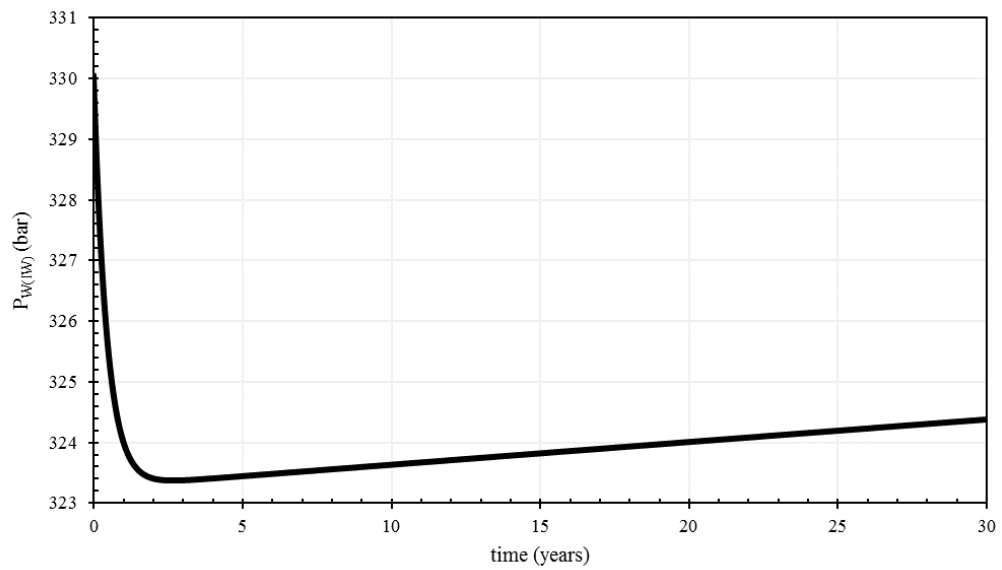


Figure 5.24. Behavior of bottomhole injection pressure through exploitation.

Reservoir pressure from injection $P_{r(IW)}$ behavior through exploitation is shown in Figure 5.25. At any time, $P_{r(IW)}$ is higher than reservoir pressure by 10 bars.

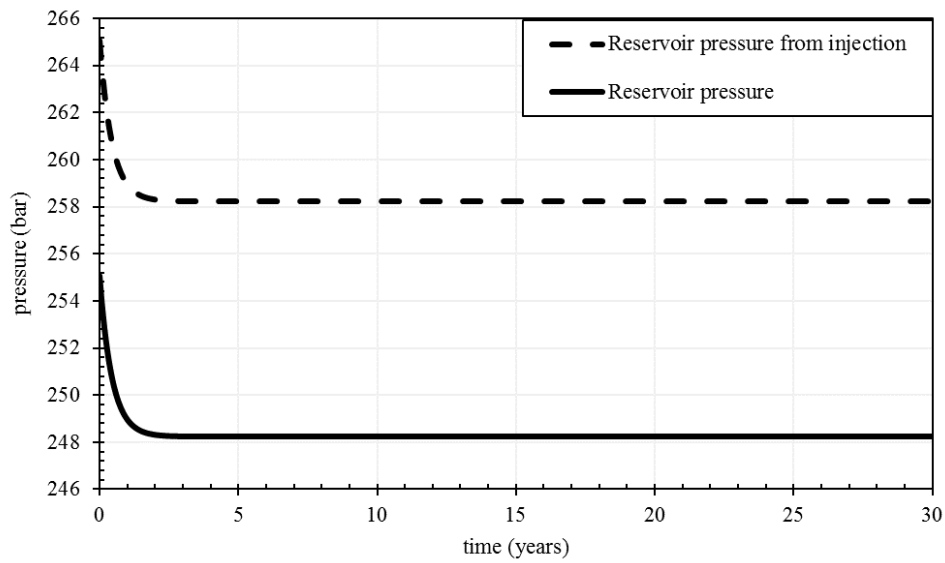


Figure 5.25. Reservoir pressure and injected fluid pressure after it has reached the reservoir (flow through porous media).

Figure 5.26 shows the change of geothermal fluid pressure with radius as it flows from the bottomhole of the injection well to the reservoir at the beginning, middle, and end of exploitation.

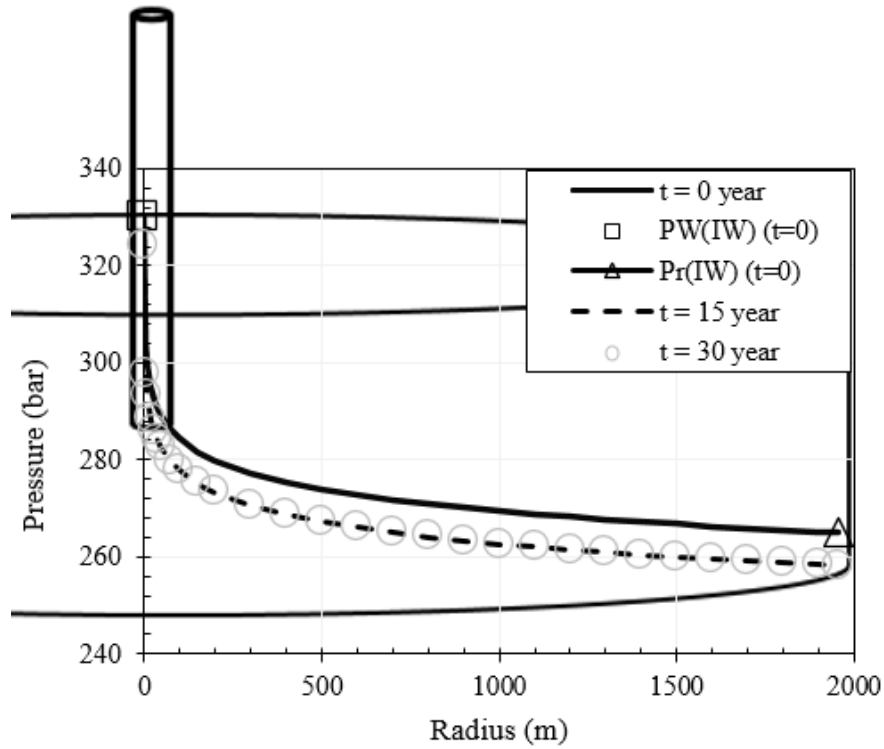


Figure 5.26. Geothermal fluid pressure behavior as it flows through the porous media from the bottomhole of the injection well to the reservoir at various instances.

As the geothermal fluid losses energy while it travels up the production well, it gains energy while it travels back into the reservoir from the surrounding rock. Figure 5.27 shows the change of geothermal fluid temperature at the wellhead of the injection well (equal to the geothermal fluid temperature at the outlet of the binary power plant T_{out}), and the change of geothermal fluid temperature at the bottomhole of the injection well $T_{W(IW)}$, during exploitation time. It can be noted that injected fluid temperature is increasing by 0.2 °C approximately at any time. Figure 5.28 shows the change of geothermal fluid temperature throughout the injection well at 3 different instances, beginning, mid, and end of exploitation.

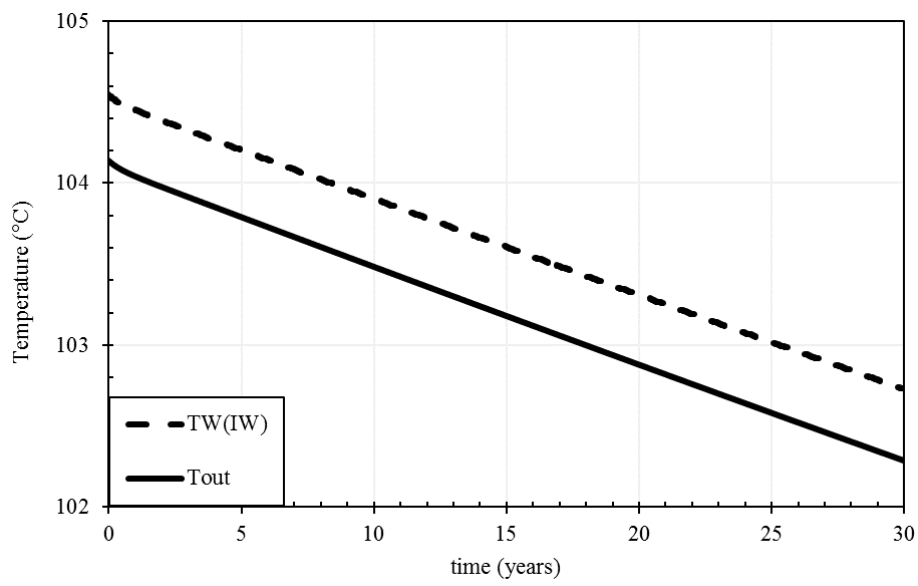


Figure 5.27. T_{out} and bottom hole injection temperature behavior with time.

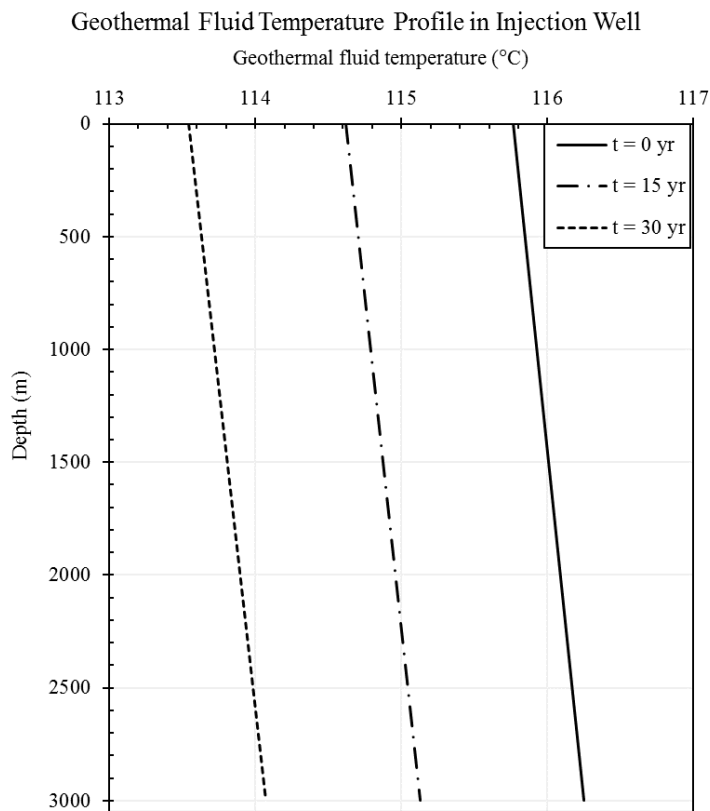


Figure 5.28. Geothermal fluid temperature change throughout the injection well at beginning, middle and end of exploitation.

Figure 5.29 shows DHP requirement W_{DHP} , IP requirement W_{IP} , binary power plant running capacity W , net running capacity W_n , and cumulative power generated $Power$, through exploitation time. W_{DHP} and W_{IP} are almost constant throughout the exploitation period. Given the 3 °C reservoir temperature drop from beginning to the end of exploitation, W decreases very gently, in which 1 MW drop approximately can be noted from the beginning of exploitation to its end. W_n follows the same pattern. The cumulative power generated by this case production/injection scenario is equal to 5.44E+06 MWh.

The installed capacity for this power plant utilizing such production/injection scenario can be 27 MW, as the running capacity is less than 27 MW at all times. Thus, the capacity factor for this power plant is equal to 77%.

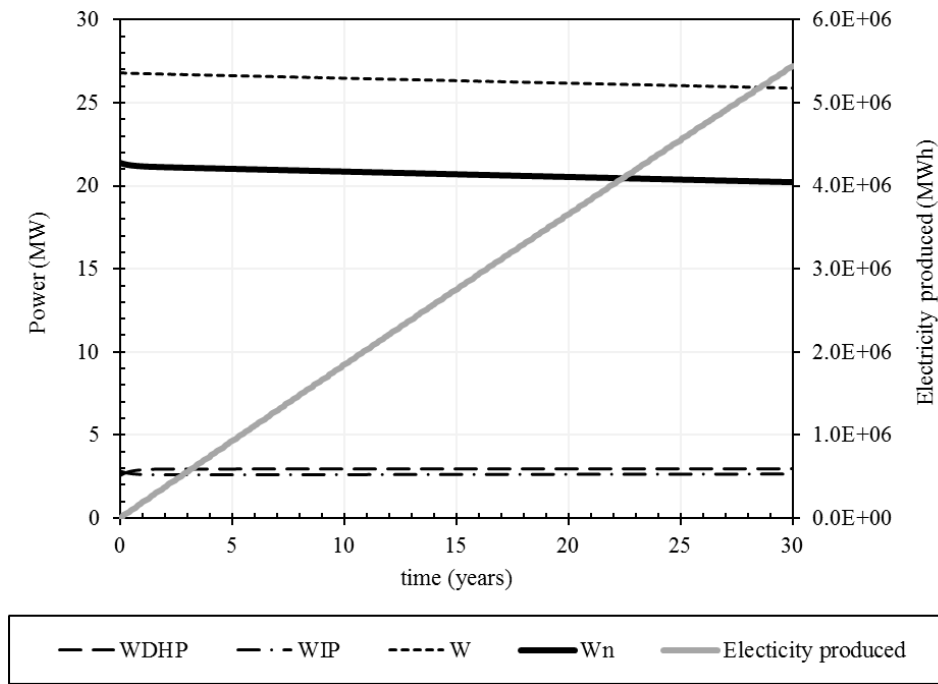


Figure 5.29. Power generated, work of pumps, running capacity and its net behaviors with time.

Figure 5.30 shows that the geothermal fluid is always in the liquid phase satisfying the condition for electricity generation from a binary power plant. Furthermore, the figure shows the geothermal fluid condition numbers shown previously in Figure

4.1, in the previous chapter. The U-shaped curve is being nearly displaced to the bottom left through time. This is due to the decreasing reservoir pressure and temperature.

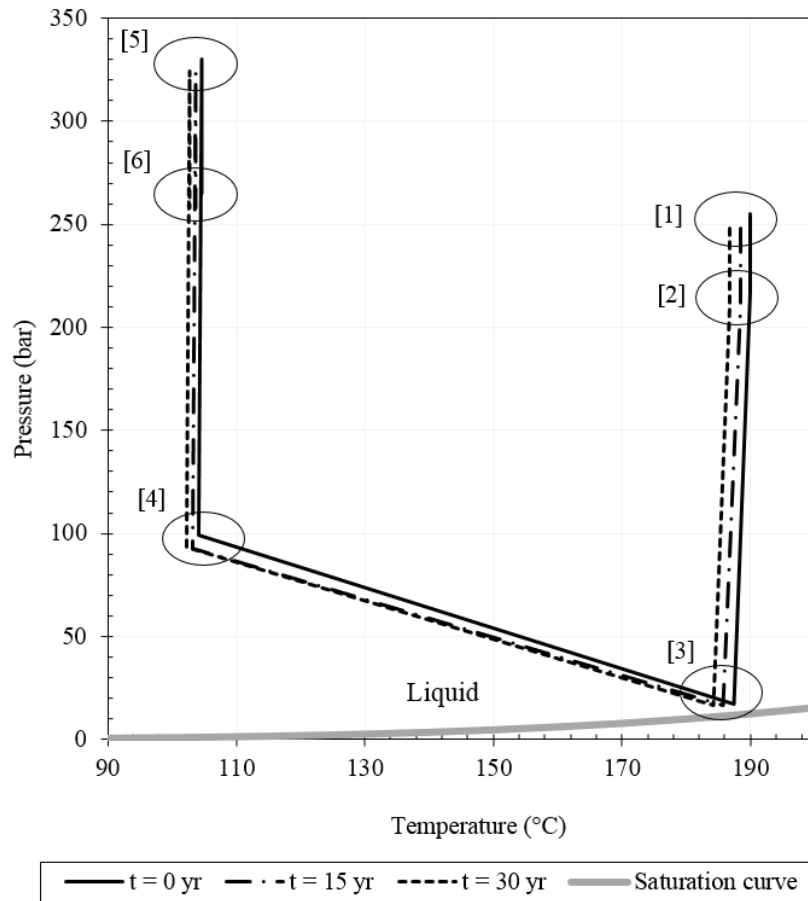


Figure 5.30. Phase diagram of water, and geothermal fluid at multiple conditions throughout its power generation cycle.

5.2.2 Case 2

The production/injection scenario of this case is composed of two production periods separated by a shut-in period, in which all the periods are 10 years long as shown in Figure 5.31. In the first production period, 500 kg/s are produced from the reservoir, and 90% of the production rate is injected back to the reservoir. The production rate

from the reservoir in the first production period is doubled in the second production period, and 10% of it is injected back into the reservoir. Injection temperature in both of the production periods correspond to the temperature of the geothermal fluid at the outlet of the power plant, same as Case 1. The corresponding net production rate and recharge rate throughout this scenario, are also shown in the figure.

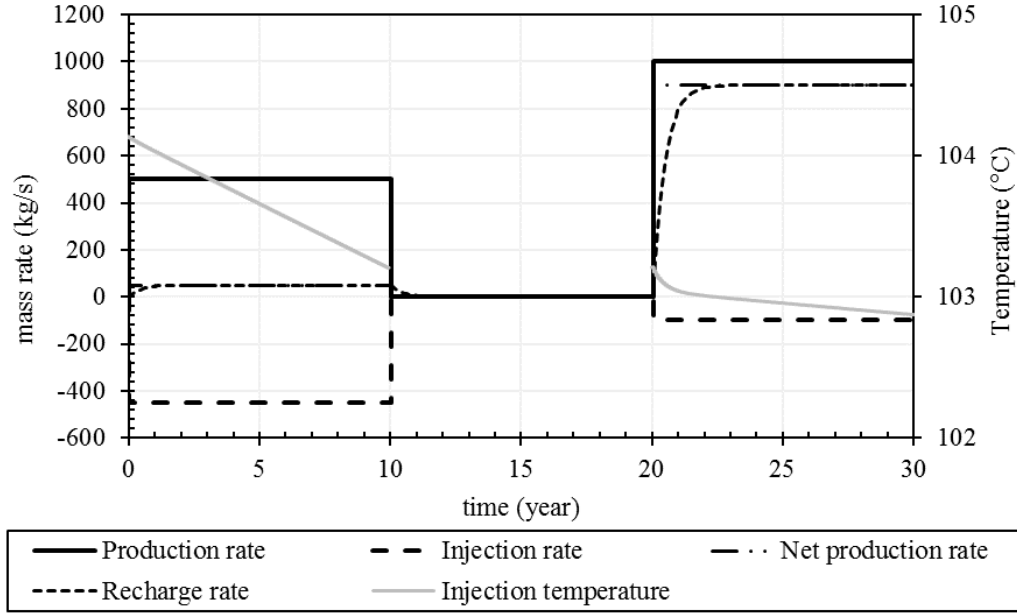


Figure 5.31. Production/injection scenario, production induced recharge, and injection temperature of Case 2.

Five production wells and four injection wells are utilized during the first production period. In the 2nd production period, the number of production wells utilized n_p is doubled and the number of injection wells utilized n_{ri} is reduced to one as shown in Figure 5.32, which also shows the production rate from single production well $\dot{m}_{p(PW)}$ and injection rate from single injection well $\dot{m}_{ri(IW)}$.

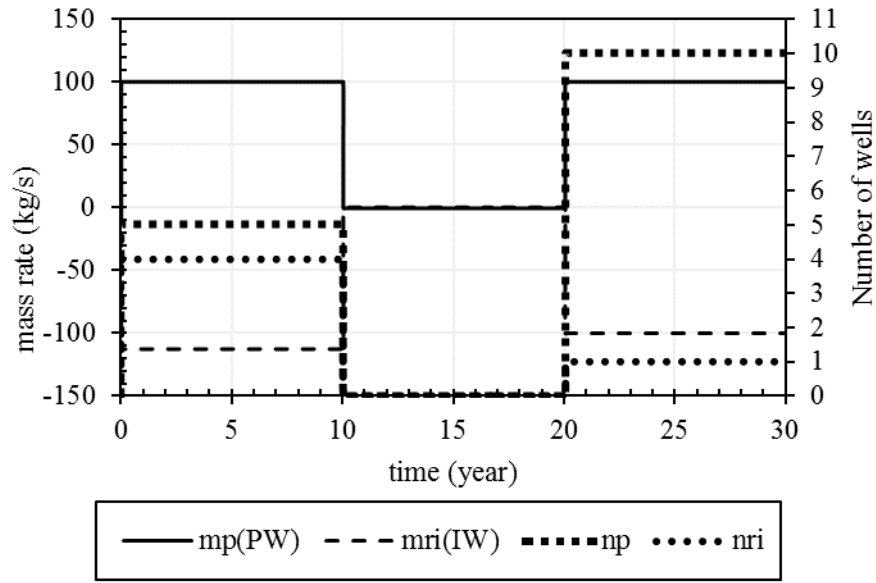


Figure 5.32. Case 2 utilized production and injection well count, and their single well production and injection rate.

Reservoir pressure behavior in response to this case scenario is shown in Figure 5.33. The high injection rate in the first production period maintains the reservoir pressure, where it drops few bars before reaching to steady state at the end of the 1st year approximately. After shutting-in the reservoir at the 10th year, reservoir pressure increases to its initial pressure due to recharge by almost the 11th year. The recharge rate between the 10th and 11th year in Figure 5.31, and Figure 5.34, confirm this. Given the low injection rate in the second production period, reservoir pressure drops significantly by almost 30 bars, where it reaches steady state at the 2nd year approximately of the second production period. The high reservoir drawdown in this period allows higher recharge rate to infiltrate into the reservoir as shown previously in Figure 5.31 and Figure 5.34, which shows the cumulative recharged pore volume PV_{re} . The growth rate (slope) of PV_{re} at the 2nd production period is steeper than that of the 1st production period.

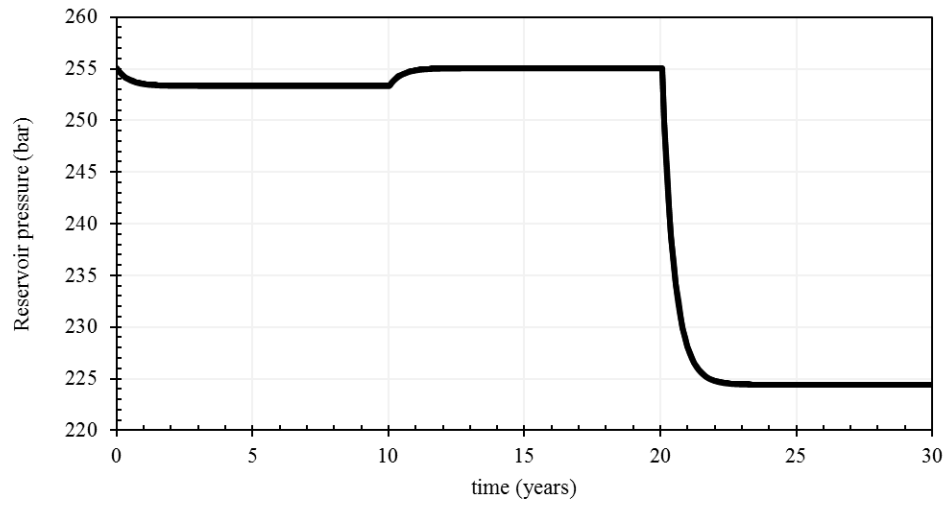


Figure 5.33. Response of reservoir pressure to Case 2 production/injection scenario

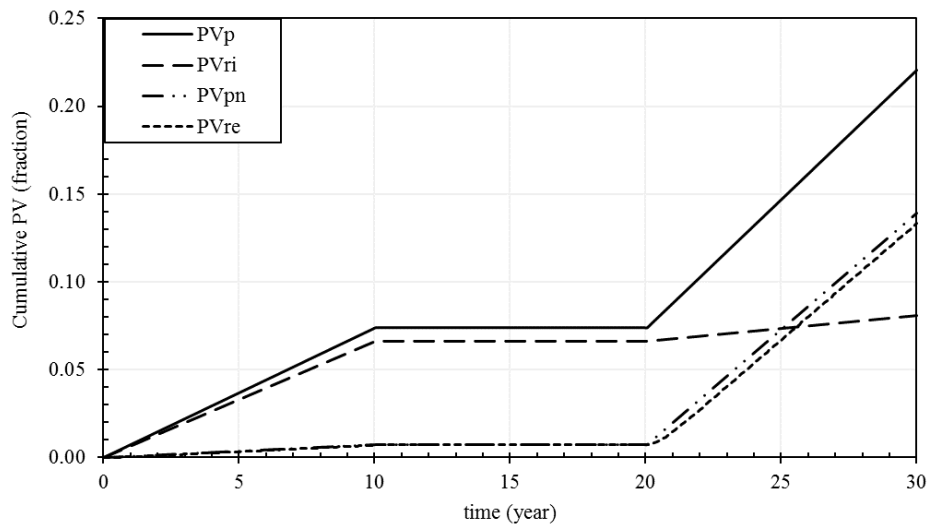


Figure 5.34. Case 2's cumulative; produced PV, injected PV, net produced PV, and recharged PV

Unlike the behavior of reservoir pressure in the 1st production period, reservoir temperature drop during the 1st production period is more significant relative to the second production period as shown in Figure 5.35. This is due to the limited recharge (limited convection) the reservoir receives in the 1st period. As a reminder, recharge temperature is constant, and equals to the initial reservoir temperature. During shut-in, reservoir temperature increase is very small to the point where it can be

considered negligible. This small increase is due to the small recharge amount that entered the reservoir during this period (between 10th and 11th year). The conductive heat transfer has not affected the reservoir temperature. This can be indicated from the net conductive heat H_{Qn} shown in Figure 5.36, where it's almost zero at all times.

Figure 5.36 also shows the cumulative total heat gained H_G . The high growth rate (slope) of H_G at the second production period explains the small decrease in reservoir temperature in this period relative to the first period. It can be noted that almost all the heat gained by the reservoir in the 2nd production period is due to the convective heat transfer from the recharge. The contribution of injection is almost negligible as the cumulative injected heat H_{ri} increases very gently between year 20 and 30, given the small injection rate at this period.

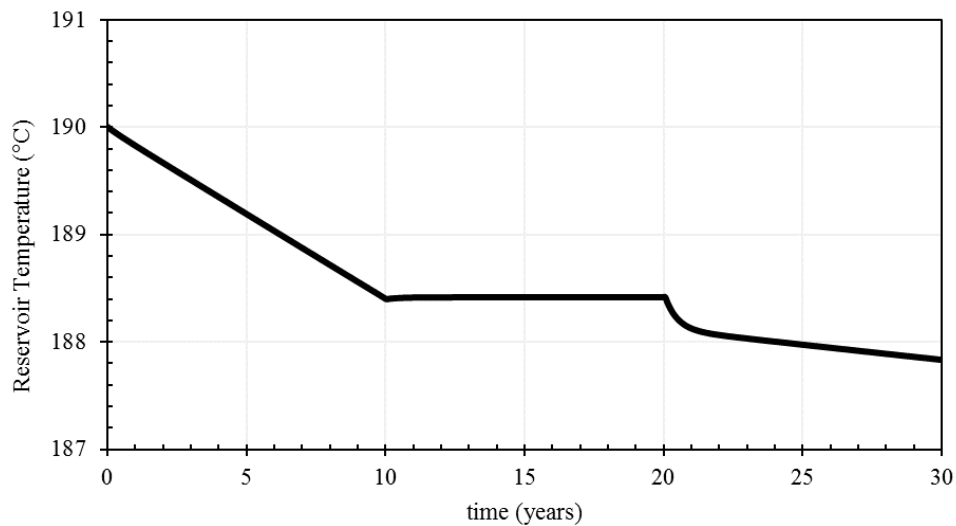


Figure 5.35. Change of reservoir temperature in response to Case 2 production/injection scenario

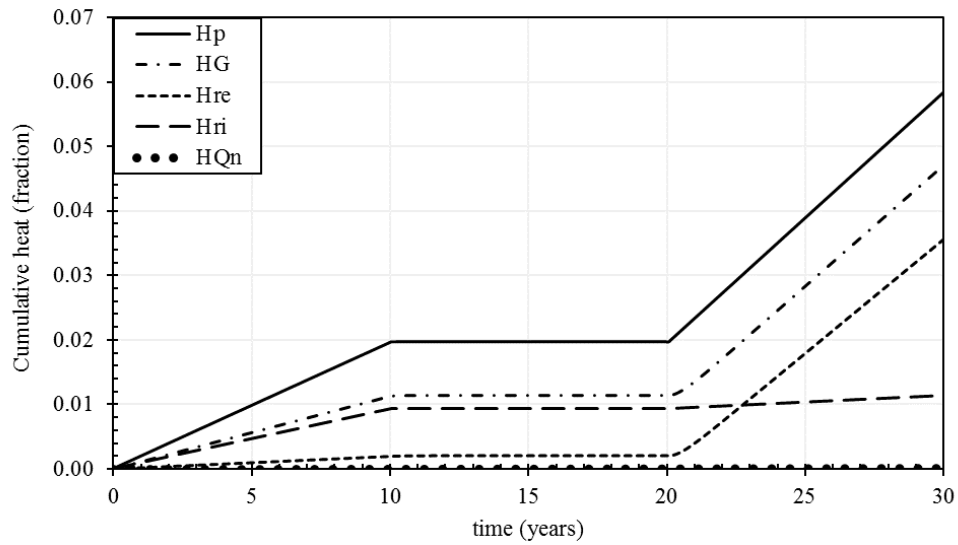


Figure 5.36. Cumulative; produced heat, gained heat, recharged heat, injected heat, and net conductive heat, of Case 2.

One of the advantages of maintaining reservoir pressure can be noted in Figure 5.37, which shows the flash depth and pressure supplied by the downhole pump in the production well. The flash depth in the 1st production period is almost constant and equal to that at the initial reservoir conditions, 400 m. While, in the second production period, the flash depth almost doubled to 720 m due to the high pressure drawdown in this period, given its high net production rate.

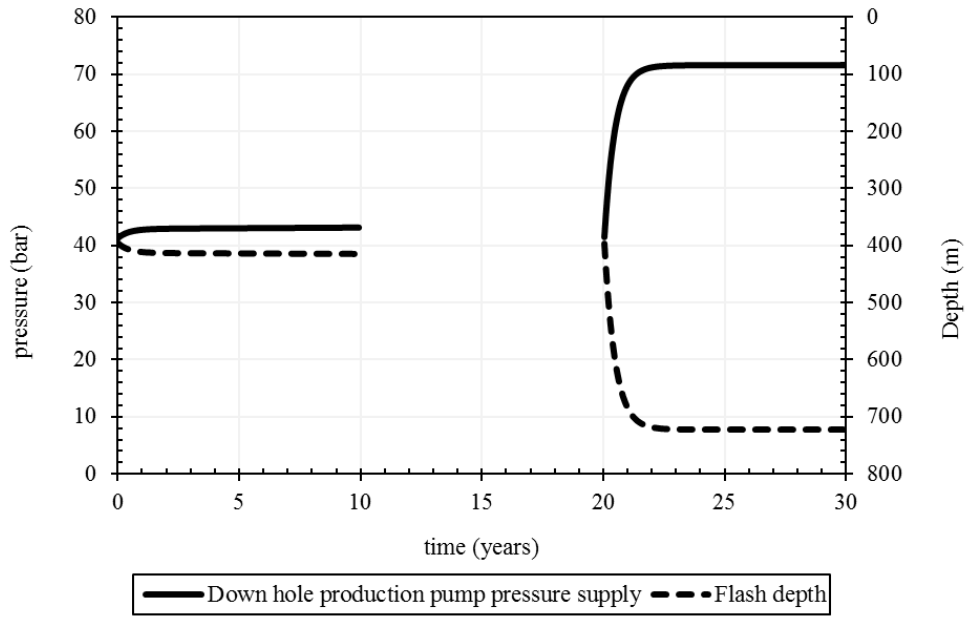


Figure 5.37. Change of flash depth, and pressure supplied by the downhole pump, of Case 2 through time.

On the other side, maintaining reservoir pressure requires higher pressure to be supplied to the geothermal fluid when injecting it back to the reservoir as shown in Figure 5.38. In the 1st production period, the pressure supplied by the injection pump is higher than that at the second production period, where reservoir pressure drawdown is significant. Note the difference between the initial injection pump pressure supply for the 1st production period ($t = 0$) and the 2nd ($t = 20$ years) due to the decrease in injection rate from 450 kg/s in the 1st production period to 100 kg/s in the 2nd production period.

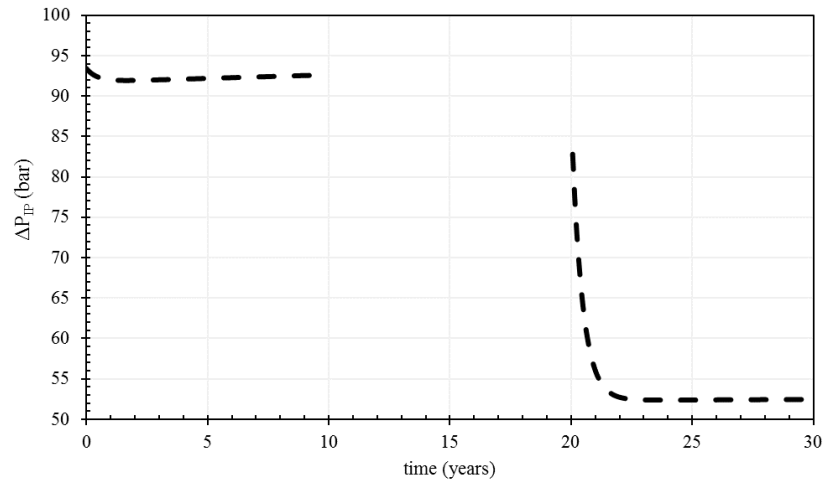


Figure 5.38. Change of pressure supplied by the injection pump through time.

DHP and IP requirements are shown in Figure 5.39. In the first production period, the IP requires more work relative to that of DHP. While, in the second production period, the opposite can be observed. The reason for this has been discussed previously, due to the behavior of reservoir pressure in the 1st and 2nd production periods. Power plant running capacity is almost stable in the 1st and 2nd production periods, and equals to 26 MW and 52 MW approximately, respectively. The pump requirements decrease the power plant capacity to around 20 MW for the 1st production period, and 42 MW approximately for the 2nd production period. Note, the decrease in the net running capacity in the first years of the 2nd production period due to the increase in DHP requirement in this period. Given the 2nd production period higher net running capacity, the growth (slope) of cumulative power generated *Power* in this period is higher than that in the 1st production period. The total power generated from this case is equal to 5.44E+06 MWh, which is equal to the power generated from the first case. 30.7% of the total power generated is generated from the first production period, and the rest is generated from the 2nd production period. Although the reservoir in this case is utilized for 20 years only (10 years shut-in), it generated the same amount of power generated from the 1st case.

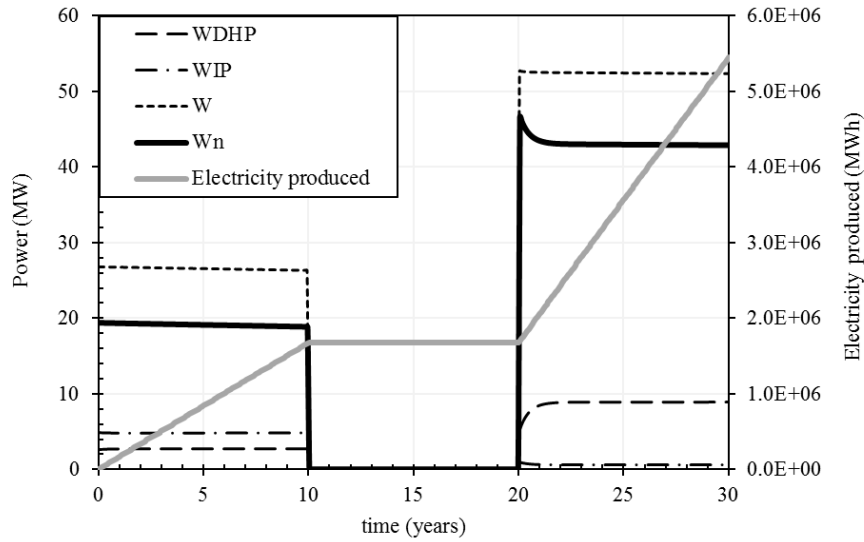


Figure 5.39. Change of; DHP and IP requirements, power, running capacity and its net, in Case 2.

Power plant installed capacity for this case is 28 MW for the first production period, and it's increased to 53 MW for the 2nd production period. The capacity factor is equal to 68% and 81% for the 1st and 2nd production period, respectively. The difference between the capacity factors of the 1st and 2nd production periods is attributed to the decrease in reservoir temperature throughout the 1st and 2nd production period.

5.2.3 Other Cases

The results in terms of cumulative power generated from two production/injection scenarios are shown in this section. In the 3rd case, the production/injection scenario of Case 2 1st production period is utilized for the whole 30 years rather than 10 years only. The production/injection scenario of case 2 2nd production period is utilized for the whole 30 years rather than 10 years only, in the 4th case. In the final case, case 4b, the same production/injection scenario of case 4 is used. However, the recharge temperature T_{re} is decreased from 190 °C to 120 °C.

5.2.3.1 Case 3

Given the 90% injection, reservoir pressure dropped by almost 1.5 bars only after reaching steady state at the 2nd year approximately as shown in Figure 5.40. Reservoir temperature, however, dropped significantly from 190 °C at $t = 0$ to around 186 °C by the end of exploitation as shown in Figure 5.41. This sharp decrease is attributed to the high injection rate, which accompanies low injection temperature relative to initial reservoir temperature. Furthermore, the maintenance of high reservoir pressure in this case limits the amount of recharge that flows into the reservoir.

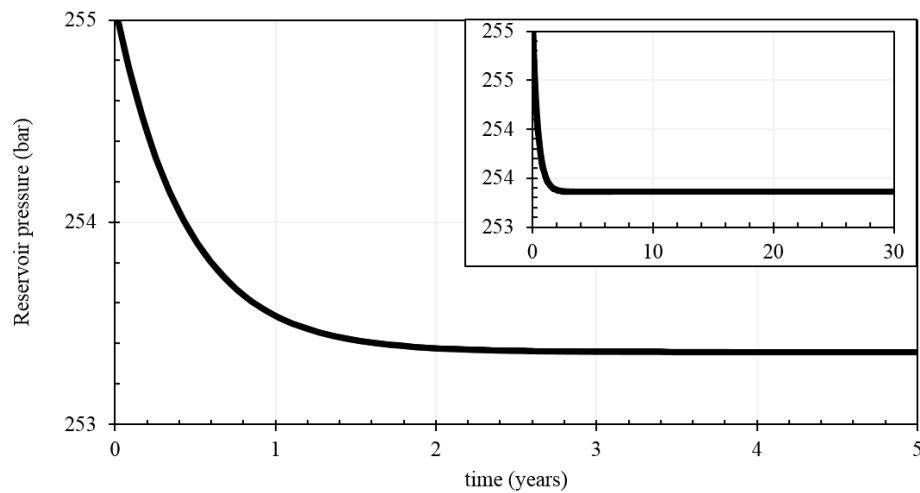


Figure 5.40. Change of reservoir pressure with time, in response to Case 3 production/injection scenario.

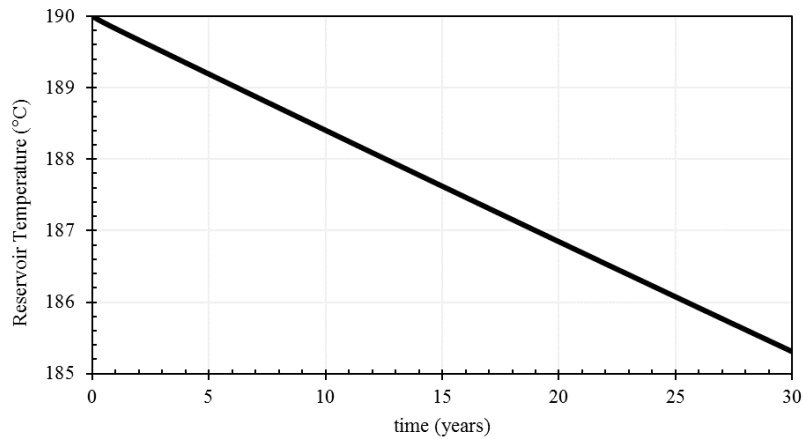


Figure 5.41. Change of reservoir temperature in Case 3, through exploitation.

Due to the small reservoir pressure drawdown in this case, relatively small and stable pump requirements are needed as shown in Figure 5.42. However, the decrease in the running capacity can be noted due to the significant drop in reservoir temperature. The cumulative power generated from this case is equal to $4.88\text{E}+06$ MWh, which is around 10% less than the cumulative power generated in Cases 1 and 2.

The installed capacity of the power plant can be 27 MW, making power plant capacity factor for this case equal to 69%.

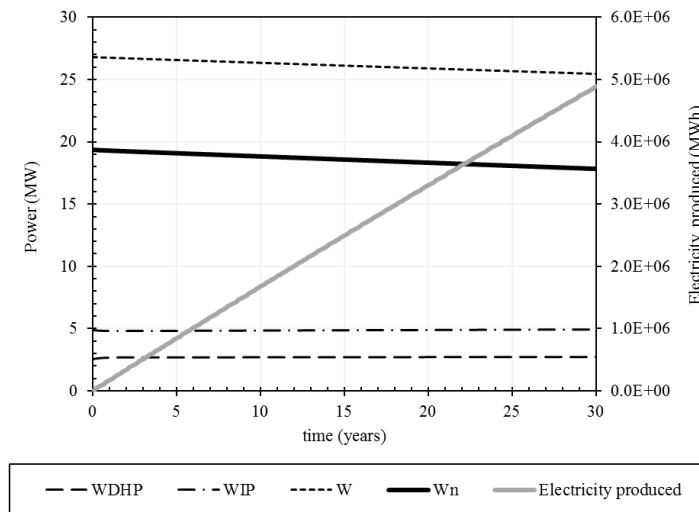


Figure 5.42. Case 3; requirements of DHP and IP, cumulative power generated, running capacity and its net, through time.

5.2.3.2 Case 4

Production/injection scenario, injection temperature, and recharge rate throughout exploitation of this case is shown in Figure 5.43.

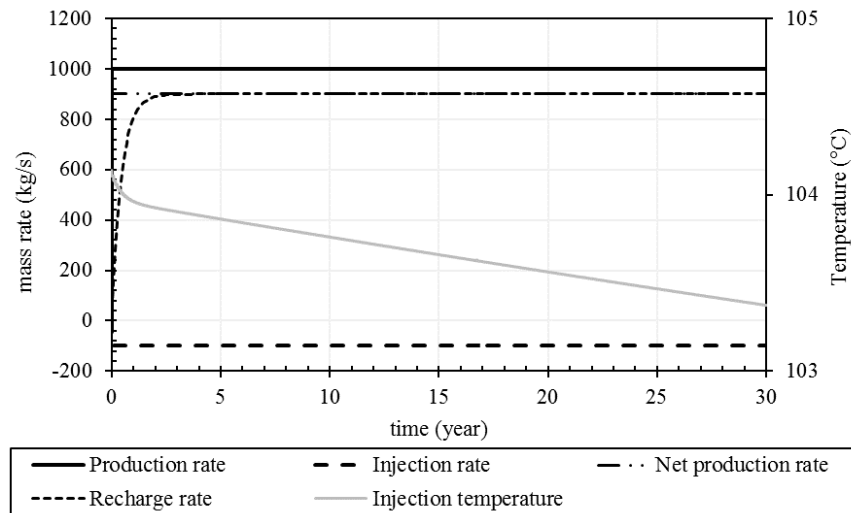


Figure 5.43. Production/injection scenario, injection temperature, and production-induced recharge rate of Case 4.

The responses of reservoir pressure and temperature to Case 4, are shown in Figure 5.44 and Figure 5.45, respectively. Reservoir temperature dropped by 1.4 °C from the beginning to the end of exploitation due to the high reservoir pressure drawdown, which allowed a great amount of recharge (convection) to enter the reservoir as can be noted from the cumulative recharged pore volume in Figure 5.46.

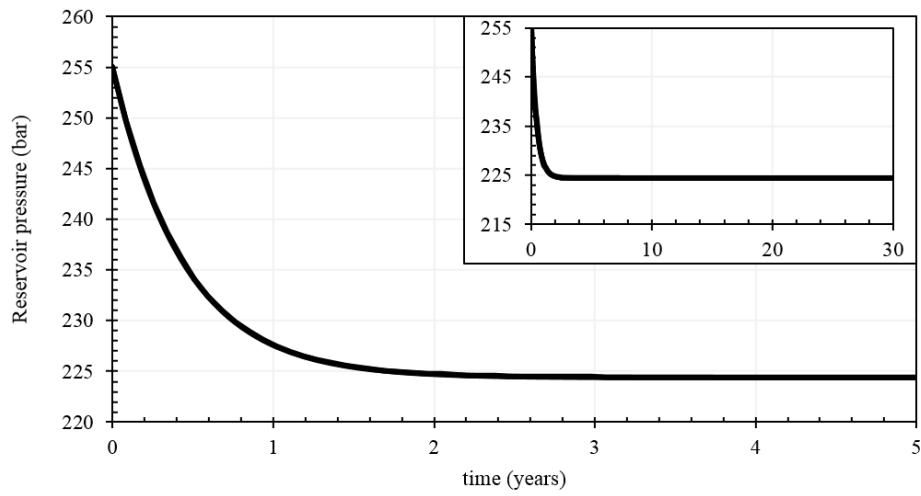


Figure 5.44. Reservoir pressure behavior in response to Case 4 production/injection scenario, through exploitation.

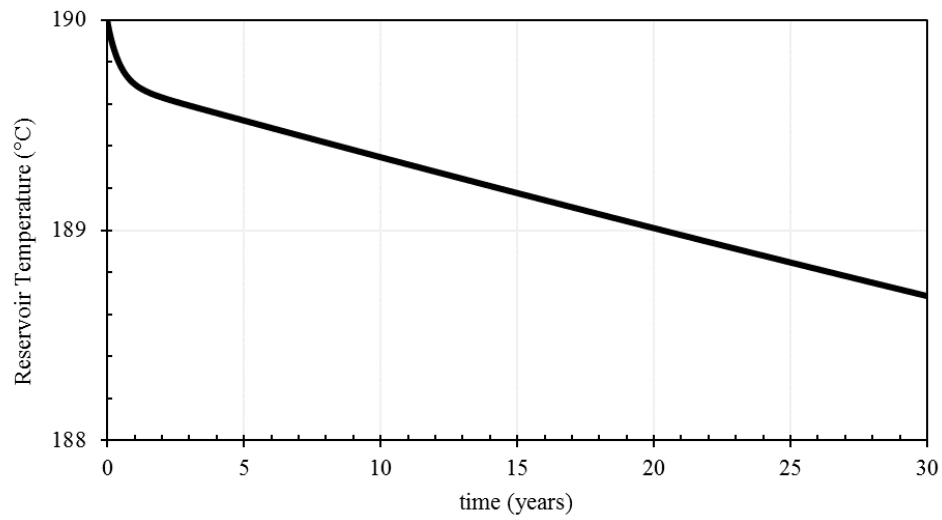


Figure 5.45. Reservoir temperature behavior in response to Case 4 production/injection scenario, through exploitation.

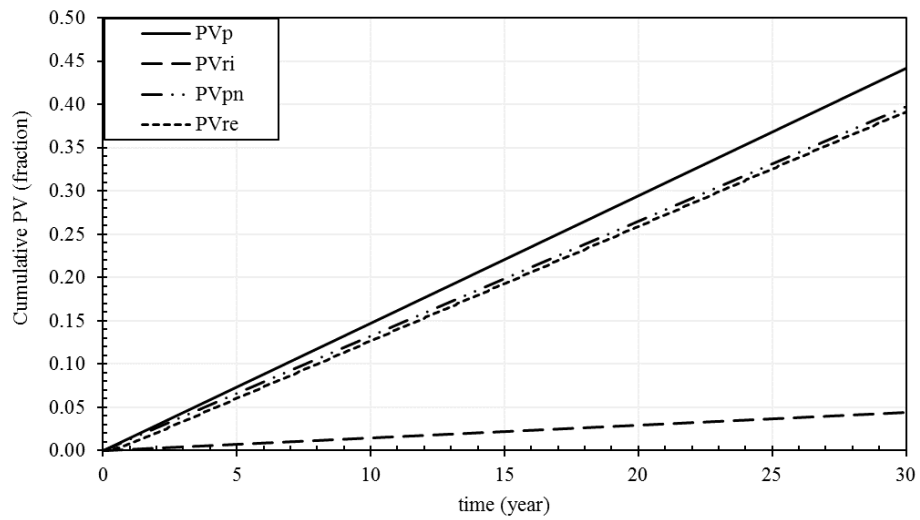


Figure 5.46. Case 4's cumulative, produced PV, injected PV, net produced PV, and recharged PV, through time.

The small reservoir temperature drop from the beginning until the end of exploitation allowed a negligible amount of net conductive heat to enter the reservoir as shown in Figure 5.47.

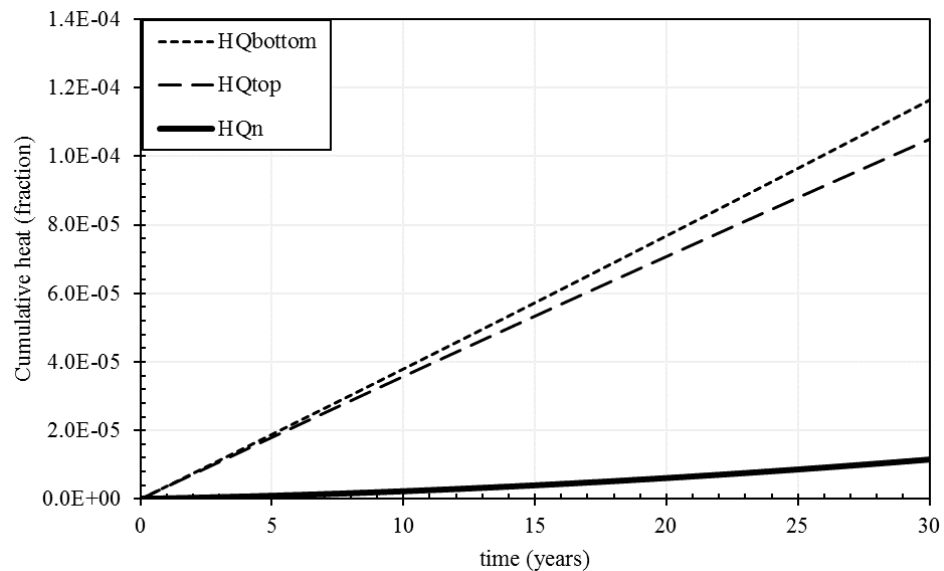


Figure 5.47. Case 4's cumulative conductive heat; gained from the underlying layer, lost to the overlying layer, and net conduction during the 30 years.

The cumulative power generated from this case is equal to $1.15\text{E}+07$ MWh (Figure 5.48), which is around 110% more than the cumulative power generated from case 1 and 2. The down hole pump requirement in this case is relatively high, stable, and equal to 10 MW. However, the injection pump requirement is relatively small and equal to 1 MW, making the total pump requirements equal to 10 MW approximately (the difference between the running capacity and its net).

The power plant installed capacity can be 54 MW, which makes the capacity factor of the binary power plant operated by this case's production/injection scenario to be 81%.

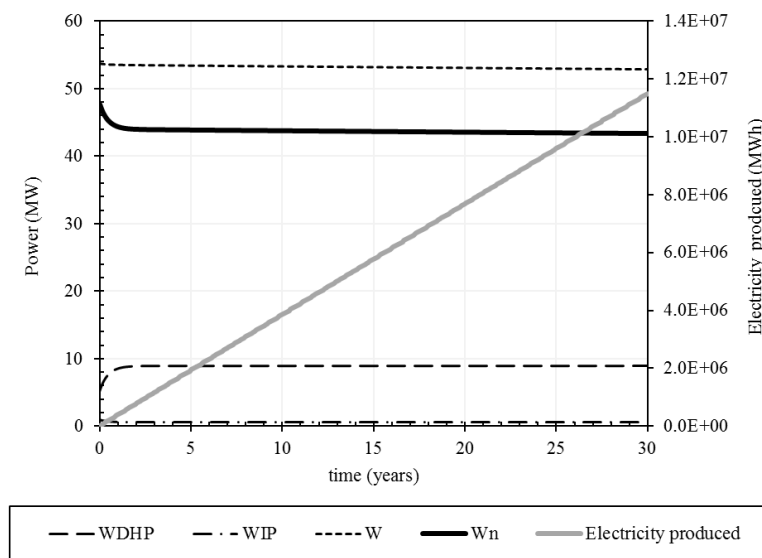


Figure 5.48. Case 4's; requirements of DHP and IP, cumulative power generated, running capacity and its net, through time.

5.2.3.2.1 Case 4b

The response of reservoir temperature behavior to the decrease of recharge temperature by $70\text{ }^{\circ}\text{C}$ is shown in Figure 5.49. Reservoir temperature dropped significantly by around $8\text{ }^{\circ}\text{C}$ from its initial by the end of exploitation relative to the $1\text{ }^{\circ}\text{C}$ approximately decrease of Case 4.

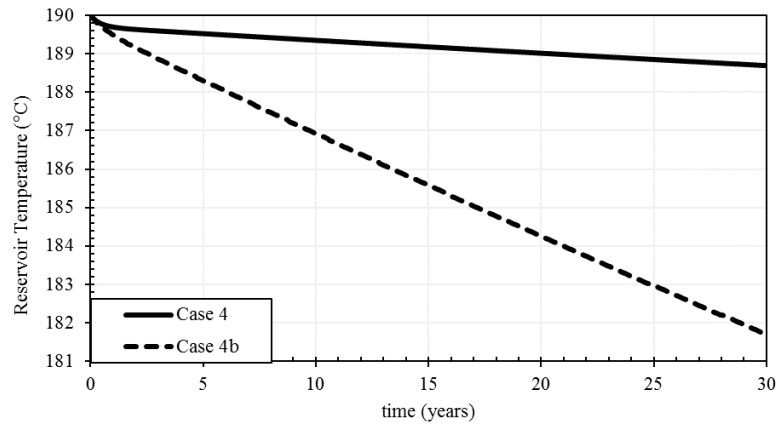


Figure 5.49. Reservoir temperature behavior in response to Case 4 and Case 4b through exploitation.

Although the same mass of case 4 is being produced and injected, reservoir pressure in this case dropped 15 bars more until steady state than that of Case 4 as can be noted from Figure 5.50. This additional 15 bar decrease is attributed to the change in recharge fluid density, which decreased the recharge index α from 29.38 to 19.46 $\frac{kg}{s\ bar}$. Thus, the reservoir received less amount of recharge for every bar decrease from its initial pressure. Note the longer time needed to reach steady state relative to case 4's.

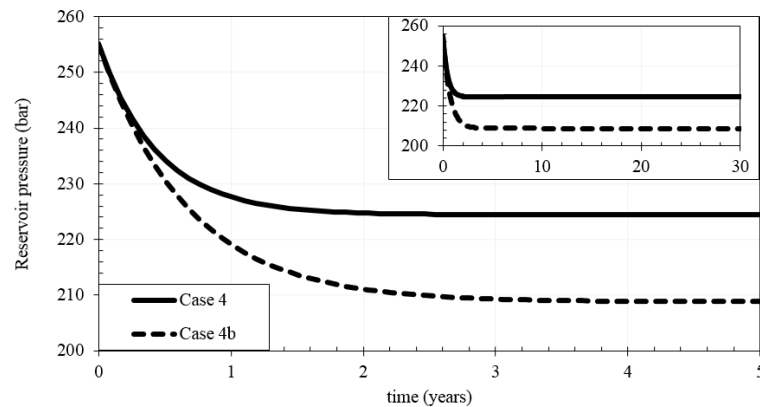


Figure 5.50. Reservoir pressure behavior in response to case 4 and 4b through exploitation.

Figure 5.51 shows the behavior of injection temperature and production-induced recharge rate throughout exploitation for both case 4 and 4b. Injection temperature drop for this case is more significant than that in case 4. Furthermore, case 4's recharge rate reaches to steady state earlier than that in this case. This figure also confirms that the reservoir in case 4b received less amount of recharge compared to that in case 4 (the area under the recharge curve represents the cumulative recharge amount).

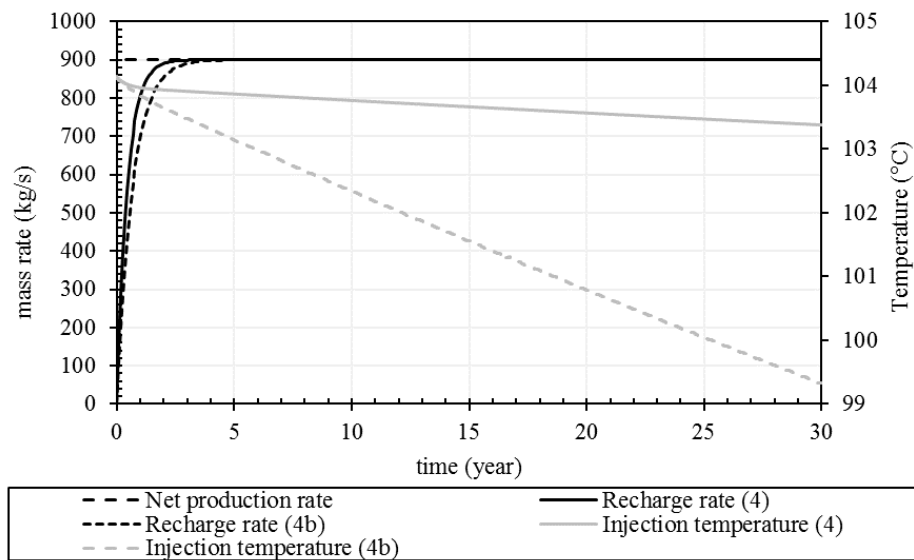


Figure 5.51. production-induced recharge rate and injection temperature of Cases 4 and 4b through time.

Reservoir temperature drop of this case allowed for approximately 250% increase in net conductive heat into the reservoir as shown in Figure 5.52, relative to that of Case 4 at year 30.

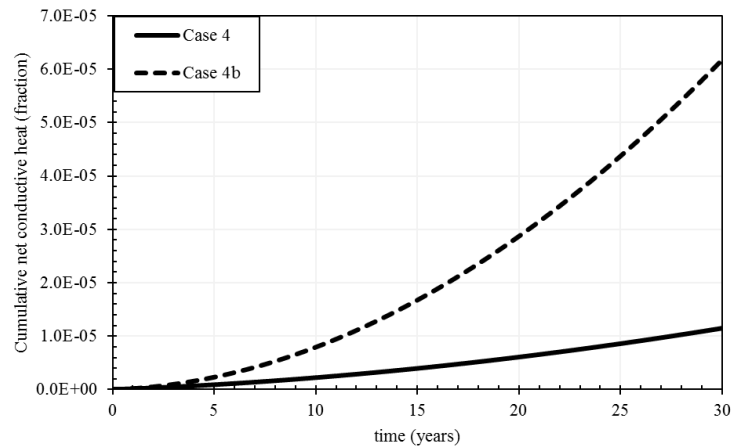


Figure 5.52. Case 4's and 4b's cumulative net conductive heat gained during the 30 years.

The impact of the decrease in reservoir temperature in this case on the running capacity can be noted from Figure 5.53. Injection pump power requirement also increased slightly relative to case 4 (Figure 5.48) due to the increase in injected fluid density. Downhole pump power requirement also increased, but very slightly that it can be negligible. The approximate 36.8% decrease in recharge temperature impacted the power generation by approximately 8.7% less than case 4's.

The installed capacity for this case's power plant is the same as case 4 as the recharge infiltrates the reservoir after exploitation commences (after reservoir pressure decreases). Thus, the capacity factor in this case is around 7% less than the capacity factor of Case 4.

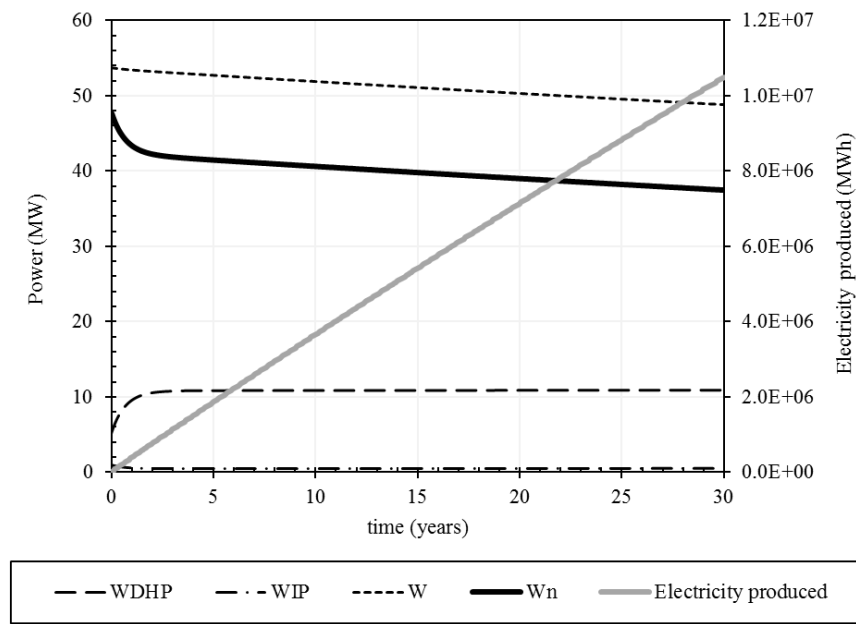


Figure 5.53. Case 4b's; requirements of DHP and IP, cumulative power generated, running capacity and its net, through time.

5.3 Summary

For the considered hypothetical reservoir in this study, Table 5.3 shows the cumulative power generated, and capacity factor of each case. It can be noted that case 4 is the most favorable case in terms of power generation. Moreover, the power plant capacity factor of this case is one of the highest, 81%, which is also equal to that achieved by case 2 second production period.

Table 5.3. Summary of the considered production/injection cases in this study, in terms of electricity produced, installed capacity, and capacity factor.

Case		Electricity produced (MWh)	Installed Capacity (MW)	Capacity factor (%)
1		5.44E+06	27	77
2	1st production period	5.44E+06	28	68
	2nd production period		53	81
3		4.88E+06	27	69
4		11.5E+06	54	81
4b		10.5E+06	54	74

In terms of levelized cost and land use, Table 5.4 shows the results of each case calculated using simple statistics presented earlier in the introduction of this thesis. As a reminder, geothermal occupies a land of 404 m²/GWh for 30 years shown previously in Table 1.1 (Bronicki & Lax, 2004), and the levelized cost of a binary power plant is equal to 6.5 cent/kWh as presented previously in Figure 1.7 (Glassley, 2010). Case 4 has the highest levelized cost and land use. While, Case 3 has the lowest levelized cost and land use.

Table 5.4. Levelized cost and land use of all the four cases.

Case	Levelized cost (\$)	Land use (km ²)
1	354E+06	2.2
2	354E+06	2.2
3	317E+06	2.0
4	748E+06	4.6
4b	683E+06	4.2

CHAPTER 6

CONCLUSION

In this study, a spreadsheet model has been developed for predicting power generation from a binary power plant utilizing low temperature geothermal reservoir. The model takes into consideration the convective and conductive heat transfer mechanisms. Furthermore, it considers the whole journey of the geothermal fluid from the reservoir to the power plant through production wells, and back to the reservoir through injection wells.

The explicit single-tank (control volume) LPM developed in this study has been validated against TOUGH2 code, achieving less than 1% error for a 30 days test period. The model extends Satman (2010) model by adding the following:

- Modeling variable production/injection rates.
- Modeling variable injection temperatures.
- Modeling multiple production/injection periods, and shut-in periods.
- Updating fluid properties according to the change in fluid pressure and temperature, rather than assuming constant values.
- Modeling reservoir conductive heat gain and loss rather than assuming it constant.
- Modeling geothermal fluid flow in porous media at steady state.
- Modeling geothermal fluid conditions (pressure and temperature) through its flow in production and injection wells using simple well model.
- Modeling the running capacity and the power generated from a binary power plant using correlations.

6.1 Results

Five production/injection scenarios (cases) have been investigated for a binary power plant utilizing low temperature geothermal reservoir. Case 4, whose production/injection scenario is of 1000 kg/s constant production rate, 100 kg/s constant injection rate, and geothermal fluid temperature at the outlet of the power plant as the injection temperature, achieved the highest cumulative power generated, 11.5E+06 MWh, relative to other three cases.

If this amount of power is to be generated from coal using Integrated coal Gasification Combined Cycle (IGCC), its capacity factor, life cycle GHG emissions, occupied land, and levelized cost, are shown in Table 6.1 with the results of Case 4. Please note that the coal results shown in the table, are calculated using the simple statistics presented in the introduction of this thesis. As a reminder, coal produces a median of 1000 g CO₂ equivalent per kWh according to the statistics presented in Figure 1.6 by Edenhofer et al. (2011). According to Glassley (2010); the coal – IGCC capacity factor is around 60% (Figure 1.5), and its levelized cost is equal to 8.0 cents/kWh (Figure 1.7). 3642 m²/GWh of land including mining for a 30-year period is occupied by coal-IGCC according to Bronicki & Lax (2004), shown in Table 1.1.

Table 6.1. Capacity factor, lifecycle GHG emissions, land use, and levelized cost of Case 4 (geothermal energy – binary) and Coal (IGCC).

Technology	Capacity factor (%)	Lifecycle GHG Emissions (kg CO ₂ eq.)	Land use (km ²)	Levelized cost (\$)
Geothermal – binary, case 4	81	0	4.6	748E+06
Coal-IGCC	60	1.15E+10	41.9	920E+06

According to Table 6.1, the capacity factor of geothermal (binary) is 21% more than the coal (IGCC). Coal (IGCC), being a conventional energy resource, generates a huge amount of GHGs relative to binary, which is a zero-emission power plant

utilizing a renewable and sustainable energy resource, geothermal. The land Coal (IGCC) occupies is almost 10 times the land area occupied by the binary. Moreover, the levelized cost of coal (IGCC) is around 23% more than the levelized cost of binary power plant.

An average tree absorbs 10 kg of CO₂/year on average during the first 20 years of growth (Bernet, 2021). Assuming this rate holds for 30 years and the coal (IGCC) emissions are CO₂ only, 384E+06 trees would be needed to absorb the emissions of coal (IGCC). Furthermore, the 37 km² land area saved by utilizing binary power plant instead of coal (IGCC), could be used for planting trees or saving the trees already in place occupying this saved area.

6.2 Future Work and Recommendations

During the period of this study, the focus has been the development and validation of the spreadsheet tool. With the tool developed herein, numerous different scenarios can be studied. For example, two interesting cases to be tested are: increase the production to the point where the impact of conduction is clear, and shut in the reservoir once the powerplant efficiency reach a preset value.

In a separate effort, results of Firanda et al. (2021) can be verified, and the impact of non-isothermal wellbore flow can be quantified.

The limitations of the model developed in this study can be eliminated by removing some of the assumptions made in developing the model, and then adding on it. For example:

- The LPM can be extended to several tanks rather than single tank, in which would eliminate the thermodynamic equilibrium and add some spatial discretization.
- The LPM can be extended to two-phase (water and steam) rather than single-phase only.

- Geochemistry can be included by considering the geothermal fluid as brine and CO₂ rather than pure water only.
- Fluid flow type in the porous media could be changed to pseudo-steady state or unsteady state.
- Well model can be improved significantly by; eliminating the constant properties assumption through varying the properties of production and injection wells rather than assuming they all have the same properties, and changing the flow type through the wells from steady state to pseudo-steady state or unsteady state.
- Energy conversion system can be analyzed and calculated analytically rather than using correlations, and pressure losses within the system can be accounted for rather than assuming it negligible.

REFERENCES

- Akhlaghi, Y. G., Kutun, K., Tureyen, O. I., & Satman, A (2015). Effect of Underground Convective Flows on the Performance of Ground Source Heat Exchanger Systems.
- Akın, S., Kok, M. V., & Uraz, I. (2010). Optimization of well placement geothermal reservoirs using artificial intelligence. *Computers & Geosciences*, 36(6), 776-785.
- Alcott, A., Swenson, D., & Hardeman, B. (2012). Conceptual Model Tools in the PetraSim Graphical User Interface for the TOUGH2 Suite of Simulators. TOUGH2 Symposium, Lawrence Berkeley National Laboratory, Berkeley, California.
- Alkan, H., & Satman, A. (1990). A new lumped parameter model for geothermal reservoirs in the presence of carbon dioxide. *Geothermics*, 19(5), 469-479.
- Allegre, C. J., Manhès, G., & Göpel, C. (1995). The age of the Earth. *Geochimica et Cosmochimica Acta*, 59(8), 1445-1456.
- Alp, D. (2021). Numerical Solution of zero-dimensional models of hydrothermal systems [Unpublished work in progress]. Petroleum and Natural Gas Engineering program, Middle East Technical University – Northern Cyprus Campus.
- Antúnez, E., Lippmann, M., & Ali Khan, M. (1995). *Simulation of the Heber geothermal field, a TOUGH2/PC application* (No. LBL-37200; CONF-9503110-). Lawrence Berkeley Lab., CA (United States).
- Axelsson, G. (1989). Simulation of pressure response data from geothermal reservoirs by lumped parameter models. In *Stanford University*.
- Axelsson, G. (2016). Nature and assessment of geothermal resources. *Short Course on Sustainability and Environmental Management of Geothermal Resource Utilization and the Role of Geothermal in Combating Climate Change*, organized by UNU-GTP and LaGeo, Santa Tecla, El Salvador.
- Axelsson, G., & Arason, P. (1992). LUMPFIT, automated simulation of pressure changes in hydrological reservoirs. Version 3.1, user's guide.

- Ay, E. (2005). Comparison of Lumped Parameter and 1D Linear Distributed Models Used in Reservoir Simulation. Lisans bitirme tezi, İTÜ, Petrol ve Doğal Gaz Mühendisliği Bölümü.
- Aydemir, A (2021). Geothermal Energy Technologies, Lecture Notes. Department of Petroleum and Natural Gas Engineering, Middle East Technical University, Northern Cyprus Campus.
- Barbier, E. (1997). Nature and technology of geothermal energy: a review. *Renewable and sustainable energy reviews*, 1(1-2), 1-69.
- Barbier, E. (2002). Geothermal energy technology and current status: an overview. *Renewable and sustainable energy reviews*, 6(1-2), 3-65.
- Benderitter, Y., & Cormy, G. (1990). Possible approach to geothermal research and relative cost estimate. *Small geothermal resources, UNITARRJNDP Centre for Small Energy Resources, Rome, Italy*, 61-71.
- Bernet, R. (2021). *How Much CO2 Does A Tree Absorb? One Tree Planted*. Retrieved July 22, 2022, from <https://onetreepanted.org/blogs/stories/how-much-co2-does-tree-absorb>
- Biagi, J., Agarwal, R., & Zhang, Z. (2015). Simulation and optimization of enhanced geothermal systems using CO2 as a working fluid. *Energy*, 86, 627-637.
- Boardman, T. S., Khan, M. A., & Antunez, E. (1996). *TOUGH2/PC application simulation project for Heber geothermal field, California, a progress report* (No. SGP-TR-151-20). California Department of Conservation, Division of Oil, Gas, & Geothermal Resources, El Centro, CA; California Department of Conservation, Division of Oil, Gas, & Geothermal Resources, Santa Rosa, CA; Lawrence Berkeley National Laboratory, Berkeley, CA.
- Bodvarsson, G., Pruess, K., & Lippmann, M. (1986). Modeling of geothermal systems. *Journal of petroleum technology*, 38(09), 1007-1021.

- Bostanci, Y. (2018). *Estimation of sustainable production limit by using lumped parameter and USGS hydrotherm simulation* (Doctoral dissertation).
- Bradford, N. (n.d.). *Groundwater and the Rising Seas*. NEEF. Retrieved July 3, 2022, from <https://www.neefusa.org/nature/water/groundwater-and-rising-seas>
- Bronicki, L., & Lax, M. (2004). Chapter 12 - Geothermal Energy. In J. Trinnaman & A. Clarke (Eds.), *2004 Survey of Energy Resources (Twentieth Edition)* (pp. 335–362). Elsevier Science. <https://doi.org/https://doi.org/10.1016/B978-008044410-9/50017-6>
- Castanier, L. M., Sanyal, S. K., & Brigham, W. E. (1980). A Practical Analytical Model For Geothermal Reservoirs Simulation. In *SPE California Regional Meeting*. OnePetro.
- Center for Climate and Energy Solutions. (n.d.). *Drought and Climate Change*. C2ES. Retrieved July 3, 2022, from <https://www.c2es.org/content/drought-and-climate-change/>
- Chambers, J. E. (2001). Making more terrestrial planets. *Icarus*, 152(2), 205-224.
- Chong, Q., Wang, J., & Gates, I. D. (2021). Evaluation of energy extraction from a geothermal resource in central Alberta, Canada using different well configurations. *Geothermics*, 96, 102222.
- Chung, M., Vecchi, G., & Sun, J. (2021). *Climate change is probably increasing the intensity of tropical cyclones*. Climate.Gov. Retrieved July 3, 2022, from <https://www.climate.gov/news-features/understanding-climate/climate-change-probably-increasing-intensity-tropical-cyclones>
- Client Earth. (2022). *Fossil fuels and climate change: the facts*. Retrieved July 3, 2022, from <https://www.clientearth.org/latest/latest-updates/stories/fossil-fuels-and-climate-change-the-facts/>
- Dickson, M. H., & Fanelli, M. (2003). *Geothermal energy: utilization and technology*. Routledge.

- Dincer, I., & Ozcan, H. (2018). 1.17 Geothermal Energy. In I. Dincer (Ed.), *Comprehensive Energy Systems* (pp. 702–732). Elsevier.
<https://doi.org/https://doi.org/10.1016/B978-0-12-809597-3.00119-X>
- DiPippo, R. (1998). Geothermal Power Systems. In T.C. Elliott, K. Chen and R.C. Swanekamp (Eds.), Sect. 8.2 in *Standard Handbook of Powerplant Engineering*, 2nd ed., (pp. 8.27–8.60). McGraw-Hill, Inc. New York.
- DiPippo, R. (2008). In *Geothermal power plants: principles, applications, case studies and environmental impact* (2nd ed.). Butterworth-Heinemann.
- Edenhofer, O., Pichs-Madruga, R., Sokona, Y., Seyboth, K., Kadner, S., Zwickel, T., Eickemeier, P., Hansen, G., Schlomer, S., Von-Stechow, C., & Matschoss, P. (Eds.). (2011). *Renewable energy sources and climate change mitigation: Special report of the intergovernmental panel on climate change*. Cambridge University Press.
- Environmental and Energy Study Institute (EESI). (n.d.). *Fossil Fuels*. EESI. Retrieved July 3, 2022, from <https://www.eesi.org/topics/fossil-fuels/description>
- Fajardo, V. R. (2000). Lumped Parameter Model Of The Bacon-Manito Geothermal Production Field Albay, Philipppines”. In *Proceedings*.
- Firanda, E., Pasaribu, F., & Pratama, H. B. (2021). A Modified Non-Isothermal Lumped Parameter Model in Porous Media for Geothermal Reservoirs. In *IOP Conference Series: Earth and Environmental Science* (Vol. 732, No. 1, p. 012019). IOP Publishing.
- Ganguly, S., & Kumar, M. (2012). Geothermal reservoirs—A brief review. *Journal of the Geological Society of India*, 79(6), 589-602.
- Gentry, R. W., & McCray, A. W. (1978). The effect of reservoir and fluid properties on production decline curves. *Journal of Petroleum Technology*, 30(09), 1327-1341.

- Ghosh T.K., Prelas M.A. (2011) Geothermal Energy. In: *Energy Resources and Systems*. Springer, Dordrecht. https://doi.org/10.1007/978-94-007-1402-1_4
- Glassley, W. E. (2010). In *Geothermal energy: renewable energy and the environment*. CRC press.
- Göpel, C., Manhès, G., & Allegre, C. J. (1994). U-Pb systematics of phosphates from equilibrated ordinary chondrites. *Earth and Planetary Science Letters*, 121(1-2), 153-171.
- Grant, M. (2011). In *Geothermal reservoir engineering* (2nd ed.). Elsevier.
- Grant, M. A. (1983). Review no. 1 Geothermal reservoir modeling. *Geothermics*, 12(4), 251-263.
- Gudmundsson, J. S., & Olsen, G. (1987). Water-influx modeling of the Svartsengi geothermal field, Iceland. *SPE Reservoir Engineering*, 2(01), 77-84.
- Guo, B., Song, S., Ghalambor, A., & Lin, T. R. (2013). *Offshore pipelines: design, installation, and maintenance*. Gulf Professional Publishing.
- Gupta, H. K., & Roy, S. (2006). Chapter 4 – Geothermal Systems and Resources. In *Geothermal energy: an alternative resource for the 21st century* (pp. 49 – 59). Elsevier.
- Haklıdır, F. S. T., & Haklıdır, M. (2020). Prediction of reservoir temperatures using hydrogeochemical data, Western Anatolia geothermal systems (Turkey): a machine learning approach. *Natural Resources Research*, 29(4), 2333-2346.
- Hidayat, I. (2016). Decline curve analysis for production forecast and optimization of liquid-dominated geothermal reservoir. In *IOP Conference Series: Earth and Environmental Science* (Vol. 42, No. 1, p. 012024). IOP Publishing.
- Hochstein, M. P. (1988). Assessment and modelling of geothermal reservoirs (small utilization schemes). *Geothermics*, 17(1), 15-49.

- Kaya, E., Zarrouk, S. J., & O'Sullivan, M. J. (2011). Reinjection in geothermal fields: a review of worldwide experience. *Renewable and sustainable energy reviews*, 15(1), 47-68.
- Leaver, J. D. (1986). *Injectivity and Productivity Estimation in Multiple Feed Geothermal Wells* (No. SGP-TR-93-4). Department of Petroleum Engineering, Stanford University; Ministry of Works and Development, New Zealand.
- Lee, K. C. (2001). Classification of geothermal resources by exergy. *Geothermics*, 30(4), 431-442.
- Libretexts. (2020). *1.7: Mechanisms of Heat Transfer*. Physics LibreTexts. Retrieved June 26, 2022, from [https://phys.libretexts.org/Bookshelves/University_Physics/Book%3A_University_Physics_\(OpenStax\)/Book%3A_University_Physics_II_-_Thermodynamics_Electricity_and_Magnetism_\(OpenStax\)/01%3A_Temperature_and_Heat/1.07%3A_Mechanisms_of_Heat_Transfer](https://phys.libretexts.org/Bookshelves/University_Physics/Book%3A_University_Physics_(OpenStax)/Book%3A_University_Physics_II_-_Thermodynamics_Electricity_and_Magnetism_(OpenStax)/01%3A_Temperature_and_Heat/1.07%3A_Mechanisms_of_Heat_Transfer)
- Lindal, B. (1973). Industrial and other applications of geothermal energy. *Geothermal energy*, 135-148.
- Lindsey, R. (2022). *Climate Change: Atmospheric Carbon Dioxide*. Climate.Gov. Retrieved July 3, 2022, from <https://www.climate.gov/news-features/understanding-climate/climate-change-atmospheric-carbon-dioxide#:~:text=Based%20on%20analysis%20from%20NOAA%27s,from%20the%20COVID-19%20pandemic>.
- Lund, J. W., Huttner, G. W., & Toth, A. N. (2022). Characteristics and trends in geothermal development and use, 1995 to 2020. *Geothermics*, 105, 102522.
- Maghiar, T., & Antal, C. (2001). Power generation from low-enthalpy geothermal resources. *Geo-Heat Center Quarterly Bulletin*, 22(2), 35-38.

- Matawal, D. S., & Maton, D. J. (2013). Climate change and global warming: signs, impact and solutions. *International Journal of Environmental Science and Development*, 4(1), 62.
- Math/Science Nucleus. (n.d.). Plate Tectonic. Retrieved January 5, 2022, from https://www.msncucleus.org/membership/html/k-6/pt/plate/1/ptpt1_1a.html
- Moeck, I. S., Beardsmore, G., & Harvey, C. C. (2015). Cataloging worldwide developed geothermal systems by geothermal play type. In *World geothermal congress* (pp. 19-25).
- Muffler, P., & Cataldi, R. (1978). Methods for regional assessment of geothermal resources. *Geothermics*, 7(2-4), 53-89.
- Norton, D. L. (1984). Theory of hydrothermal systems. *Annual Review of Earth and Planetary Sciences*, 12, 155.
- Nunez, C. & National Geographic Staff. (2022). *Sea level rise, explained*. Natinal Geographic. Retrieved July 3, 2022, from <https://www.nationalgeographic.com/environment/article/sea-level-rise-1>
- Nurlaela, F. (2016). Performance Prediction of Two-Phase Geothermal Reservoir using Lumped Parameter Model. In *IOP Conference Series: Earth and Environmental Science* (Vol. 42, No. 1, p. 012030). IOP Publishing.
- Onur, M., Sarak, H., Tureyen, O. I., Cinar, M., & Satman, A. (2008). A new non-isothermal lumped-parameter model for low temperature, liquid dominated geothermal reservoirs and its applications. In *33rd Workshop on Geothermal Reservoir Engineering, Stanford University, USA*.
- Pathak, V., Babadagli, T., Majorowicz, J. A., & Unsworth, M. J. (2014). Evaluation of engineered geothermal systems as a heat source for oil sands production in Northern Alberta. *Natural Resources Research*, 23(2), 247-265.
- Pradhipta, Y. D., Pratama, H. B., & Adiprana, R. (2019). Natural state modeling of Mataloko Geothermal field, Flores Island, East Nusa Tenggara, Indonesia using

TOUGH2 simulator. In *IOP Conference Series: Earth and Environmental Science* (Vol. 254, No. 1, p. 012027). IOP Publishing.

Pruess, K., Oldenburg, C. M., & Moridis, G. J. (1999). *TOUGH2 user's guide version 2* (No. LBNL-43134). Lawrence Berkeley National Lab.(LBNL), Berkeley, CA (United States).

Qin, Z., Valfells, Á., & Guðjónsdóttir, M. S. (2017). The lumped-parameter model on two-phase and superheated geothermal reservoir. *Energy Procedia*, 142, 481-487.

Ripperda, M., & Bodvarsson, G. S. (1987). *Decline curve analysis of production data from The Geysers geothermal field* (No. LBL-22987; CONF-870136-7). Lawrence Berkeley Lab., CA (USA).

Ritchie, H., Roser, M., & Rosado, P. (2020). *Energy*. Our World in Data. Retrieved July 3, 2022, from <https://ourworldindata.org/energy-mix>

Roser, M., Ritchie, H., & Ortiz-Ospina, E. (2013). *World Population Growth*. Our World in Data. Retrieved July 3, 2022, from <https://ourworldindata.org/world-population-growth>

Rybach, L. (1981). Geothermal systems, conductive heat flow, geothermal anomalies. *Geothermal Systems: Principles and case histories*, 3-36.

Rybach, L. (2010). Status and prospects of geothermal energy. In *Proceedings world geothermal congress* (Vol. 5, pp. 1-5).

Sabol, S. (2016). *Case Studies in Mechanical Engineering: Decision Making, Thermodynamics, Fluid Mechanics and Heat Transfer*. John Wiley & Sons.

Sanyal, S. K. (2005). Classification of geothermal systems—a possible scheme. In *Proceedings of the 13th Workshop on Geothermal Reservoir Engineering, Stanford, California* (pp. 85-88).

Sanyal, S. K., & Sarmiento, Z. (2005). Booking geothermal energy reserves. *Geothermal Resources Council Transactions*, 29, 467-474.

- Sanyal, S. K., Morrow, J. W., & Butler, S. J. (2007). Geothermal well productivity: why hotter is not always better. *GRC Transactions*, 31, 573-579.
- Sarak, H., Onur, M., & Satman, A. (2005). Lumped-parameter models for low-temperature geothermal fields and their application. *Geothermics*, 34(6), 728–755. <https://doi.org/https://doi.org/10.1016/j.geothermics.2005.09.001>
- Satman, A. (2010). Sustainability of a geothermal reservoir. In *Proceedings, World Geothermal Congress*.
- Satman, A., Sarak, H., Onur, M., & Korkmaz, E. D. (2005). Modeling of production/reinjection behavior of the Kizildere geothermal field by a two-layer geothermal reservoir Lumped-Parameter Model. In *World Geothermal Congress*.
- Schilthuis, R. J. (1936). Active oil and reservoir energy. *Transactions of the AIME*, 118(01), 33-52.
- Shih, K. G. (1971). Temperature production in the continental crust due to radioactive heat sources. *pure and applied geophysics*, 90(1), 115-125.
- Snyder, D. M., Beckers, K. F., Young, K. R., & Johnston, B. (2017). Analysis of geothermal reservoir and well operational conditions using monthly production reports from Nevada and California. *GRC Trans*, 41, 2844-2856.
- Stein, C. A. (1995). *Heat flow of the Earth. Global earth physics: a handbook of physical constants*, 1, 144-158.
- Swamee, P. K., & Jain, A. K. (1976). Explicit equations for pipe-flow problems. *Journal of the hydraulics division*, 102(5), 657-664.
- Syed, N. I. (2011). Analysis of Well Test Data for The Estimation of Reservoir Parameters and The Prediction of Pressure Response Using Welltester and Lumpfit.
- Taji, O., & Alp, D. (2021). Comparison of Type Well Generation Methods for Unconventional Reservoirs. *SPE Reservoir Evaluation & Engineering*, 1-18.

- Tang, B., Zhu, C., Xu, M., Chen, T., & Hu, S. (2019). Thermal conductivity of sedimentary rocks in the Sichuan basin, Southwest China. *Energy Exploration & Exploitation*, 37(2), 691-720.
- Tester, J.W., Anderson, B., Batchelor, A., Blackwell, D., DiPippo, R., Drake, E., Garnish, J., Livesay, B., Moore, M., Nichols, K., Cambridge, MA, Massachusetts Institute of Technology (2006). The future of geothermal energy: impact of Enhanced Geothermal Systems (EGS) on the United States in the 21st Century. In: Final Report to the US Department of Energy Geothermal Technologies Program
- Thompson, G. R., & Turk, J. (1998). Chapter 2 – Plate Tectonics: A First Look. In *Introduction to physical geology* (pp. 16–35). Brooks/Cole Publishing Company.
- Tureyen, O. I., & Akyapı, E. (2011). A generalized non-isothermal tank model for liquid dominated geothermal reservoirs. *Geothermics*, 40(1), 50-57.
- Tureyen, O. I., Onur, M., & Sarak, H. (2009). A Generalized non-isothermal lumped parameter model for liquid dominated geothermal reservoirs. In *Proc. 34th Workshop on Geothermal Reservoir Engineering Stanford University, Stanford, California*.
- United Nations Development Programme. (2000). *World energy assessment: Energy and the challenge of sustainability*. UNDP.
- United Nations. (n.d.). *The Paris Agreement*. UNFCCC. Retrieved July 3, 2022, from <https://unfccc.int/process-and-meetings/the-paris-agreement/the-paris-agreement>
- Vallejos-Ruiz, O. (2005). Lumped Parameter Model of the Miravalles Geothermal Field, Costa Rica. In *Proc. World geotherm. Congr. Antalya, Turkey*.
- WEC. (2013). *World Energy Resources - Geothermal*. World Energy Council. https://www.worldenergy.org/assets/images/imported/2013/10/WER_2013_9_Geothermal.pdf

- Weixing, H., Lihe, Y., & Xiaoyong, W. (2003). Assessment of geothermal resources for the Qichun geothermal field, Shanxi, China.
- Whiting, R. L., & Ramey, H. J. (1969). Application of material and energy balances to geothermal steam production. *Journal of Petroleum Technology*, 21(07), 893-900.
- Wu, Y., Patel, H., & Salehi, S. (2020). Thermal considerations of cement integrity in geothermal wells. In *The 45th Workshop on Geothermal Reservoir Engineering. Stanford, California, USA*.
- Yeltekin, K., Parlaktuna, M., & Akin, S. (2002). Modeling of Kizildere geothermal reservoir, Turkey. In *Proceedings of the 27th Workshop on Geothermal Reservoir Engineering, Stanford University, Stanford, CA, paper SGP-TR-171 (on CDROM) pp* (pp. 1-8).
- Yin, Q., Jacobsen, S. B., Yamashita, K., Blichert-Toft, J., Télouk, P., & Albarede, F. (2002). A short timescale for terrestrial planet formation from Hf–W chronometry of meteorites. *Nature*, 418(6901), 949-952.
- Yuono, R. T., & Daud, Y. (2020). Reservoir simulation of Ulumbu geothermal field using TOUGH2 and ITOUGH2 simulator. In *IOP Conference Series: Earth and Environmental Science* (Vol. 538, No. 1, p. 012059). IOP Publishing.
- Zarrouk, S. J., & McLean, K. (2019). In S. J. Zarrouk & K. McLean (Eds.), *Geothermal Well Test Analysis*. Academic Press. [https://doi.org/https://doi.org/10.1016/B978-0-12-814946-1.00002-5](https://doi.org/10.1016/B978-0-12-814946-1.00002-5)
- Zarrouk, S. J., & Moon, H. (2014). Efficiency of geothermal power plants: A worldwide review. *Geothermics*, 51, 142-153.
- Zhang, X., Wang, Y., Jiang, Z., Li, J., Zhu, J., Zhao, L., & Jia, Y. (2021). Spatial structure and resource potential of heat storage in Nanmeng geothermal field. In *IOP Conference Series: Earth and Environmental Science* (Vol. 766, No. 1, p. 012042). IOP Publishing.

APPENDICES

A. Derivation of Schilthuis Method, Eq. 4.12

The volumetric flow rate \dot{V}_{re} for a radial reservoir using Darcy's equation is:

$$\dot{V}_{re} = \frac{k_A A}{\mu_w} \frac{dP}{dr} \quad \text{A.1}$$

Cross sectional flow area A , and volumetric flow rate in terms of mass production rate, equal to Eq. A.2 and Eq. A.3:

$$A = 2\pi r L_A \quad \text{A.2}$$

$$\dot{V}_{re} = \frac{\dot{m}_{re}}{\rho_w} \quad \text{A.3}$$

Substituting Eq. A.2, and Eq. A.3 into Eq. A.1 and solving:

$$\begin{aligned} \frac{\dot{m}_{re}}{\rho_w} &= \frac{k_A (2\pi r L_A)}{\mu_w} \frac{dP}{dr} \\ \int_{r_R}^{r_A} \frac{1}{r} dr &= \frac{2\pi k_A L_A \rho_w}{\dot{m}_{re} \mu_w} \int_{P_r}^{P_{re}} dP \\ \ln \left(\frac{r_A}{r_R} \right) &= \frac{2\pi k_A L_A \rho_w}{\dot{m}_{re} \mu_w} (P_{re} - P_{r_j}) \\ \dot{m}_{re} &= \frac{2\pi k_A L_A \rho_w}{\ln \left(\frac{r_A}{r_R} \right) \mu_w} (P_{re} - P_{r_j}) \end{aligned}$$

P_r is the reservoir pressure, and P_{re} is the constant pressure of the recharge source, which equals the reservoir pressure at time equal zero $P_r(t = 0)$ or initial reservoir pressure P_{r_i} ($P_{re} = P_r(t = 0) = P_{r_i}$) due to their equilibrium at time equal zero (Sarak et al., 2005).

$$\dot{m}_{re} = \frac{2\pi k_A L_A}{\ln\left(\frac{r_A}{r_R}\right)} \frac{\rho_w}{\mu_w} (P_{ri} - P_{rj}) = \alpha \Delta P_{rj} \quad \text{A.4}$$

B. Derivation of Reservoir Pressure Behavior, Eq. 4.14.

$$V_R \frac{d(\rho_w \phi_r)}{dt} = \dot{m}_{re} - \dot{m}_{pj} + \dot{m}_{rij} \quad \text{B.1}$$

Production rate w_p and injection rate \dot{m}_{ri} can be defined as the net production rate \dot{m}_{pn} , Eq B.2, acting on Δt . The recharge rate \dot{m}_{re} is modeled using steady state Schilthuis (1936) method, Eq. A.4.

$$\dot{m}_{pnj} = \dot{m}_{pj} - \dot{m}_{irj} \quad \text{B.2}$$

$$\dot{m}_{re} = \alpha (P_{ri} - P_r) \quad \text{A.4}$$

Change of water density ρ_w and rock porosity ϕ_r with time due to their isothermal compressibility, Eq. B.4:

$$\rho_{wj} = \rho_{wj-1} e^{c_f(P_{rj} - P_{rj-1})}$$

$$\phi_{rj} = \phi_{rj-1} e^{c_r(P_{rj} - P_{rj-1})}$$

$$\begin{aligned} \rho_{wj} \phi_{rj} &= \rho_{wj-1} \phi_{rj-1} e^{c_f(P_{rj} - P_{rj-1})} e^{c_r(P_{rj} - P_{rj-1})} = \rho_{wj-1} \phi_{rj-1} e^{(c_f + c_r)(P_{rj} - P_{rj-1})} \\ &= \rho_{wj-1} \phi_{rj-1} e^{c_t(P_{rj} - P_{rj-1})} \approx \rho_{wj-1} \phi_{rj-1} c_t (1 + P_{rj} - P_{rj-1}) \end{aligned}$$

$$\frac{d(\rho_w \phi_r)}{dt} \approx \frac{d}{dt} (\rho_{wj-1} \phi_{rj-1} c_t (1 + P_{rj} - P_{rj-1}))$$

$$\frac{d(\rho_w \phi_r)}{dt} \approx \rho_{wj-1} \phi_{rj-1} c_t \frac{d}{dt} (P_{rj} - P_{rj-1}) \approx \rho_{wj-1} \phi_{rj-1} c_t \frac{dP_r}{dt} \quad \text{B.3}$$

Substituting Eq. B.2, A.4, and B.3 into B.1:

$$V_R \rho_{wj-1} \phi_{rj-1} c_t \frac{dP_r}{dt} = \alpha (P_{ri} - P_r(t)) - \dot{m}_{pnj} \quad \text{B.4}$$

Reservoir storage capacity κ groups the constants of the LHS, Eq. B.5.

$$\kappa_{j-1} \frac{dP_r}{dt} = \alpha \left(P_{r_i} - P_r(t) \right) - \dot{m}_{pn_j} \quad \text{B.5}$$

Rearranging and Defining constant D:

$$\frac{dP_r}{dt} = \frac{\alpha}{\kappa_{j-1}} \left(P_{r_i} - P_r(t) \right) - \frac{\dot{m}_{pn_j}}{\kappa_{j-1}}$$

$$D_{j-1} = \frac{\alpha}{\kappa_{j-1}}$$

$$\frac{dP_r}{dt} = D_{j-1} \left(P_{r_i} - P_r(t) \right) - \frac{\dot{m}_{pn_j}}{\kappa_{j-1}}$$

$$\frac{1}{D_{j-1} \left(P_{r_i} - P_r(t) \right) - \frac{\dot{m}_{pn_j}}{\kappa_{j-1}}} dP_r = dt$$

Using substitution method:

$$u = D_{j-1} \left(P_{r_i} - P_r(t) \right) - \frac{\dot{m}_{pn_j}}{\kappa_{j-1}}$$

$$du = -D_{j-1} dP_r$$

$$\frac{1}{u} \left(-\frac{1}{D_{j-1}} du \right) = dt$$

$$-\frac{1}{D_{j-1}} \int_{u_{j-1}}^{u_j} \frac{1}{u} du = \int_{t_{j-1}}^{t_j} dt$$

$$-\frac{1}{D_{j-1}} \ln \left(\frac{u_j}{u_{j-1}} \right) = (t_j - t_{j-1})$$

$$u_j = u_{j-1} e^{-D_{j-1} \Delta t}$$

$$u_j = -\frac{\dot{m}_{pnj}}{\kappa_{j-1}} + D_{j-1} \left(P_{ri} - P_{rj}(t) \right)$$

$$u_{j-1} = -\frac{\dot{m}_{pnj}}{\kappa_{j-1}} + D_{j-1} \left(P_{ri} - P_{rj-1}(t) \right)$$

$$-\frac{\dot{m}_{pnj}}{\kappa_{j-1}} + D_{j-1} \left(P_{ri} - P_{rj}(t) \right) = \left(-\frac{\dot{m}_{pnj}}{\kappa_{j-1}} + D_{j-1} \left(P_{ri} - P_{rj-1}(t) \right) \right) e^{-D_{j-1}\Delta t}$$

$$P_{rj} = -\frac{\dot{m}_{pnj}}{\alpha} + P_{ri} + \frac{\dot{m}_{pnj}}{\alpha} e^{-D_{j-1}\Delta t} - P_{ri} e^{-D_{j-1}\Delta t} + P_{rj-1} e^{-D_{j-1}\Delta t}$$

Pressure drawdown from the initial reservoir pressure P_{ri} to P_r at time t , is defined as ΔP_r .

$$P_{ri} - P_{rj} = P_{ri} - P_{rj-1} - \left(\Delta P_{rj-1} - \frac{\dot{m}_{pnj}}{\alpha} \right) (1 - e^{-D_{j-1}\Delta t})$$

$$\Delta P_{rj} = \Delta P_{rj-1} - \left(\Delta P_{rj-1} - \frac{\dot{m}_{pnj}}{\alpha} \right) (1 - e^{-D_{j-1}\Delta t}) \quad \text{B.6}$$

If time interval is taken from $t_{j-1} = 0$, where $\Delta P_{rj-1} = 0$, to $t_j = t$, where $\Delta P_{rj} = \Delta P_r$, Sarak et al. (2005) pressure equation is obtained.

$$\Delta P_r = \frac{\dot{m}_{pn}}{\alpha} (1 - e^{-D\Delta t})$$

C. Derivation of Reservoir Temperature Behavior, Eq. 4.17.

$$V_R \rho_{av} C_{av} \frac{dT_r}{dt} = \dot{m}_{re} C_{pwre} T_{re} - \dot{m}_{pj} C_{pw} T_r + \dot{m}_{ri} C_{pwri} T_{W(IW)_j} + Q_n \quad \text{C.1}$$

Recharge rate \dot{m}_{re} is described using Steady state Schilthuis (1936) water influx method (Eq. A.4).

$$\dot{m}_{re} = \alpha (P_{ri} - P_r(t)) = \alpha \Delta P_r \quad \text{A.4}$$

Substituting Eq. B.6 in Eq. A.4 for the reservoir pressure drawdown ΔP_r , yields Eq. C.2.

$$\dot{m}_{re} = \alpha \left(\Delta P_{rj-1} - \left(\Delta P_{rj-1} - \frac{\dot{m}_{pnj}}{\alpha} \right) (1 - e^{-D_{j-1}\Delta t}) \right) \quad \text{C.2}$$

Substituting Eq. C.2 in Eq. C.1, and rearranging yields Eq. C.3

$$\begin{aligned} \frac{dT_r}{dt} + \frac{\dot{m}_{pj}C_{pw}}{V_R\rho_{av}C_{av}}T_r &= \frac{\alpha C_{pwre}T_{re}}{V_R\rho_{av}C_{av}} \left(\Delta P_{rj-1} \right. \\ &\quad \left. - \left(\Delta P_{rj-1} - \frac{\dot{m}_{pnj}}{\alpha} \right) (1 - e^{-D_{j-1}\Delta t}) \right) \\ &\quad + \frac{\dot{m}_{ri}C_{pwri}T_{W(IW)_j}}{V_R\rho_{av}C_{av}} + \frac{Q_n}{V_R\rho_{av}C_{av}} \end{aligned} \quad \text{C.3}$$

For time step $\Delta t = t_j - t_{j-1}$, terms changing with time such as $\rho_{av}C_{av}$, C_{pw} , and Q_n are assumed constant and equal to their values obtained at the previous time index t_{j-1} . \dot{m}_p , \dot{m}_{ri} , and $T_{W(IW)}$, are constants within the time step Δt . C_{pwri} is computed at the bottom hole of the injection well ($P_{W(IW)}$, $T_{W(IW)}$).

$$a_{j-1} = \frac{\dot{m}_{pj}C_{pwj-1}}{V_R(\rho_{av}C_{av})_{j-1}}$$

$$c_{j-1} = \frac{\alpha C_{pwre}T_{re}}{V_R(\rho_{av}C_{av})_{j-1}}$$

$$g_{j-1} = \frac{\dot{m}_{ri}C_{pwri}T_{W(IW)_j}}{V_R(\rho_{av}C_{av})_{j-1}}$$

$$x_{j-1} = \frac{Q_{n_{j-1}}}{V_R(\rho_{av}C_{av})_{j-1}}$$

Thus, this yields Eq. C-4

$$\begin{aligned} \frac{dT_r}{dt} + a_{j-1}T_r = C_{j-1} \left(\Delta P_{r_{j-1}} - \left(\Delta P_{r_{j-1}} - \frac{\dot{m}_{pn_j}}{\alpha} \right) (1 - e^{-D_{j-1}\Delta t}) \right) \\ + g_{j-1} + x_{j-1} \end{aligned} \quad C.4$$

Using integration factor method to solve Eq. C.4.

$$\mu = e^{a_{j-1}t}$$

$$\begin{aligned} \int_{t_{j-1}}^{t_j} \left(\frac{dT_r}{dt} e^{a_{j-1}t} + a_{j-1}T_r e^{a_{j-1}t} \right) dt \\ = \int_{t_{j-1}}^{t_j} \left(C_{j-1} e^{a_{j-1}t} \left(\Delta P_{r_{j-1}} \right. \right. \\ \left. \left. - \left(\Delta P_{r_{j-1}} - \frac{\dot{m}_{pn_{j-1}}}{\alpha} \right) (1 - e^{-D_{j-1}(t-t_{j-1})}) \right) + e^{a_{j-1}t} (g_{j-1} \right. \\ \left. + x_{j-1}) \right) dt \end{aligned}$$

$$\begin{aligned} T_{r_j} e^{a_{j-1}t_j} - T_{r_{j-1}} e^{a_{j-1}t_{j-1}} \\ = \frac{C_{j-1}}{a_{j-1}} \left(\Delta P_{r_{j-1}} (e^{a_{j-1}t_j} - e^{a_{j-1}t_{j-1}}) \right. \\ \left. - \left(\Delta P_{r_{j-1}} - \frac{\dot{m}_{pn_j}}{\alpha} \right) \left((e^{a_{j-1}t_j} - e^{a_{j-1}t_{j-1}}) \right. \right. \\ \left. \left. - \frac{a_{j-1}}{a_{j-1} - D_{j-1}} (e^{(a_{j-1}-D_{j-1})t_j + D_{j-1}t_{j-1}} - e^{(a_{j-1}-D_{j-1})t_{j-1} + D_{j-1}t_{j-1}}) \right) \right. \\ \left. + \left(\frac{g_{j-1}}{a_{j-1}} + \frac{x_{j-1}}{a_{j-1}} \right) (e^{a_{j-1}t_j} - e^{a_{j-1}t_{j-1}}) \right) \end{aligned}$$

$$\begin{aligned}
T_{rj} = & T_{rj-1} e^{-a_{j-1} \Delta t} \\
& + \frac{C_{j-1}}{a_{j-1}} \left(\left(\Delta P_{rj-1} (1 - e^{-a_{j-1} \Delta t}) \right. \right. \\
& - \left(\Delta P_{rj-1} - \frac{\dot{m}_{pnj}}{\alpha} \right) \left((1 - e^{-a_{j-1} \Delta t}) \right. \\
& \left. \left. - \frac{a_{j-1}}{a_{j-1} - D_{j-1}} (e^{-D_{j-1} \Delta t} - e^{-a_{j-1} \Delta t}) \right) \right) \\
& + \left(\frac{g_{j-1}}{a_{j-1}} + \frac{x_{j-1}}{a_{j-1}} \right) (1 - e^{-a_{j-1} \Delta t})
\end{aligned} \tag{C.5}$$

If time interval is taken from $t_{j-1} = 0$, where $\Delta P_{rj-1} = 0$ and $T_{rj-1} = T_{ri}$, to $t_j = t$, where $\Delta P_{rj} = \Delta P_r$ and $T_{rj} = T_r$, Satman (2010) reservoir temperature equation is obtained, Eq. C.6. Note that Satman's model does not contain a well model, thus, parameter $T_{W(IW)}$ is replaced with T_{ri} in the definition of constant g .

$$T_r = T_{ri} e^{-at} + \frac{b'}{a} \left(1 + \frac{D}{a - D} e^{-at} - \frac{a}{a - D} e^{-Dt} \right) + \left(\frac{g}{a} + \frac{x}{a} \right) (1 - e^{-at}) \tag{C.6}$$

where b' is

$$b' = \frac{\dot{m}_{pn} C_{pwre} T_{re}}{V_r \rho_{av} C_{av}}$$

D. Steady State Flow in Radial Reservoir Under Production, Eq. 4.33.

The volumetric flow rate \dot{V}_w for a radial reservoir using Darcy's equation is:

$$\dot{V}_w = \frac{k_R A}{\mu_w} \frac{dP}{dr} \tag{D.1}$$

Cross sectional flow area A, and volumetric flow rate in terms of mass production rate, equal to Eq. D.2 and Eq. D.3:

$$A = 2\pi r h_{comp} \quad D.2$$

$$\dot{V}_w = \frac{\dot{m}_{p(PW)_j}}{\rho_{wj-1}} \quad D.3$$

Substituting Eq. D.2, and Eq. D.3 into Eq. D.1 and solving:

$$\begin{aligned} \frac{\dot{m}_{p(PW)_j}}{\rho_{wj-1}} &= \frac{k(2\pi r h_{comp})}{\mu_{wj-1}} \frac{dP}{dr} \\ \int_{r_W}^{r_R} \frac{1}{r} dr &= \frac{2\pi k_R h_{comp}}{\dot{m}_{p(PW)_j}} \frac{\rho_{wj-1}}{\mu_{wj-1}} \int_{P_{W(PW)}}^{P_r} dP \\ \ln \left(\frac{r_R}{r_W} \right) &= \frac{2\pi k_R h_{comp}}{\dot{m}_{p(PW)_j}} \frac{\rho_{wj-1}}{\mu_{wj-1}} (P_r - P_{W(PW)}) \\ (P_r - P_{W(PW)}) &= \frac{\ln \left(\frac{r_R}{r_W} \right)}{2\pi k_R h_{comp}} \frac{\mu_{wj-1}}{\rho_{wj-1}} \dot{m}_{p(PW)_j} = C_{Dj-1} \dot{m}_{p(PW)} \end{aligned}$$

Drawdown coefficient C_D equals to the inverse of the productivity index J (DiPippo, 2008):

$$\begin{aligned} C_{Dj-1} &= \frac{1}{J_{j-1}} = \frac{\ln \left(\frac{r_R}{r_W} \right)}{2\pi k_R h_{comp}} \frac{\mu_{wj-1}}{\rho_{wj-1}} \\ P_{W(PW)_j} &= P_{rj-1} - \frac{\ln \left(\frac{r_R}{r_W} \right)}{2\pi k_R h_{comp}} \frac{\mu_{wj-1}}{\rho_{wj-1}} \dot{m}_{p(PW)_j} \\ &= P_{rj-1} - C_{Dj-1} \dot{m}_{p(PW)_j} \end{aligned} \quad D.4$$

E. Steady State Flow in Radial Reservoir Under Injection, Eq. 4.61.

The injection case differs from the production case in the sign of Darcy's equation:

$$\dot{V}_w = -\frac{k_R A}{\mu_w} \frac{dP}{dr} \quad \text{E.1}$$

The negative sign in Eq. E.1 is due to the change of pressure with the radius. In the injection case, As the radius increases, the pressure decreases.

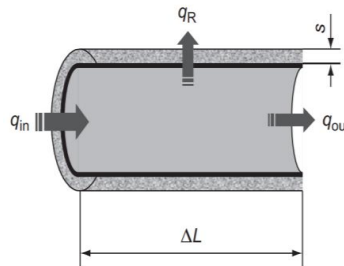
If the same procedure followed in the previous section (Appendix D), reservoir pressure from injection $P_{r(IW)}$ is obtained:

$$\begin{aligned} (P_{W(IW)_j} - P_{r(IW)_j}) &= \frac{\ln\left(\frac{r_R}{r_W}\right)}{2\pi k_R h_{comp}} \frac{\mu_{w,j-1}}{\rho_{w,j-1}} \dot{m}_{ri(IW)_j} = C_{D,j-1} \dot{m}_{ri(IW)_j} \\ P_{r(IW)_j} &= P_{W(IW)_j} - \frac{\ln\left(\frac{r_R}{r_W}\right)}{2\pi k_R h_{comp}} \frac{\mu_{w,j-1}}{\rho_{w,j-1}} \dot{m}_{ri(IW)_j} \\ &= P_{W(IW)_j} - C_{D,j-1} \dot{m}_{ri(IW)_j} \end{aligned} \quad \text{E.2}$$

F. Geothermal Fluid Temperature Behavior in Well.

For a fluid flowing up the production well or down the injection well as shown in Figure below, energy balance is applied to model fluid temperature behavior through the production/injection well. For the pipe element shown of length ΔL , which is surrounded by an insulation layer of thickness s , Eq. F.1 is its energy balance during a time period of Δt (Guo et al., 2013) assuming:

- Isobaric specific heat of water and its density is constant.
- Negligible friction-induced heat.
- The insulation layer controls the heat transfer in the radial direction.



$$q_{in} - q_{out} - q_R = q_{acc} \quad F.1$$

where q_{in} and q_{out} are the energies entering and existing the pipe element by fluid flow, respectively. q_R is the energy transferred from the liquid to the pipe surroundings by conduction, and q_{acc} is the accumulation of energy in the pipe element. These terms are further formulated in Eq. F.2, Eq. F.3, Eq. F.4, and Eq. F.5, respectively.

$$q_{in} = \rho_w C_{pw} v_{PW} A_f T_{f,L} \Delta t_f \quad F.2$$

$$q_{out} = \rho_w C_{pw} v_{PW} A_f T_{f,L+\Delta L} \Delta t_f \quad F.3$$

$$q_R = 2\pi r_n \lambda_n \Delta L \frac{\partial T_f}{\partial r} \Delta t_f \quad F.4$$

$$q_{acc} = \rho_w C_{pw} A_f \Delta L \Delta \bar{T}_f \quad F.5$$

Where $T_{f,L}$ is flowing-in fluid temperature, $T_{f,L+\Delta L}$ is flowing-out fluid temperature, Δt_f is flow time, $\frac{\partial T_f}{\partial r}$ is radial temperature gradient in the insulation layer, and $\Delta \bar{T}_f$ is the average temperature increase of fluid in the pipe segment.

Substituting Eq. F.2, Eq. F.3, Eq. F.4, and Eq. F.5 into Eq. F.1, and dividing by $\Delta L \Delta t_f$:

$$\rho_w C_{pw} v_{PW} A_f \frac{(T_{f,L} - T_{f,L+\Delta L})}{\Delta L} - 2\pi r_n \lambda_n \frac{\partial T_f}{\partial r} = \rho_w C_{pw} A_f \frac{\Delta \bar{T}_f}{\Delta t_f} \quad F.6$$

Radial temperature gradient in the insulation layer is formulated in Eq. F.7

$$\frac{\partial T_f}{\partial r} = \frac{T_f - (T_{f,0} - G \cos(\theta) L)}{s} \quad F.7$$

Rearranging, substituting Eq. F.7 into Eq. F.6, and taking the infinitesimal of ΔL and Δt_f

$$-\rho_w C_{pw} v_{PW} A_f \frac{(T_{f,L+\Delta L} - T_{f,L})}{\Delta L} - \rho_w C_{pw} A_f \frac{\Delta \bar{T}_f}{\Delta t_f} = 2\pi r_n \lambda_n \frac{\partial T_f}{\partial r}$$

$$v_{PW} \frac{(T_{f,L+\Delta L} - T_{f,L})}{\Delta L} + \frac{\Delta \bar{T}_f}{\Delta t_f} = -\frac{2\pi r_n \lambda_n}{\rho_w C_{pw} A_f} \frac{\partial T_f}{\partial r}$$

$$v_{PW} \frac{\partial T_f}{\partial L} + \frac{\partial T_f}{\partial t_f} = -\frac{2\pi r_n \lambda_n}{\rho_w C_{pw} A_f} \left(\frac{T_f - (T_{f,0} - G \cos(\theta) L)}{s} \right)$$

For steady flow conditions, fluid temperature at any point is independent of time.

Thus, the second term of the LHS is zero.

$$\begin{aligned} \frac{\partial T_f}{\partial L} = & -\frac{2\pi r_n \lambda_n}{\rho_w C_{pw} A_f v_{PW} S} T_f + \frac{2\pi r_n \lambda_n}{\rho_w C_{pw} A_f v_{PW} S} T_{f,0} \\ & - \frac{2\pi r_n \lambda_n}{\rho_w C_{pw} A_f v_{PW} S} G \cos(\theta) L \end{aligned} \quad \text{F.8}$$

Identifying the following constants, substituting them (Eq. F.9, Eq. F.10, and Eq. F.11) into Eq. F.8, and rearranging yields Eq. F.12

$$\alpha_c = \frac{2\pi r_n \lambda_n}{\rho_w C_{pw} S A_f v_{PW}} \quad \text{F.9}$$

$$\beta_c = \frac{2\pi r_n \lambda_n G \cos(\theta)}{\rho_w C_{pw} S A_f v_{PW}} = \alpha_c G \cos(\theta) \quad \text{F.10}$$

$$\gamma_c = -\frac{2\pi r_n \lambda_n T_{f,0}}{\rho_w C_{pw} S A_f v_{PW}} = -\alpha_c T_{f,0} \quad \text{F.11}$$

$$\frac{\partial T_f}{\partial L} + \alpha_c T_f + \beta_c L + \gamma_c = 0 \quad \text{F.12}$$

Let

$$u = \alpha_c T_f + \beta_c L + \gamma_c \quad \text{F.13}$$

Thus

$$T_f = \frac{u - \beta_c L - \gamma_c}{\alpha_c} \quad \text{F.14}$$

$$\frac{dT_f}{dL} = \frac{1}{\alpha_c} \frac{du}{dL} - \frac{1}{\alpha_c} \beta_c \quad \text{F.15}$$

Substituting Eq. F.14 and Eq. F.15 into Eq. F.12

$$\frac{1}{\alpha_c} \frac{du}{dL} - \frac{1}{\alpha_c} \beta_c + u = 0$$

Using separation of variables method

$$\frac{1}{\beta_c - u\alpha_c} du = dL \quad \text{F.16}$$

Let,

$$m = \beta_c - u\alpha_c \quad \text{F.17}$$

Thus,

$$du = -\frac{1}{\alpha_c} dm \quad \text{F.18}$$

Substituting Eq. F.17 and Eq. F.18 into Eq. F.16

$$\begin{aligned} \frac{1}{m} \left(-\frac{1}{\alpha_c} dm \right) &= dL \\ -\frac{1}{\alpha_c} \int \frac{1}{m} dm &= \int dL \\ -\frac{1}{\alpha_c} \ln(m) &= L + C \end{aligned} \quad \text{F.19}$$

Substituting the definition of m (Eq. F.17) and definition of u (Eq. F.13) into Eq. F.19

$$-\frac{1}{\alpha_c} \ln(\beta_c - \alpha_c^2 T_f - \alpha_c \beta_c L - \alpha_c \gamma_c) = L + C$$

Rearranging and solving for T_f

$$T_f = \frac{1}{\alpha_c^2} (\beta_c - \alpha_c \beta_c L - \alpha_c \gamma_c - e^{-\alpha_c(L+C)})$$

Integration constant C is determined using the initial conditions, which differ for the production case and the injection case. In case of production, the initial condition of the geothermal fluid at the bottom hole of the production well is

$$T_f = T_r \quad \text{at} \quad L = 0$$

$$C_{prod} = -\frac{1}{\alpha_c} \ln(\beta_c - \alpha_c^2 T_r - \alpha_c \gamma_c)$$

In case of Injection, the initial condition of the geothermal fluid at the wellhead of the injection well is

$$T_f = T_{ri} \quad \text{at} \quad L = L_W$$

$$C_{inj} = -L_W - \frac{1}{\alpha_c} \ln(\beta_c - \alpha_c^2 T_{ri} - \alpha_c \beta_c L_W - \alpha_c \gamma_c)$$

Note that v_{PW} in constants α_c (Eq. F.9), β_c (Eq. F.10), and γ_c (Eq. F.11), is replaced by v_{IW} in the injection case.

G. Liquid Flow in Wells.

$$-dP - \frac{dF}{A_f} - \rho_w g dz = \rho_w v dv \quad \text{G.1}$$

$$dF = \frac{1}{2} \rho_w v^2 f C dz \quad \text{G.2}$$

$$C = 2\pi r_W = \pi D_W \quad \text{G.3}$$

$$A_f = \frac{1}{4} \pi D_W^2 \quad \text{G.4}$$

Substituting Eq. G.2, Eq. G.3, and Eq. G.4 into Eq. G.1

$$-dP - \frac{\frac{1}{2} \rho_w v^2 f_F \pi D_W dz}{\frac{1}{4} \pi D_W^2} - \rho_w g dz = \rho_w v dv$$

$$-dP = \rho_w v dv + \frac{2}{D} \rho_w v^2 f dz + \rho_w g dz$$

$$-\int_{P_W}^{P_h} dP = \int_{v_1}^{v_2} \rho_w v dv + \frac{2}{D} \int_{z_1}^{z_2} \rho_w v^2 f_F dz + g \int_{z_1}^{z_2} \rho_w dz$$

$$P_W - P_h = \int_{v_1}^{v_2} \rho_w v dv + \frac{2}{D} \int_{Z_1}^{Z_2} \rho_w v^2 f_F dz + g \int_{Z_1}^{Z_2} \rho_w dz \quad \text{G.5}$$

As only liquid flow is considered in this model; water density is assumed constant through the production well, velocity is assumed constant as the flow area A_f is constant. Thus, Eq. G.5 reduces to Eq. G.6.

$$P_{W(PW)} - P_{Wh(PW)} = \frac{2}{D_W} \rho_w v^2 f_F \int_{Z_1}^{Z_2} dz + \rho_w g \int_{Z_1}^{Z_2} dz \quad \text{G.6}$$

$$P_{W(PW)} - P_{Wh(PW)} = \frac{2}{D_W} \rho_w v^2 f_F (Z_2 - Z_1) + \rho_w g (Z_2 - Z_1) \quad \text{G.7}$$

$$\text{Where } (Z_2 - Z_1) = L_W \quad \text{G.8}$$

$$v = \frac{\dot{m}_{p(PW)}}{\rho_w A_f} = \frac{\dot{m}_{p(PW)}}{\rho_w \left(\frac{1}{4} \pi D_W^2 \right)} \quad (\text{Continuity equation}) \quad \text{G.9}$$

$$\text{and } f_D = 4f_f \quad \text{G.10}$$

Substituting Eq. G.8, Eq. G.9, and Eq. G.10 into Eq. G.7

$$P_{W(PW)} - P_{Wh(PW)} = \frac{8f_D}{\pi^2 \rho_w D_W^5} L_W \dot{m}_{p(PW)}^2 + \rho_w g L_W$$

$$\text{Let } C_2 = \frac{8f_D}{\pi^2 \rho_w D_W^5}$$

Thus,

$$P_{W(PW)} - P_{Wh(PW)} = (C_2 \dot{m}_{p(PW)}^2 + \rho_w g) L_W$$

$$P_{Wh(PW)} = P_{W(PW)} - (C_2 \dot{m}_{p(PW)}^2 + \rho_w g) L_W$$

The same applies for the injection well, however, the movement direction of the geothermal fluid is in the opposite direction and injection rate is used rather than production rate. Thus, for the injection case, the signs of the first and third terms in the LHS of Eq. G.1, are opposite to that in the production case, Eq. G.11.

$$dP - \frac{dF}{A_f} + \rho_w g dz = \rho_w v dv \quad \text{G.11}$$

The same solution procedure followed in the production case, is followed for the injection case, obtaining:

$$P_{Wh(IW)} - P_{W(IW)} = (C_2 \dot{m}_{ri(IW)}^2 - \rho_w g) L_W$$

$$P_{W(IW)} = P_{Wh(IW)} - (C_2 \dot{m}_{ri(IW)}^2 - \rho_w g) L_W$$

H. Derivation of Cumulative Recharge

The cumulative recharge within a time step M_{re} :

$$\begin{aligned} M_{re_j} &= \int_{t_{j-1}}^{t_j} \dot{m}_{re_j} dt = \int_{t_{j-1}}^{t_j} \alpha \Delta P_{r_j} dt \\ M_{re_j} &= \alpha \int_{t_{j-1}}^{t_j} \Delta P_{r_j} dt = \alpha \int_{t_{j-1}}^{t_j} \left(\Delta P_{r_{j-1}} - \left(\Delta P_{r_{j-1}} - \frac{\dot{m}_{pn}}{\alpha} \right) (1 - e^{-D\Delta t}) \right) dt \\ M_{re_j} &= \alpha \left(\int_{t_{j-1}}^{t_j} \Delta P_{r_{j-1}} dt - \int_{t_{j-1}}^{t_j} \left(\left(\Delta P_{r_{j-1}} - \frac{\dot{m}_{pn}}{\alpha} \right) (1 - e^{-D\Delta t}) \right) dt \right) \\ M_{re_j} &= \alpha \left(\Delta P_{r_{j-1}} \Delta t - \left(\Delta P_{r_{j-1}} - \frac{\dot{m}_{pn}}{\alpha} \right) \int_{t_{j-1}}^{t_j} (1 - e^{-D\Delta t}) dt \right) \\ M_{re_j} &= \alpha \left(\Delta P_{r_{j-1}} \Delta t - \left(\Delta P_{r_{j-1}} - \frac{\dot{m}_{pn}}{\alpha} \right) \left(\Delta t + \frac{1}{D} (e^{-D\Delta t} - e^{-D(t_{j-1}-t_{j-1})}) \right) \right) \\ M_{re_j} &= \alpha \left(\Delta P_{r_{j-1}} \Delta t - \left(\Delta P_{r_{j-1}} - \frac{\dot{m}_{pn}}{\alpha} \right) \left(\Delta t - \frac{1}{D} (1 - e^{-D\Delta t}) \right) \right) \end{aligned}$$

If time interval is taken from $t_{j-1} = 0$, where $\Delta P_{r_{j-1}} = 0$, to $t_j = t$, where $\Delta P_{r_j} = \Delta P_r$, Satman (2010) cumulative recharge equation is obtained.

$$M_{re} = \dot{m}_{pn} \left(t - \frac{1}{D} (1 - e^{-Dt}) \right)$$

TEZ İZİN FORMU / THESIS PERMISSION FORM

PROGRAM / PROGRAM

Sürdürülebilir Çevre ve Enerji Sistemleri / Sustainable Environment and Energy Systems

☒

Siyaset Bilimi ve Uluslararası İlişkiler / Political Science and International Relations

☐

İngilizce Öğretmenliği / English Language Teaching

☐

Elektrik Elektronik Mühendisliği / Electrical and Electronics Engineering

☐

Bilgisayar Mühendisliği / Computer Engineering

☐

Makina Mühendisliği / Mechanical Engineering

☐

YAZARIN / AUTHOR

Soyadı / Surname : Taji

Adı / Name : Oubaida

Programı / Program : Sustainable Environment and Energy Systems

TEZİN ADI / TITLE OF THE THESIS (İngilizce / English) : Power Generation from Low Temperature Liquid Dominated Geothermal Systems Utilizing a Binary Power Plant

TEZİN TÜRÜ / DEGREE:

Yüksek Lisans / Master

☒

Doktora / PhD

☐

1. Tezin tamamı dünya çapında erişime açılacaktır. / Release the entire work immediately for access worldwide. ☐

2. Tez iki yıl süreyle erişime kapalı olacaktır. / Secure the entire work for patent and/or proprietary purposes for a period of two years. * ☐

3. Tez altı ay süreyle erişime kapalı olacaktır. / Secure the entire work for period of six months. * ☒

Yazarın imzası / Author Signature Tarih / Date

Tez Danışmanı / Thesis Advisor Full Name: Asst. Prof. Dr. Doruk Alp

Tez Danışmanı İmzası / Thesis Advisor Signature:

Eş Danışmanı / Co-Advisor Full Name: Prof. Dr. Mahmut Parlaktuna

Eş Danışmanı İmzası / Co-Advisor Signature:

Program Koordinatörü / Program Coordinator Full Name:

Program Koordinatörü İmzası / Program Coordinator Signature: